Magnetic field mapper based on rotating coils

Candidate:

Eng. Ernesto De Matteis

CERN Supervisor:

Prof. Stephan Russenschuck

University Supervisor:

Prof. Pasquale Arpaia

Department of Engineering,
University of Sannio, Benevento

©Ernesto De Matteis

CERN-THESIS-2016-147
15/01/2016

List of publications

List of the publications of the candidate

Book:

[1] Arpaia P., E. De Matteis and V. Inglese, "Flexible Test Automation - A Software Framework for Easily Developing Measurement Automation", *Momentum Press*, New York, USA, 31 Dec 2014.

Research Book Chapter:

[2] P. Arpaia, E. De Matteis et al., "Integrated Telemedicine Systems: Patient Monitoring, In-time Prognostics, and Diagnostics at Domicile", The design and manufacture of medical devices, *Woodhead Pub Limited*, October 2012.

Journal Papers:

[3] P. Arpaia, E. De Matteis and R. Schiano Lo Moriello, "Unscented Transform-based Uncertainty Analysis of Rotating Coil Transducers for Field Mapping", *AIP Review of Scientific Instruments*, (accepted for publication, November 2015);

[4] P. Arpaia, M. Buzio, E. De Matteis and S. Russenschuck, "A Rotating Coil Transducer for Magnetic Field Mapping", *IOP Journal of Instrumentation*, Vol. 10, 2015;

[5] P. Arpaia, E. De Matteis and V. Inglese, "Software for measurement automation: a review of the state of the art", *Elsevier Measurement*, Vol. 66, pp. 10-25, April 2015;

[6] P. Arpaia, P. Cimmino, E. De Matteis, and G. D'Addio, "A Low-Cost Force Sensor-based Posturographic Plate for Home Care Telerehabilitation Exergaming", *Elsevier Measurement*, Volume 51, May 2014, Pages 400-410;

Conference Papers:

[7] P. Arpaia, M. Buzio, E. De Matteis, O. Dunkel, and S. Russenschuck, "Magnetic field mapper based on rotating coil", *I2MTC 2016*, Taipei, Taiwan, May 23-26, 2016;

[8] P. Arpaia, E. De Matteis and V. Inglese, "Perspectives of Software for Measurement Automation", *XXI IMEKO World Congress*, August 30 - September 4, 2015, Prague, Czech Republic;

[9] P. Arpaia, M. Buzio, E. De Matteis, O. Dunkel and S. Russenschuck, "Experimental characterization of a rotating coil transducer for local multipole scanning", *20th IMEKO TC4*, Benevento, Italy, Sept 15-17, 2014;

[10] P. Arpaia, E. De Matteis, D. De Paola and M. Sosin, "Comparative assessment of signal cable impact in differential capacitive position measurements", *20th IMEKO TC4*, Benevento, Italy, Sept 15-17, 2014;

[11] G. D'Addio, P. Cimmino, E. De Matteis and P. Arpaia, "Home Care and Domotic Zigbee Network for Telemedicine Applications", *24th MIE2012* - in Pisa, August 26th -29th, 2012;

[12] P. Arpaia, P. Cimmino, E. De Matteis and G. D'Addio, "A Balance Board Device for Home Care Telerehabilitation Exergaming", *XX IMEKO World Congress* September 9-14, 2012, Busan, Republic of Korea;

[13] P. Arpaia, E. De Matteis, G. Montenero, C. Manna, "Evolutionary Design of Lifting Scheme Wavelet-Packet Adaptive Filters for Elevator Fault Detection", *Proc. of. I2MTC 2010*, Austin, USA;

[14] P. Arpaia, E. De Matteis, C. Manna, "An Evolutionary Lifting Scheme Wavelet Packet Decomposition method for Mechanical Fault Detection in Elevator Systems", *17th Symposium IMEKO TC 4*, Sept. 8-10, 2010, Kosice, Slovakia.

Acknowledgments

The work presented in this dissertation was carried out at CERN, in collaboration with the Engineering Department of the University of Sannio (Benevento, Italy) and the Magnetic Measurements section of CERN, Technology Department (TE) and Magnets Superconductor and Cryogenics (MSC) group. The Thesis represents, personally, the end of a "long walk" that started five years ago, when I got the PhD position at university. These years, not always easy, have grown and improved both professionally and temperamentally, and then I must thank all the people with whom I worked and shared this experience started in 2010.

First of all, I would like to give my big thanks to my university supervisor Professor Pasquale Arpaia. He was my guidance and reference in the last seven years, teaching me the love for research and giving me support in difficult times. All my research and professional experience was possible thanks to him.

I want to thank my CERN supervisor (Section's boss), Stephan Russenschuck, for his professional and technical guidance. His passion for the research, and his determination for reaching the objective, improved my technical and human skills.

I'd like to thank the group leader Luca Bottura, and the Prof. Luigi Glielmo, university coordinator. I gratefully acknowledge to the entire TE-MSC-MM section at CERN for their support and for their kind availability to help me in my technical problem (Olaf, David, Peter, Riccardo, Elsa, Manu, Naim, Xavier). In particular, I want to thank Marco Buzio for his technical suggestions.

An exceptional thanks to all the italian CERN friends and colleagues, Lucio Fiscarelli, Giancarlo Golluccio, Vitaliano Inglese, Giuseppe Montenero and Carlo Petrone, for their help and support, and constant presence in every moment (especially in coffee breaks). Special thanks to my current and ex-office colleagues, Domenico Caiazza, for the fruitful discussion during (and after) work, Mario Kazazi, for the work support and funny moments, Giordana Severino, for her kind availability and collaboration in the design of the PCB coils. I'd like to thank also the newcomers, Daniele

for the help to design 3D printer components, Martino, Marco, and Rocio for the nice moments during the coffee breaks. A special thanks to all the colleagues/friends and also co-authors of works, Carlo Baccigalupi, Pasquale Cimmino, Gianni D'Addio, Donato De Paola, Mario Girone, Oliver Koster, Massimo Manna, Alessandro Parrella, Emmanuele Ravaioli, Rosario Schiano Lo Moriello and Vito Vizziello.

A big thanks also to the rest of Geneva friends, Andrea, Carla, Delia, Lorenzo, Marina, Oana and Rossella. I'd like also to thank all my friends in Italy, colleagues of the university studies and all the ex-housemates in Benevento.

In these years, my girlfriend Francesca supported me with her love complying my decisions (following me to Geneva). I'm sure that without her, this experience would not have been achievable...she deserves a very "BIG THANKS".

Finally, I want to thank my family (my parents, my sister, my grandmother, my brother in law, my nephews and Francesca's parents) for their support and love.

Ernesto De Matteis

Contents

Introduction

In quality assurance process for particle accelerator magnets, magnetic measurements are required for checking the field uniformity, the magnetic length, and the extension of the fringe-field region. In literature, the related measurement systems are based on different technologies, like Hall sensors, Nuclear Magnetic Resonance (NMR), and rotating-coil technologies.

NMR transducers are very accurate for the main field, e.g., Metrolab PT2025 NMR [1], with ± 5 and ± 0.1 ppm of absolute and relative accuracy, respectively. However, they are not suitable for gradient measurements (e.g. fringe fields), and have limited lower range of operation (e.g. Metrolab PT2025 probe, 0.043 T) [1]. Often, the NMR transducers support other measurement systems, such as Hall probes, which are are widely used for local mapping of straight and curved magnets [2–4]. Main advantages are high spatial resolution due to the size of the sensing element (e.g. 11 mm^2 for 3D Hoeben electronics [5]), a wide range of field, and the use for non-homogeneous fields both in static and dynamic conditions. Main disadvantages are the relatively low accuracy (0.1%) and the strong temperature dependence of the metrological performance. Moreover, the mechanical limit of these systems, and i.e. the measurement precision, is the difficulty to align the Hall probe characterized to small sensing element, with respect to the mechanical system.

In most cases, the best suited sensor for field uniformity is still the sensing coil, fixed or moving. Main advantages are stable measurement performance, easy calibration procedures for small dimension coils, and multipole-field measurements. Rotating coil systems, such as the D/QIMM [6] (Dipole or Quadrupole Industry Magnetic Measurement) and FAME [7] (Fast Measurement Equipment) systems at CERN, are used for integral field measurement of magnets for the Large hadron Collider (LHC). Regarding curved magnets, the main systems use fixed coils, such as the curved printed coil array [8] and long, curved coils [9], applied mainly to measure field uniformity. Measurement systems based on rotating coils were also applied to curved magnets. As

an example, a 50-cm long rotating coil sensor for testing fast-ramped superconducting magnets is presented in [10, 11]. Moreover, magnets with large acceptance for separators and mass spectrometers [11, 12] require local mapping for track reconstruction.

In this Thesis, a new magnetic measurement system capable of satisfying the abovementioned requirements is presented. The magnetic field mapper is based on the rotating coil method, for localized measurements of magnetic fields and the harmonic multipole content in the magnet ends. The system is composed of a rotating coil transducer and a train-like system for longitudinal positioning inside magnet bore.

In particular, in the *Background* part, the **Chapters 1** and **2** present the rotating coil and the main mapping techniques, respectively, highlighting theoretical and practical aspects. The **Chapter 3** focuses on the rotating coil transducer [13], highlighting its main project aspects. In **Chapter 4**, a method based on Unscented transform [14] for analyzing uncertainty and its sources classification of a generic rotating coil transducer is presented. In the *Experimental results*, **Chapter 5** details the implementation of the main mapper components (transducer and train-like motion system). **Chapter 6** reports the results of the metrological characterization and the uncertainty analysis [14] of the rotating coil transducer. Finally, **Chapter 7** shows and discusses the final measurements of the full bench, focusing on the characterization and the end-field profile measurements.

Chapter 1

Rotating Coils for Measuring Accelerator Magnets

The rotating coils represent one of the most powerful system for measuring rapidly the most useful characteristics of accelerator magnets. In literature, these are based on the so-called harmonic-coil method. This technique is the most accurate, convenient and widely used technique for measuring the harmonic coefficients in accelerator magnets. In fact, the harmonic description of the field is the base for field quality characterization, as well as for particle tracking simulations. The harmonic coefficients are related to the azimuthal variation of the field components, i.e. a rotating loop coil measures the azimuthal variation of the magnetic flux. By the knowledge of the coil geometry it's possible to deduce the field harmonics.

The first part of the chapter presents the theoretical fundamentals of the rotating coil method. In the second part, the experimental setup have been exploited, and in conclusions a short look to the limitations of the method.

1.1 Field Harmonics

Magnetic field quality in the aperture of accelerator magnets is commonly described by a set of Fourier coefficients, known to the magnet design community as field harmonics or multipole coefficients [15]. The method used for the calculation of field harmonics is based on finding a general solution that satisfies the Laplace equation in a suitable coordinate system. The integration constants in the general solution, obtained with the separation of variables technique, are then determined by comparison with the boundary values. The classical method compares the integration constants with the Fourier series expansion of the field components on the domain boundary. In accelerator magnets, the domain boundary is often chosen as a circle with a radius of two-thirds of the aperture radius. A general solution that satisfies the Laplace equation, $\nabla^2 A_z = 0$, can be found by the separation of the variables method. Considering the magnet aperture as the problem domain the general solution for the vector potential is

$$A_z(r,\phi) = \sum_{n=1}^{\infty} r^n (C_n \sin n\phi - D_n \cos n\phi) \tag{1.1}$$

and the field components can then expressed as

$$B_r(r,\phi) = \frac{1}{r}\frac{\delta A_z}{\delta \phi} = \sum_{n=1}^{\infty} n r^{n-1} (C_n \cos n\phi + D_n \sin n\phi) \tag{1.2}$$

$$B_\phi(r,\phi) = -\frac{\delta A_z}{\delta r} = -\sum_{n=1}^{\infty} n r^{n-1} (C_n \sin n\phi - D_n \cos n\phi) \tag{1.3}$$

Each value of the integer n in the solution of the Laplace equation corresponds to a specific flux distribution generated by ideal magnet geometries. The three lowest values, $n = 1, 2, 3$, correspond to the dipole, quadrupole, and sextupole flux density distributions. Assuming that the radial component of the magnetic flux density is measured or calculated at a reference radius $r = r_0$ as a function of the angular position ϕ, the Fourier series expansion of the field components (radial B_r and azimuthal B_ϕ)

$$B_r(r_0,\phi) = \sum_{n=1}^{\infty} (B_n(r_0) \sin n\phi + A_n(r_0) \cos n\phi) \tag{1.4}$$

$$B_\phi(r_0,\phi) = \sum_{n=1}^{\infty} (B_n(r_0) \cos n\phi - A_n(r_0) \sin n\phi) \tag{1.5}$$

where

$$A_n(r_0) = \frac{1}{\pi}\int_0^{2\pi} B_r(r_0,\phi)\cos n\phi d\phi \tag{1.6}$$

$$B_n(r_0) = \frac{1}{\pi}\int_0^{2\pi} B_r(r_0,\phi)\sin n\phi d\phi \tag{1.7}$$

Because the magnetic flux density is divergence free, $A_0 = 0$. In computational practice, the B_r field components are numerically calculated at N discrete points in the interval $[0, 2\pi)$

$$\phi_k = \frac{2\pi k}{N}, k = 0, 1, 2, ..., N-1. \tag{1.8}$$

This allows the calculation of two times N Fourier coefficients by the discrete Fourier transform (DFT):

$$A_n(r_0) \approx \frac{2}{N}\sum_{k=0}^{N-1} B_r(r_0,\phi_k)\cos n\phi_k \tag{1.9}$$

$$B_n(r_0) \approx \frac{2}{N}\sum_{k=0}^{N-1} B_r(r_0,\phi_k)\sin n\phi_k \tag{1.10}$$

These coefficients are usually noted in units (10^{-4}) of Tesla at a given reference radius r_0 (2/3 of the magnet aperture). The normal and skew multipoles $a_n(r_0)$ and $b_n(r_0)$ are related to the main field $B_N(r_0)$ (B_1 for the dipole, B_2 for the quadrupole, and so on). The equations (1.4) and (1.5) become

$$B_r(r_0,\phi) = B_N\sum_{n=1}^{\infty}(b_n(r_0)\sin n\phi + a_n(r_0)\cos n\phi) \tag{1.11}$$

$$B_\phi(r_0,\phi) = B_N\sum_{n=1}^{\infty}(b_n(r_0)\cos n\phi - a_n(r_0)\sin n\phi) \tag{1.12}$$

The magnetic field usually is represented in the 2-D complex plane (x, y) in terms of the complex variable $z = x + iy$. If the trigonometric transformation $(\cos\phi + i\sin\phi)^n = (e^{i\phi})^n = e^{in\phi} = \cos n\phi + i\sin n\phi$, with $n \in \mathbb{Z}$ is applied to Eqs. (1.4) and (1.5) the magnetic field can be represented in Cartesian coordinates as:

$$B_x(r,\phi) = \sum_{n=1}^{\infty}(B_n(r_0)\sin(n-1)\phi + A_n(r_0)\cos(n-1)\phi) \tag{1.13}$$

$$B_y(r,\phi) = \sum_{n=1}^{\infty} (B_n(r_0)\cos(n-1)\phi - A_n(r_0)\sin(n-1)\phi) \tag{1.14}$$

In literature the multipole coefficients are represented in complex notation as

$$C_n(r_0) = B_n(r_0) + iA_n(r_0) \tag{1.15}$$

In the complex plane (x, y) the field representation becomes simply

$$B(z) = B_y(z) + iB_x(z) = \sum_{i=0}^{\infty} C_n(z) \left(\frac{z}{r_0}\right)^{(n-1)} \tag{1.16}$$

Commonly, the harmonic cefficients are indicated relatively to main field component B_N:

$$c_n = 10^4 \frac{C_n}{B_N} = 10^4 \left(\frac{B_n}{B_N} + i\frac{A_n}{B_N}\right) = b_n + ia_n \tag{1.17}$$

where the normalized c_n are expressed in the form of *units*.

1.1.1 Field Harmonics: dipole and quadrupole distribution

A dipole magnet gives an homogeneous field displayed in Fig. 1.1

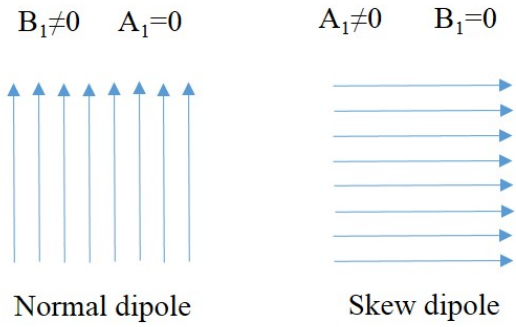

Figure 1.1: Field lines for normal and skew dipole field.

In this case (normal dipole of Fig. 1.1) for $n = 1$ the Eqs. (1.4) and (1.5) yield

$$B_r(r,\phi) = B_1\cos\phi + A_1\sin\phi \tag{1.18}$$

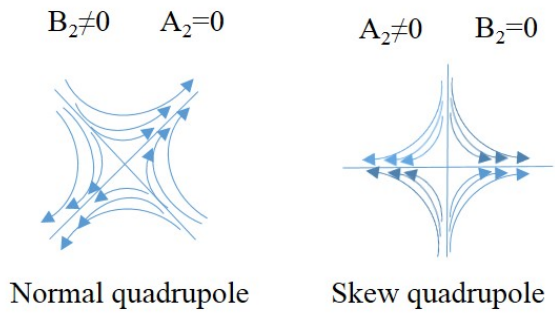

Figure 1.2: Field lines for normal and skew quadrupole field.

$$B_\phi(r,\phi) = B_1 \cos\phi - A_1 \sin\phi \tag{1.19}$$

and the Eqs. (1.13) and (1.14)

$$B_x(x,y) = A_1, \qquad B_y(x,y) = B_1 \tag{1.20}$$

For $n = 2$ (Fig. 1.2) the Eqs. (1.4) and (1.5) yield a quadrupole field distribution, represented as

$$B_r(r,\phi) = \frac{r}{r_0}\left(B_2(r_0)\sin 2\phi + A_2(r_0)\cos 2\phi\right) \tag{1.21}$$

$$B_\phi(r,\phi) = \frac{r}{r_0}\left(B_2(r_0)\cos 2\phi - A_2(r_0)\sin 2\phi\right) \tag{1.22}$$

and

$$B_x(x,y) = \frac{1}{r_0}\left(B_2(r_0)y + A_2(r_0)x\right) \tag{1.23}$$

$$B_y(x,y) = \frac{1}{r_0}\left(-A_2(r_0)y + B_2(r_0)x\right) \tag{1.24}$$

Both components vary linearly with the distance form the origin, and in a normal quadrupole ($A_2 = 0$)

$$B_x(x,y) = gy, \qquad B_y(x,y) = gx \tag{1.25}$$

where g is the gradient ($\mathrm{T}\cdot\mathrm{m}^{-1}$). This kind of field distribution focuses the charged particles of the beam.

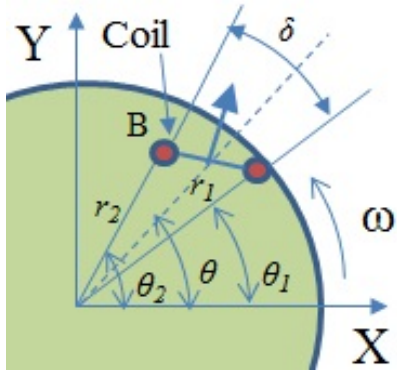

Figure 1.3: Rotating coil: generalized scheme.

1.2 Harmonic coil method

The harmonic coil method has followed the development of the early analog integrators, that forced the measuring coil to rotate stepwise between consecutive angular positions [16]. The method represents the best choice for higher order multipoles measurements within a well-established theoretical frame, such as the circular apertures of superconducting and quadrupole magnets [17]. The method is based on the Lens's law, that says: "If an induced current flows, its direction is always such that it will oppose the change which produced it". In the Faraday's law of induction (Eq. (1.26)), this is shown with the negative sign.

$$U = -\frac{d\Phi}{dt} \tag{1.26}$$

which indicates as the change of the magnetic flux in the time generates an induced voltage with opposite sign, i.e. the induced voltage goes against the magnetic flux change and/or variation.

The magnetic flux can be evaluated integrating the Eq. 1.26 in time

$$\Phi(t) = -\int_{t_1}^{t_2} U dt \tag{1.27}$$

If the field is assumed to be uniform in z-direction and constant in the time, the flux can be written in terms of coil area, A, function of the coil turns, N_T,

$$\Phi = N_T \int_A \vec{B} \cdot d\vec{a} \tag{1.28}$$

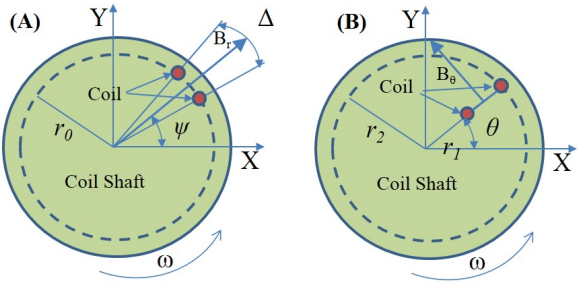

Figure 1.4: Rotating coil: (A) tangential and (B) radial coil schemes.

where Φ is evaluated in $\mathrm{Vs} = \mathrm{Tm}^2 = \mathrm{Wb}$. The coil is perfectly centered in the magnet and rotates rigidly with an angular velocity ω around the magnet axis (Fig. 1.3). Assuming the coil wire infinitely thin, the surface for all the coil turns N_T around the axis is

$$A = N_T l \int_{r_1}^{r_2} dr = N_T l (r_2 - r_1) \tag{1.29}$$

where l is the length of the coil.

Considering the tangential coil scheme in Fig. 1.4A, the magnetic flux at time t is

$$\begin{aligned} \Phi(t) &= N_T l \int_{\psi} B_r(r_0, \psi) r_0 d\psi \\ &= \sum_{n=1}^{\infty} K_n^{tan} \left[B_n(r_0) \sin(n\omega t + n\Theta) + A_n(r_0) \cos(n\omega t + n\Theta) \right] \end{aligned} \tag{1.30}$$

where Θ is the angle of the coil at time $t = 0$ and

$$K_n^{tan} = \frac{2 N_T l r_0}{n} \sin\left(\frac{n\Delta}{2}\right) \tag{1.31}$$

is the coil sensitivity of tangential coil, that depends on the geometrical features of the coil, Δ is the opening angle, and r_0 the measurement coil radius. The coil sensitivity factor are evaluated by calibration procedure, and the field harmonics are obtained by Fourier transform of the flux (1.30). Another traditional scheme is the radial one shown in Fig. 1.4-B. In this case the magnetic flux is induced by the azimutal component of the field, as

$$\begin{aligned}\Phi(t) &= N_T l \int_{r_1}^{r_2} B_\psi(r,\psi) dr \\ &= \sum_{n=1}^{\infty} K_n^{rad} \cdot [B_n(r_0)\cos(n\omega t + n\Theta) - A_n(r_0)\sin(n\omega t + n\Theta)]\end{aligned} \tag{1.32}$$

where the r_1 and r_2 are the coil inner and outer radii. The coil sensitivity factor is

$$K_n^{rad} = \frac{2N_T l r_0}{n}\left[\left(\frac{r_2}{r_0}\right)^n - \left(\frac{r_1}{r_0}\right)^n\right] \tag{1.33}$$

As explained for the tangential coil, the field harmonics can be evaluated by Fourier transform of the flux (1.33).

1.3 Rotating coil systems

The rotating coil systems remain the main instrument to check the field quality of accelerator magnets. The measurement requirements and techniques are very demanding for the optimization and performance analysis of accelerator magnets, and for the manufacturing and assembly tolerances. From this the magnetic measurements assist the production of high field quality magnets, and the goal depends on the accuracy of the desired analysis. In order to achieve the targets given from accurate magnet models, the study and development of more advanced measurement technique and relative systems are going on in all the research centers treating the accelerator machines. At CERN, recent instrumentation and acquisition systems implement high bandwidth and fully automated measurements, for accelerator magnets at warm and cryogenic temperature, satisfying the field quality precision requests from beam optics. For reproducing the relative measurement procedure (1.2), these systems present three main areas to develop: mechanics and automatics, electronics and software.

The mechanics (rotating motor, encoder, shaft, bearings and support, shown in Fig. 1.5) of these systems is conceptually the same in the last years. From the other hand, the manufacturing precision is improved, pushed to more tighten measurement requirements. The electronics, in particular the acquisition block of the coil signals (Fig. 1.5), has seen important progress in this field. At CERN, the Fast Digital Integrator (FDI [18]) was developed for facing the challenges posed by the new generation of fast rotating coils. The scheme of functionality of FDI is shown in Fig. 1.6.

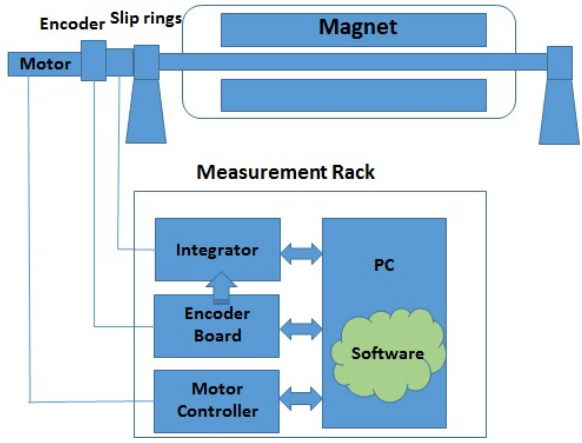

Figure 1.5: General architecture of rotating coil system.

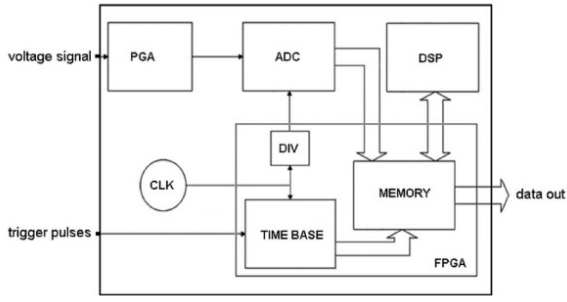

Figure 1.6: Function scheme of Fast Digital Integrator (FDI) [18].

The principle shown in Fig. 1.6, consists in the integration of the input signal voltage in the digital domain, in order to reduce the impact of analog uncertainty sources. A differential gain amplifier (PGA in Fig. 1.6) conditiones the input signal, with self-calibration capabilities. An Analog-to-Digital Converter (ADC-18 bit) digitizes the input signal, and a Digital Signal Processor (DSP) processes the measurement data and supervises the board with a Field Programmable Gate Array (FPGA). About the software, a Flexible Framework of Magnetic Measurement (FFMM) software [19] was developed at CERN. This satisfies wide range of measurement requirements, such as the adaptability and extend-ability for the new applications. The software is installed on a workstation and controls the integrators, the motor rotating the shaft and the magnet power supply.

The systems gives a 2D (or integrated 3D) field distribution, expressed by a series of multipoles. The procedure of the system is composed of the following steps:

1. the motor controller driven by the measurement software actuates the rotating motor of the measurement shaft;

2. the voltage signal induced from the magnetic field is acquired by slip rings and sent to the integrator. In the same time the encoder board receives the pulse signal (square wave, Fig. 1.3) from the encoder;

3. the integrator triggered by the encoder pulses through the Encoder board (decimation and/or multiplication ratio of the encoder pulses) integrates the sampled coil signal in K points aver a full revolution, $\psi_k = \frac{2\pi k}{K}$, where $k = 1, ..., K$. At each sample it's associated an instant time, evaluated and saved by integrator as a number of internal clock pulses. From this the Eq. (1.27), seen by integrator, can be written as

$$\Delta\Phi := \Phi(t_2) - \Phi(t_1) = \int_{t_1}^{t_2} U dt \tag{1.34}$$

substituting the instant time with the relative angular position,

$$\Delta\Phi_m := \Phi(\psi_m) - \Phi(\psi_{m-1}) = \int_{t(\psi_{m-1})}^{t(\psi_m)} U d\psi \tag{1.35}$$

where the ψ_{m-1} and ψ_m are two consecutive angular position triggered by angular encoder. In Eq. (1.35) the $\Delta\Phi_m$ are known as delta magnetic fluxes, and they depend also on the rotation speed of the coil;

4. the magnetic flux through the search coils is obtained as a cumulative sum over the magnetic delta fluxes:

$$\Phi(\psi_k) = \begin{cases} 0, & \text{if } m = 0, \\ \sum_{m=1}^{k} \Delta\Phi_m, & \text{if } k \in [1, K] \end{cases} \tag{1.36}$$

5. Drift correction: the magnetic flux evaluated in Eq. (1.36) must be corrected taking into account the electronic noise of the integrator. The drift correction is realized in the post-processing phase, cnsidering the offset voltage V_0, and the Eq. (1.36) becomes

$$\Phi(\psi_k) = \sum_{m=1}^{k} [\Delta\Phi_m + V_0(t_m - t_{m-1})] \tag{1.37}$$

where the offset voltage is $V_0 = -\frac{\sum_{k=1}^{K} \Delta\Phi_k}{\sum_{k=1}^{K} \Delta t_k}$;

6. the magnetic field B and its multipoles can be calculated as an discrete Fourier series expansion of $\Phi(\psi)$ (Eqs. (1.30) and/or (1.32)), using the coil sensitivity (Eqs. (1.31) and/or (1.33)). Generalizing the field multipoles can be obtained as

$$B_n = \frac{r_0^{n-1} \bar{\Phi}_n}{K_n} \tag{1.38}$$

7. Bucking coil - to increase the resolution of the higher order multipoles, differential coil measurements are evaluated by connecting a series of coils. These coils are known as compensation or bucking coils, and the scheme of series connection depends on the magnet typology (dipole, quadrupole, etc...).

   The signal of the compensation coils must suppress the main field, and this is carried out connected electrically with opposite polarities. The compensation scheme emproves the resolution of the higher order multipoles for three main reason: 1) reduction of the electrical noise and of the errors coming from the offset and non-linear coupling between rotation rate and main field component; 2) avoiding the variations of the magnet power supply; and 3) noise rejection emproved with respect to mechanical instabilities (e.g. vibrations of the shaft, bearings quality, etc...).

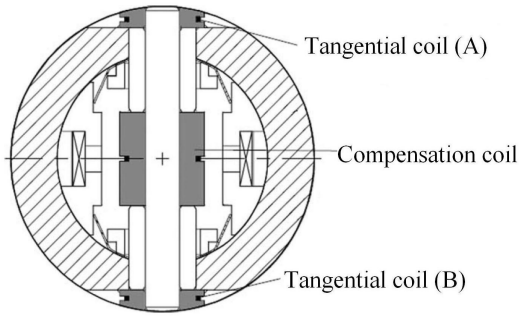

Figure 1.7: Cross section of a tangential coil shaft with dipole compensation scheme, from [20].

1.4 Limitations of the rotating coils

The rotating coil method has some limitation due to mechanical and electronic imperfections. These degrade the measurements of the higher order multipoles. The main sources of limitations/errors can be summarized in the following:

1. imperfections in the rotation of the coil (vibrations and disalignment) due to quality of mechanical components, such as shaft, ball bearings and supports;
2. coil angle error due to angular encoder or to torsion of the coil shaft;
3. coupling of the voltage integrator offset with the irregular rotation rate of the shaft;
4. magnet current instability during the measurements;
5. coil cross sections with respect to magnet geometries.

Regarding the first point, the mechanical imperfections can generate lateral movement of the rotating coil, inducing non-linear coupling on the higher order harmonics (quadrupole, sextupole, etc...) and consequently increasing the uncertainty of the measured harmonics. The encoder quality and the eventual torsion of the shaft increases the uncertainty on the pulse triggers. The integrator usually presents a voltage offset that gives a flux error inversely dependent to the rotation rate. This effect can be eliminated evaluating an average offset over a turn, when the field is static during the coil rotation. The power converter of the magnet mujst be stable. In fact, the exticing current must be in the range of ppm to 10 ppm, in order to avoid high-order multipoles on the turn. In this sense, the acquisition of the current value for each

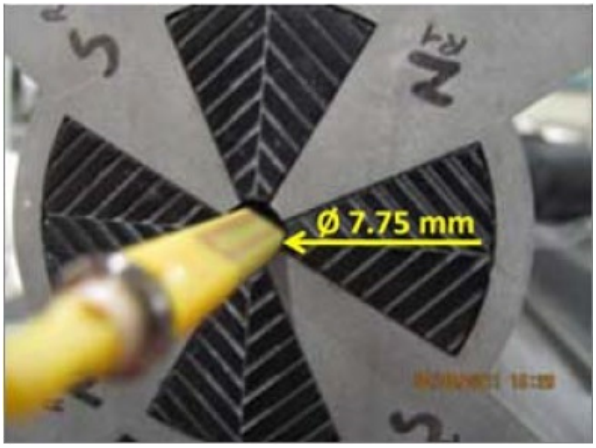

Figure 1.8: Printed circuit board coil shaft (7.75 mm) in small aperture magnet.

increment, and a first order correction are necessary to emprove the measurement quality. The transfer funtion (integral field divided by the current) and the field strenght measurements are insensitive to electronic and mechanical noise sources. However, the calibration of the coil surface influences the dipole measurement and the positioning of the coils on the shaft the quadrupole and higher order ones.

Regarding the last point, the traditional rotating coil cannot be used in the following cases: i) for magnets with small-aperture (height less than 20 mm, Fig. 1.8); ii) for curved magnets; iii) in case of magnets with horizontal apertures much bigger than height; Moreover, the rotating coil method is not able to measure pulsed fields,when the variation of the field in time ($\Delta B/\Delta t$) is not negligible on a coil revolution.

Chapter 2

Magnetic Field Mapping

The magnetic field mapping is the reproduction of magnetic fields on a map or images. The design and optimization of accelerator magnets is carried out by magnetic field maps, in particular for mass spectrometers and separetors. Usually, the mapping is relied one point at a time with various measuring methods. The methods and technologies of magnetic field mapping are the focus of this chapter. How reported in [21], the measurement methods have remained unchanged for a long period, while the instrumentation was subjected to continuous progress. This chapter, complementary to the previous one, analyses only the more common methods (Hall element, Fluxmeter, and NMR).

2.1 Mapping measurement technique

Different measurement methods are avaialble for magnetic field mapping. The criterion to choice the more suitable depends on the application and in particular on the requirements of the magnetic field to be mapped. As reported in [22] the main features to check are i) the field measurement range, ii) reproducibility and accuracy, iii) mapped volume and field geometry and, iv) time bandwidth. In some case the choice of the suitable method is conditioned from non-magnetic features, such as the operation temperature and/or the measurement volume, limiting the selection of these.

2.2 Nuclear Magnetic Resonance

The Nuclear Magnetic Resonance (NMR) represents the standard for the measurement of homogeneous magnetic fields. They commonly achieve accuracy of 0.1 ppm, for this the NMR is considered today the primary standard for calibration [22]. The field measurement of the NMR probes is based on the measurement of the precession frequency f of the particles (Fig. 2.1) in a sample places in the magnetic field. This principle follows the Larmor equation

$$f = \gamma B \tag{2.1}$$

where f is the precession frequency of the particle (Fig. 2.1), γ is the gyromagnetic ratio (constant for each particle), and B the magnetic field. Measuring the frequency f for proportionality is possible to deduce the magnetic field. The high accuracy of the frequency measurement, fractions of ppm, allows to achieve high accuracy also for magnetic measurements. The NMR is very sensitive to the local magnetic field, and in particular to field gradients. The change of the local field in the particle sample of the probe generates a change of the resonant frequency (Eq. (2.1)). In this condition the field gradient into the resonating sample must be kept below thight bounds.

Different techniques are used to measure the precession frequency: continuos wave (Q-meter), Impedance (Z-meter), and Pulsed Magnetic Resonance [22].

The range of NMR measurements depends on the frequency range of the electronics instrument (RF technology, freq. range from 1 to 100 MHz) and of the sensing material of the probe (fractions of mT using an Electron Paramagnetic Resonance probe up to 10 T using a deuterium probe). The accuracy depends mainly on the method used to measure the precession frequency, and especially on the measurement

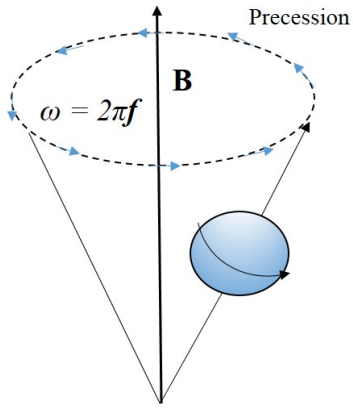

Figure 2.1: Larmor precession scheme: the particle, immersed in an homogeneous magnetic field B, precesses with a frequency f.

time of this. As an example, the continous wave technique can reach 0.1 ppm for 10 s of the measurement time, and 0.5 ppm for 1 s. The uncertainty of the measurements depends on the uncertainty of frequency measured that raches a few *ppb* for long time of data acquisition. The gyromagnetic ratio is constant in a broad range of temperature, but it can change depending on the current state of particle. This could represent a source of uncertainty, but after the calibration, the error is smaller than the resolution of the frequency measurement. The volume of these probes varies between the 10 and 100 mm^3. Regarding the magnetic field mapping, the main limitation of the NMR probes is the necessity to have an homogeneous field, and to be constant in time and uniform through the sensing volume. The maximum field gradient for a probe of a few mm varies between the 10 and 100 ppm/mm, depending on the size and material used for the probe. Higher gradient magnetic fields can be measured by using compensation coils [22].

2.3 Fluxmeter

The fluxmeter method represents the oldest method for magnetic measurements and also the most precise for determining the magnetic flux lines. It is based on the induction law (2.2), shown in Fig. 2.2, where the source of the magnetic field (B) and the coil (Area S) must move relative to each other to generate a changing potential across the coil(s) (2.2) and measurable flux output (1.36). An instantaneous output voltage can be provide by fluxmeter. The accuracy (a few tens of ppm)of this system

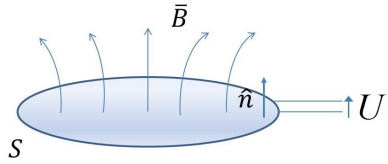

Figure 2.2: Induction Law.

depends on the coil-integrator assembly, that must be calibrated in a homogeneous magnetic field by reference to a nuclear magnetic resonance probe. The introduction of the digital integrator has made possible to acquire integrated potential difference with high accuracy. The coil geometry is customized for the particular measurement, and such as for straight magnets, also for curved dipole magnets, the measurements can be perfomed using fixed coils in a dynamic field or moving the coils in a static field.

$$U = -\frac{d\Phi}{dt} = \int (\frac{\delta \vec{B}}{\delta t} + (\vec{v} \times \vec{B}))dS \tag{2.2}$$

$$\Phi = \int_S \vec{B} \cdot \vec{n} ds \tag{2.3}$$

As shown in Eqs. (2.2) and (2.3) the variation of the magnetic field dB/dt can induce a voltage V on the coil. A voltage can be induced also by a change of the orientation of the coil dS/dt. The second solution, i.e. moving coils, is used in static magnetic fields. The precision of the movement is fundamental for the field measurement quality, and for this only simple movements are usually used (translations, flip of 180 degrees, and continuous rotation as described in Chap. 1). Both the solutions, moving and fixed coils, have been used for cryogenic and room temperature measurements.

The maeasurement of magnetic flux as described for rotating coil in Chap. 1, requires the integration of the Eq. (2.2):

$$\Phi_e - \Phi_s = -\int_{t_s}^{t_e} U dt \tag{2.4}$$

where the t_s and t_e are the start and end time of measurement, and Φ_e and Φ_s are the magnetic flux measured respectively. This integration can be realized by three different technique: analog, digital or numerical integration [22].

Induction coils The fluxemeter method is implemented by fixed or moving coils. These are built using an insulated conductor with small diameter on a non-conducting support (composite materials, fibreglass, plastics, glasses and ceramics). The material of support must have low thermal expansion and a mechanical stiffness in order to achieve a good coil calibration. The winding technique, the proper tension of the wire, and the geometry of winding are other important points for having reproducible and stable measurements, and calibration of the coil sensitivity to higher irder harmonics.

The coils can be classified in base of their form and extension in space, as [23]:

1. point coils used to measure the magnetic field at a small point in space;
2. line and area coils for measuring integrated field along a line or on a flat region of space;
3. harmonic coils, that are an assembly of line or area coils (described in the Chap. 1).

Calibration After the manufacturing the coils usually present tolerances and imperfections deviating from the ideal ones. The coil calibration represents the main solution to these problems. Usually, the coil is calibrated using a reference magnet, and comparing the measurements with NMR probe ones.

Field measurements As anticipated in previous paragraphs, the field measurement by fluxemters is performed in two mode: induction coil fixed, in case of changing field, or moving the coil in a static field.

The measurements made by fixed coils provide the reset of the integrator at the start. The integration lasts until the flux change is readout. The field change (measurement) is carried out from the flux change measured and the surface coil obtained from calibration. As shown in Eq. (2.4), the fixed coil measurement can carry out only the flux change in a interval time, i.e. relative measurements. To obtain an absolute measurement the magnetic field at start must be zero. Pratically, the integrator can be electronically triggered during the measurement period, and the voltage offset of the integrator input must be reduced. The offset gives an apparent field drift, clearly visible for long integration times. The offset can be trimmed when the induced coil voltage is zero, or the measurement spans a constant field.

The moving coils are used when the field is constant and the induced voltage is generated moving the coils. Also in this case the integrator must be resetted before movement. The final reading depends only on the final and starting position of the

coil, i.e. it's independent of the motion path. In literature these coils are known as translating, and/or sliding coils. The measurement starts outside the magnet (zero-Gauss region) and finishes in the magnet bore, so the total flux variation can be used to evaluate the absolute field. Flipping the coil, rotating it of 180 degree during the measurement, is an alternative technique of this class. The flip coil measures the flux change that is twice the coil flux in the initial position, and in a static dipole field, the absolute field can be deduced by this. As for fixed coils, the moving and flip coils are sensitive to voltage offset of the integrator. Considering the stationary nature of the field measured by these the drifts can be easily corrected (reversal movement of the coils). The resolution of these coils can be increased by using differential measurements (coils connected in opposition, or one coil fixed and the other one in motion). Differential measurements can compensate also current fluctuations of the magnet powering, and toincrease the sensitivity for field quality

Alternative method is the stretched wire technique [24,25] also based on induction measurement. The sensing element is a thin wire of high strength, stretched inside the magnet bore, and a second wire ins laid fixed outside the magnet, providing the return connection of this single-turn coil. High precision stages move the stretched wire in the magnetic field, inducing a voltage signal by the flux cutted, as the moving coils. The accuracy is strongly dependent on the positioning precision. This technique is used in special magnet geometry, strong magnets with small apertures and quadrupole fields for absolute calibration.

Finally, the rotating coils, already described in Chap. 1, represent one of the most successful methods in the measurement of field and field quality for accelerator magnets.

Range and accuracy The induction coils are linear devices, and the sensivity of these can be customized in fucntion of the magnetic field to measure. For this feature, the fluxmeter method has big potentialities, covering broad range of field measurement. The main limitation of this method are the electrical noise (thermal and environmental ones), drifts from electronic (e.g. integrator) and mechanic quality (e.g. rotating coils, stretched wire, and moving coils). Regarding the range of application, the lower limit (minimum field) is about 0.1 μT, and there is no limitation for the upper one.

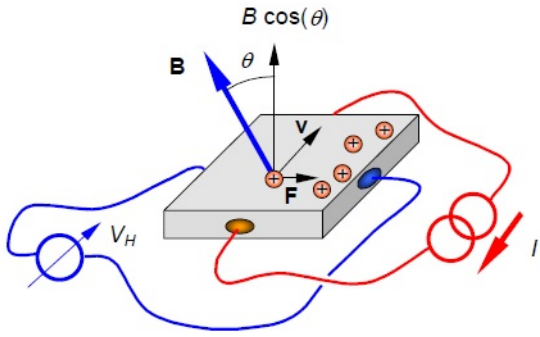

Figure 2.3: Scheme of an ideal Hall generator and the appearance of Hall voltage [22].

2.4 Hall Generator

Principle The Hall generators measure the magnetic field through the effect of this on the charges/current in a conducting material. The method of Hall generator provides to insert in the magnetic field B to be mapped a suitable material with an electric current flowing. As shown in Fig. 2.3, a thin slab is placed in a magnetic field B. Considering the normal component wrt slab, $B\cos\theta$, the charge carriers are subjected to a force F, transversal to the direction of these. The amplitude of this force is:

$$F = qvB\cos\theta \tag{2.5}$$

where v is the charge velocity and q is the charge of each carrier. The force F tends to polarize the charges in its direction, resulting in the occurrence of an electric field. At equilibrium, the electric field balances the effect of the magnetic field, generating the Hall voltage V_H. The magnitude of this is proportional to magnetic field, normal to the surface of the slab and to the electric current (Fig. 2.3). The Hall voltage can be written as

$$V_H = GR_H IB\cos\theta \tag{2.6}$$

where G is a factor depending on the geometry of the Hall generator, R_H is the Hall constant of the material, and I is the electric current flowing in the slab.

Non-linearity and parasitic effects The Hall generators show different non-linearity and parasitic effects due to design and manufacturing of Hall element (ge-

ometry, connector size, material), strong dependence wrt operation temperature and planar effect of the element.

The Hall generators are fabricated in printed circuit technology that provides direct connection on board. For this reason, usually, the terminals and connectors are bigger than the Hall generator. This deforms the flow of current within the material and consequently the electric field of the hall voltage. For the finite geometry of the contacts and the shunting effect of these on the current, the Hall generator shows also a non-linear response to the field, due to the geometric factor G. Strictly connected to this effect, a Hall generator has a material non-linearity, attributed to the R_H Hall coefficient. Both the non-linearities can be compensated choosing the proper geometry and material combination. As an example, the cruciform geometry of the Hall generator represents a solution with a better linearity of the classical rectangular generator. Another source of non-linearity of the Hall generator is the strong performance dependence with respect to the temperature. Indeed, the Hall coefficient R_H depends on the temperature with a range of variation of $100 - 1000$ ppm/C. The compensation of this effect is made by a controlled heat source in the Hall generator. As shown in Eq. (2.6), the Hall voltage depends on the direction of the magnetic field. This voltage is maximum when the field is normal to the slab $\theta = \pi/2$, while it should be zero in case of the field is parallel. Vice versa, the anisotropy of the generator material leads to non-zero voltage. This effect is known as the planar Hall effect, that depends on the strenght of the field and on the angle between the magnetic and electric field in the generator. The main consequence of this effect is the occurrence of an additional voltage at the terminals.

At cryogenic temperature there are special Hall generators, that present an additional problem at low temperatures. The so-called Shubnikov-de Haas effect [26] generates an oscillation of the Hall coefficient, causing a deviation of about 1% at high fields.

A voltage offset occurres at zero applied magnetic field as a parasitic effect due to misalignment of the voltage terminals, metal-semiconductor connections and/or doping density of the material. This offset is temperature dependent, and it can reach values of about $0.1 - 0.001$ V. A control and a compensation must be implemented to achieve good results.

Field measurement with Hall generators The Hall generator is a four terminal device, two for the current source, and two for the Hall voltage meauements. The current is supplied by very stable source (AC or DC), and the Hall voltage is measured

by an high impedance voltmeter (and conditioning circuit). The source of current must be isolated from the reading of Hall voltage by a differential input amplifier, avoiding stray current in the generator. The noise rejection of the Hall voltage is increased by AC excitation and lock-in techniques, where the voltage is synchronously readout with the modulated source of current.

The Hall voltage measured is converted to the relative magneic field by a function. The function is established by a calibration procedure, through a known magnetic field. The precision of the measurements is emproved considering also the temperature compensation. This correction is implemented by a thermostat surrounding the hall generator. In this way the calibration takes in account automatically the working temperature. Another important issue before to use an Hall generator is to establish the alignment of this. Indeed, this element are sensitive to the field normal to the slab, and an eventual disalignment can result in a measurement error (apparent reduction of the strength). The solution for this problem is to identify the maximum reading of the generator tilting it in the field.

Arrays of Hall generators for three-dimensional measurements of the field are available on the single chip, reppresenting the best solution for magnetic field strength measurements.

Finally, in order to have high precision measurements, the voltage offset must be compensated. This can be removed placing the Hall generator in zero-field chamber, and measuring it. In any case, the measurements must be stabilized in temperature, preventing the drift in the offset caused by gradients of temperature.

Range and accuracy Considering the last technological development in printed circuit, the Hall generators have become the less expensive device for magnetic field mapping in industrial and research applications. This instrument shows a wide range of strenght and shape, the possibility to use it in dynamic and static measurements. The range of field that cna be measured by Hall generators depends on the sensitivity of the material and on the voltage measurement capability. The sensitivity varies not only with the material, but depends also on the thickness and the size of active area. The typical sensitivities are in the range of 10 mV/T to 1 V/T, and the magnetic field measurement range is above 1 mT. Using high precision voltmeters it's possible also to have accurate voltage measurement (range μV), allowing magnetic measurements better than 0.1 μT. The accuracy of the Hall generators is dictated by the non-linearities (e.g. temperature dependence), the parasitic effects, and alignment errors. The typical accuracy is of 1000 ppm, and applying a custom calibration (temperature

control and various compensation) it can be achieved an improvement of factor 10 and in the last development of a factor 100 of reading. Other factor is the long term stability of the Hall-probe, that can be emproved by a weel- designed assembly of the probe, and by keeping constant the temperature. The mapped volume is determined from the sensing area of the Hall generator, that has volumes in the range of 0.01 mm^3 to 0.1 mm^3. The time resolutions are below 1 ns. The main bandwidth limitation is given by the precision voltmeter (commercial devices bandwidth up to 500 Hz).

Chapter 3

The Rotating Coil Transducer

A rotating coil transducer for local measurements of magnetic field quality in magnets is proposed. The transducer is based on

- a set of reduced-dimension rotating coils, for a spatial resolution typical of Hall sensors, as required for beam-physics codes that consider space-charge limits,
- an accurate transport system for longitudinal displacements inside the magnet aperture, and
- components with magnetic compatibility to avoid interference with the measured magnetic field.

This allows magnetic measurement requirements arisen from recently developed compact accelerator systems (with curvature radii of less than 5 m) for biomedical applications and physics research to be satisfied. In the following chapter, *i*) the *requirements*, *ii*) the *conceptual design*, *iii*) the *transducer architecture*, and *iv*) the *coil design*, based on the printed circuit board technology, of the proposed rotating coil transducer for magnetic field mapping are illustrated.

3.1 Requirements

The main requirements of a rotating coil transducer for field mapping are the ability to measure fringe fields, local distributions, end field, and the flexibility to adapt to different mechanical configurations, magnet apertures and curvatures. Therefore, the transducer must be: (i) small, typically 200 mm or less in length and 50 mm or less transversally; (ii) able to work inside the magnet aperture, completely immersed in the magnetic field; (iii) able to accommodate sensing coils of a few mm thick and (iv) light than 1 kg, to allow easy motion and low positioning error. Another important requirement is the need to measure precisely the angular position of the coils. This is necessary both statically, for fixed-coil measurement of pulsed magnets, and dynamically for conventional harmonic coil measurements. The longitudinal position of the transducer inside the magnet aperture must be known with a precision of $\pm$ 100 μm or better. The requirements on the measurement result, expressed in terms of the uncertainty of the harmonic components of the magnetic field, vary according to the specific application. Typical relative targets are in the range of a few hundreds of ppm with respect to the main field.

3.2 Conceptual design

The design of the transducer is driven by the following main aspects: *magnetic compatibility*, *manufacturing precision*, and *compact size* of all the components.

Magnetic compatibility of components is necessary to avoid field perturbations during the measurement or displacements of the sensor due to electromagnetic forces. Consequently, the transducer was realized free of ferromagnetic and highly conducting parts to avoid magnetization and eddy currents.

The *manufacturing precision* is fundamental to have low dimensional tolerances. As described in [27, 28], high rotation speeds could increase mechanical instability in traditional rotating systems [6, 7]. Specifically, speed variations must be analyzed experimentally in order to check the rotation stability and the related measurement errors on the harmonic analysis.

The *compact size* of the transducer improves the spatial resolution of coil measurements. In this case, according to recent developments on printed circuits [29], the coil can actually be made very compact without significant quality loss. Considering the systems presented in [6, 7], the 1-σ relative repeatability (relative standard deviation over several revolutions) of dipole magnetic measurements is less than $\pm 10^{-4}$. More-

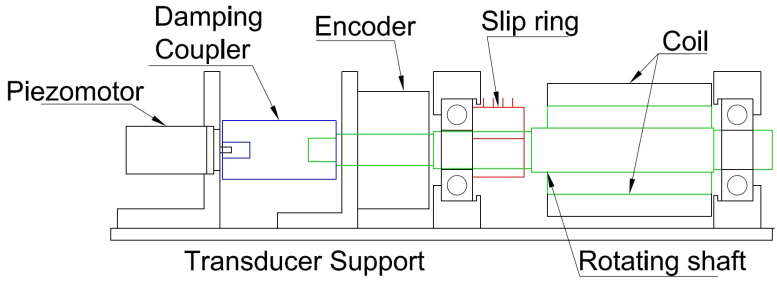

Figure 3.1: Transducer architecture.

over, the rotation and mechanical instability effects must be considered and related to the measurement results of field quality.

The key, here, is to choose compact and magnetically compatible components. Non-magnetic components, like piezoelectric drives, were investigated. Optical encoders with plastic code wheel are the most compact and promise the best technical specifications (high counts per turn) and angular position accuracy. The coils must be compact, on the order of a few cm, but with a large total surface for acquiring the signal with high signal-to-noise ratio. This requires a high precision in the mechanical parts such as the support, coil shaft, ball bearings and coupling. The choice of non-magnetic and -metallic material is fundamental, as well as the avoidance of vibrations and rotary transmission.

3.3 System Architecture

The above requirements have been satisfied by the architecture shown in Fig. 3.1: a piezomotor, an angular encoder, and a rotating shaft carrying the sensing coil are mounted on a non-magnetic aluminum support. A preliminary prototype made of Plexiglas did not show suitable mechanical stability. A plastic coupling between the motor and the encoder allows motor vibrations to be damped. Moreover, slip rings contacts are provided for voltage signal transmission.

3.4 Coil Design: Printed Circuit Board

As described in the first part of the Thesis (Chapters 1 and 2), the rotating coils represent the main transducer for harmonic multipole fields. Their accuracy depends

on the knowledge of the coil geometry (position of the windings) and on the quality of manufacturing (coil stiff and straight), in order to buck the fundemantal field [29] and suppress the vibrations effects. Considering the multiplicity and diversity of accelerator magnets, the coils should be easily customized to the magnet under test in terms of length, number of turns, radius, etc. In laboratories and test facilities of accelerator machine, the rotating coil with wire loop are the main instrument for measuring the harmonic field quality. The use of this technology requires high precision manufacture, with well-equipped labs and skilled technical personnel. In general, the construction of a new probe requires time and costs. Depending on the application, the coil must be designed in terms of the measurement requirements (type of magnet, field strength, and so on). Moreover, all the procedure needs for a dedicated staff, increasing the costs. One of the main advantages of the PCB technology is the possibility to realize compact size coils (lenght and width of fews millimeters) also with a big relative surface ($0.2 - 0.5$ m^2), by exploiting the multilayer solutions ($10 - 30$ overlapping layers for $2 - 3$ mm of board depth). Other fundamental feature of PCB technology is the precise knowledge of the coil track positioning. On the surface, the trace positions of the PCB is very high, $1 - 2$ μm, and the probes can be constructed planar considering a radial configuration (1). About the possibility to mount tangentially the coils, the mechanics and the manufacturing become predominant in the accuracy of the coil, in particular for the bucking. Regarding the Thesis project, the final coils were designed using the PCB technology. Especially, the design was centered on the following measurement requirements: magnet type to be measured, maximum and minimum strength of magnetic field, and geometry of magnet aperture. The measurement system is oriented to measure locally the field, and in principle for straight and curved magnet geometry. From this, the magnet type is a dipole and/or combined magnet, such as the reference dipole of magnetic measurement section at CERN (C-shape magnet, aperture height 80 mm, field range $0.0 - 1.0$ T), and the bending dipole magnet [30] MBR (C-shape curved, nominal field range $[0.042 - 0.420]$ T, aperture height of 75 mm) for ELENA (Extra Low ENergy Antiproton Ring).

The design has considered a radial configuration with a main coil for absolute dipole measurement, a compensation coil for the dipole component, and a spare one (Fig. 3.2). A quantitative analysis of the voltage signal was considered before to decide the geometry of coil tracks, in order to fix the acceptable coil surface. From the Eq. 1.26, the measurement flux quality depends on the level of the coil voltage signal induced form the magnetic field. Considering the electrical noise is about of 50 μV, and the measurement requirement of 1 *unit* on the harmonic field, the

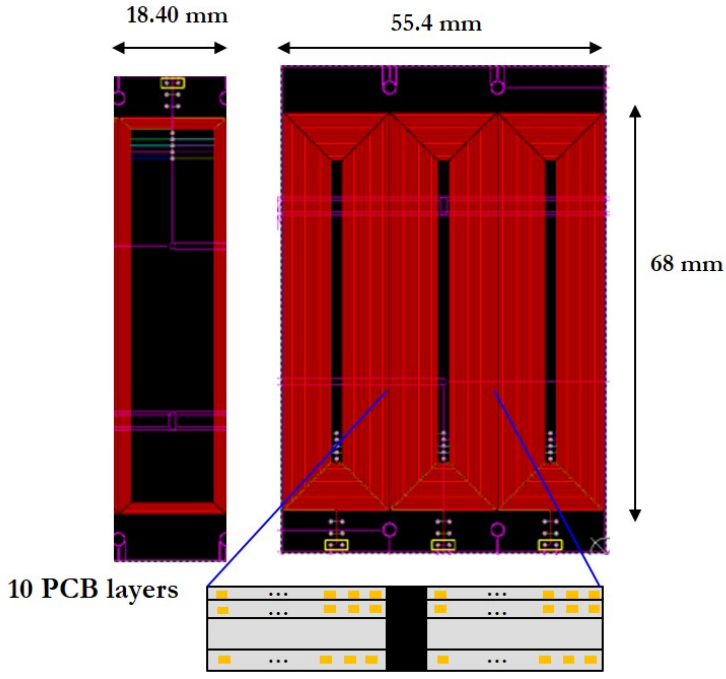

Figure 3.2: Printed Circuit Board coils: (A) design made by 41 tracks per layers nad (B) 10 tracks per layers.

voltage signal should be bigger than 150 mV. To establish this voltage, the following quantitative formula can be used:

$$U \approx \omega A_c B_{min} \tag{3.1}$$

where U is the strength of the voltage signal, ω is the angular speed of the rotating coil, A_c is the coil surface, and B_{min} is the minimum strenght of the magnetic field (to be measured). Considering the abovementioned voltage, the minimum magnetic strength $B_{min} = 0.042\ T$ (Elena curved dipole), and an angular speed of at least 2 rev/s, the relative surface coil should be

$$A_c \approx \frac{U}{\omega B_{min}} = \frac{0.15}{2\pi \cdot 2 \cdot 0.042} = 0.28 m^2 \tag{3.2}$$

From this analysis, the design made by Altium (Giordana Severino, PhD student, PACMAN project - CERN) has provided for three radial coil with 10 PCB layers, 41 tracks (Fig. 3.2-A), sizes of 18.4 × 68 × 1 mm and total magnetic surface of 0.258030 m^2. A second design (Fig. 3.2-B) with 10 tracks per layer and total surface of 0.108030 m^2 was considered to compare the results with respect to the other design and to check experimentally other aspects, such as the so-called endprobe effect [29].

Coil sensitivity The coil sensitivity of the proposed design follows the radial coil sensitivity, as reported in Eq. (1.33). Taking in account the geometry of the single layer (Fig. 3.3), a relative coil sensitivity h_n per unit length can be defined as the following

$$h_n = \frac{K_n}{LR^{(n-1)}} \tag{3.3}$$

where K_n is the radial coil sensitivity (Eq. (1.33)), L is the mean length of the coil and R is the reference radius. These can be evaluated as a cumulative sum of each track (loop of the layer) and formalized in the following equation

$$h^*(m) = \begin{cases} 0, & \text{if } m = 0, \\ \sum_{i=1}^{m} [h_n(i)], & \text{if } m \in [1, N_{tracks}] \end{cases} \tag{3.4}$$

As reported in Fig. 3.3, the sensitivity of the coil presents a non-linear behaviuor in the endprobe part, increasing by the harmonic order. The nonlinearity of the

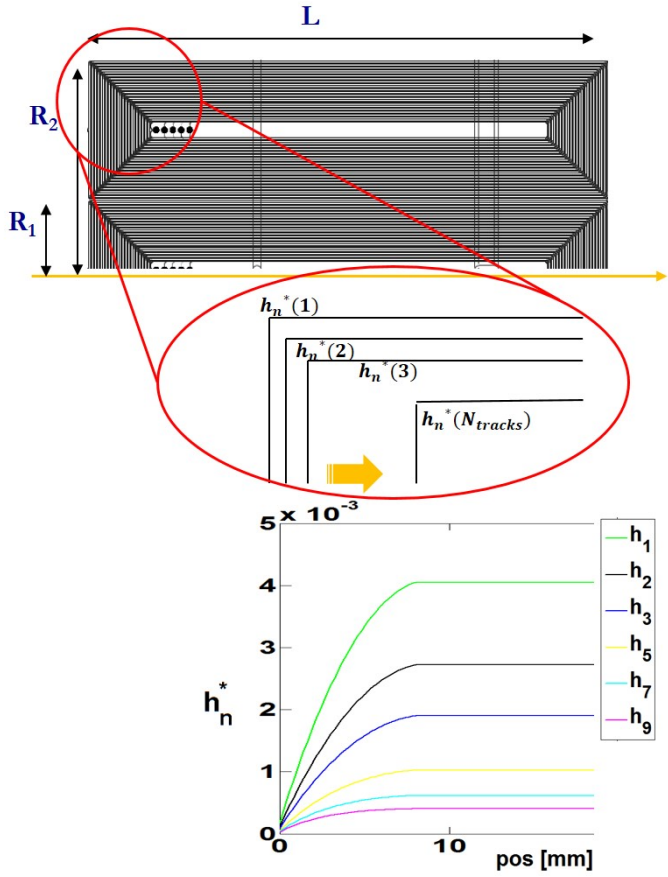

Figure 3.3: Relative PCB coil sensitivity: non-linear effects of the end-probe with respect to harmonic order.

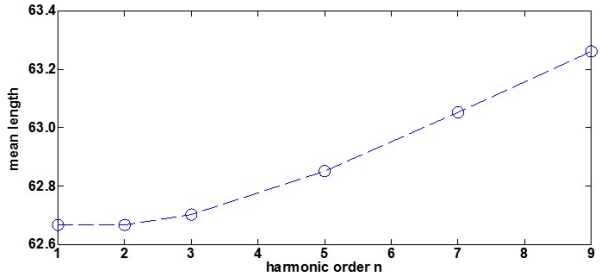

Figure 3.4: Effect of the coil design on the magnetic length order by order.

coil response due to the geometry involves a different magnetic length of the coil for each harmonic order (Fig. 3.4). This effect must be taken in account during the measurements. In particular, the critical points to be resolve are two fold: when the coil is completely immersed into the magnetic field, and the coil is into the fringe field of the magnet. The first one is related to the interpolation of more measurements for reconstructing the integral field locally or on the full aperture length. The solution could be to interpolate the measurements taking into account the magnetic length of each order (Fig. 3.4), and scanning the magnet in function of these lengths. Regarding the second situation, the nonlinearities of the fringe field and of the coil response could be resolved carrying out a scanning of the field on closely displacement of the coil, i.e. fitting of the longitudinal profile of the multipoles on many points.

Chapter 4

Uncertainty Model

The uncertainty of a rotating coil transducer for magnetic field mapping [13] is analyzed. Unscented Transform [31] and statistical design of experiments are combined to determine magnetic field expectation, standard uncertainty, and separate contributions of the uncertainty sources. For nonlinear models of measurement systems, the Unscented Transform-based approach turns out to be more suitable and error-proof than the linearization underlying the "Guide to the expression of Uncertainty in Measurements" (GUM) [32]. For nonlinearizable models, the lack for model approximations and derivative computation strongly reduces computational burden with respect to Monte Carlo-based methods proposed in the Supplement 1 of the GUM [33]. The design of experiments and the associated statistical analysis allow the uncertainty sources domain to be explored efficiently, as well as their significance and single contributions to be assessed for an effective setup configuration.

After illustrating the uncertainty analysis and its application to the rotating coil transducer, the chapter is completed by a straightforward experimental case study. The results (see Chapter 6) show the possibility of reducing measurement uncertainty more than 25 times with respect to the worst condition, if the coil relative uncertainty is decreased by one order of magnitude. Moreover, by means of only 18 trials and the related processing, results corresponding to 10^5 Monte Carlo simulations are achieved.

4.1 Overview

Magnets are qualified by considering the global uncertainty of the measurement bench [34]. In high-energy physics applications, the main field should be measured with a typical relative uncertainty of 100 ppm for dipoles, and 1,000 ppm for quadrupoles. Thus, in measurements at cryogenic temperature, the main field relative uncertainty [35] was less than 100 ppm (dipoles and quadrupoles), while for higher harmonics, lower than 10 ppm. For magnetic axis measurements, the total uncertainty of different methods is evaluated in [36]. The relative magnetic center change of a quadrupole was measured through a rotating coil system, by sub-micrometer uncertainty [37].

The rotating coil measurement errors were defined analytically in [38]. The measurement uncertainties of rotating coils were estimated in [39] for a simulated system, by highlighting construction tolerances, rotational speed variation, and electronic noise. In [40], the uncertainty on radius and area of coils calibrated by the so-called in-situ technique was analyzed according to the GUM [32] through the classical propagation law, or in other cases, by scaling and combination laws [34,38,39]. The standard approach of the GUM uses the law of propagation of uncertainty (LPU) [32], namely the first-order Taylor series approximation of the variance, not suitable for nonlinear measurement model [41, 42]. When models are not linearizable, or the probability density function (*pdf*) for the output quantity departs appreciably from a Gaussian or a scaled and shifted t-distribution (e.g. due to marked asymmetry), the Supplement 1 to the GUM proposes a Monte Carlo approach [33]. Independently of the application, also other approaches, such as fuzzy variables [43, 44], higher-order Taylor series approximations [45], and Monte Carlo simulations [32, 46, 47], were proposed.

Another approach exploits the Unscented Transform (UT) [31, 48], according to the underlying key idea that *"it is easier to approximate a probability distribution than an arbitrary nonlinear function or transformation"* [49]. This approach has proved to be very suitable to simulated and indirect measurements represented by a nonlinear model, assessing its reliability and efficiency with respect to the Monte Carlo approach proposed in the GUM's Supplement 1 [33]. Furthermore, for rotating coil transducers, differently from the uncertainty estimation, procedures for assessing the significance of the uncertainty sources have not been investigated yet. Conversely, this topic is fundamental in the design in order to focus the main uncertainty sources and effectively reduce their impact.

In this chapter, a procedure based on Unscented Transform and statistical design of experiments is proposed for uncertainty analysis, as well as for significance assessment and classification of uncertainty sources, of rotating coil transducers. This approach

turns out to be more suitable to the nonlinear model characterizing the considered magnetic measurements, while the design of experiments allows the associated uncertainty source domain to be explored efficiently in order to assess their significance. In this first analysis, the application is made as much as possible straightforward for the sake of the clarity, and vibrations and manufacturing tolerances, not directly considered in traditional measurement models, are omitted.

In the following, section 4.2 presents the method for analyzing the uncertainty of a generic rotating coil transducer. A case study on a rotating coil for field mapping [13] is shown in section 4.3. Subsections 4.3.1 and 4.3.2 report the uncertainty estimation and its sources classification, respectively. The results of uncertainty computation, validated with respect to the experimental characterization reported in [13], are reported in Chapter 6.

4.2 Method for Uncertainty Analysis of Rotating Coil Transducers

4.2.1 Background on rotating coils

Considering the configuration of Fig. 4.1, the radial component B_r of the magnetic field is measured at a reference radius r_0, as a function of the angular position ψ. The Fourier series expansion [15] of the field components are obtained as

$$B_r(r_0, \psi) = \sum_{n=1}^{\infty} (B_n(r_0)\sin(n\psi) + A_n(r_0)\cos(n\psi)), \tag{4.1}$$

where, considering a numerical discretization on the circle by S steps (Fig. 4.1),

$$\psi_s = \frac{2\pi s}{S}, s = 0, 1, 2..., S-1, \tag{4.2}$$

and the harmonic coefficients are

$$A_n(r_0) = \frac{2}{S}\sum_{s=0}^{S-1} B_r(r_0, \psi_s)\cos(n\psi_s) \tag{4.3}$$

$$B_n(r_0) = \frac{2}{S}\sum_{s=0}^{S-1} B_r(r_0, \psi_s)\sin(n\psi_s) \tag{4.4}$$

In the configuration of Fig. 4.1, the coil measures the main magnetic field B_1, with null skew component A_1, even without compensation. The coil is sensitive to higher-order components depending on the opening angle Δ [50].

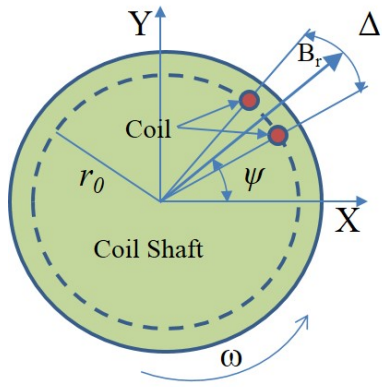

Figure 4.1: Rotating coil 2-D frame: tangential coil view.

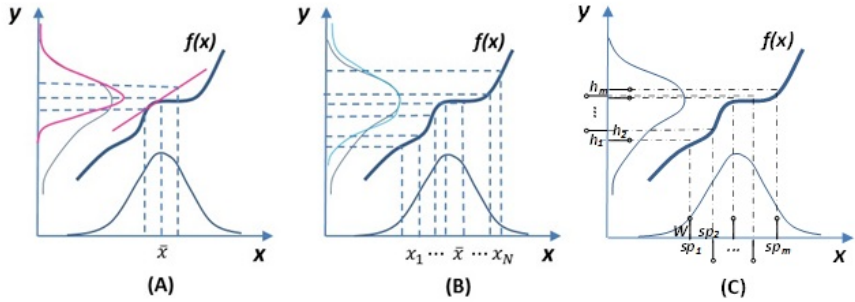

Figure 4.2: 1D comparison among Law of Uncertainty Propagation (LPU)(A), Monte Carlo (B), and Unscented Transform (UT)(C): thin line, actual *pdf*, and solid line, estimated *pdf*.

4.2.2 Basic ideas

The proposed method is based on the combined use of the Unscented Transform for the uncertainty estimation and the statistical design of experiments for the significance assessment and the impact ranking of the associated uncertainty sources. In literature, different approaches are exploited for both these problems of *uncertainty estimation* and *uncertainty source classification*.

In *uncertainty estimation* (Figs. 4.2), the classical law of uncertainty propagation (LPU), based on a first-order Taylor series approximation of the measurement model around the expected (or mean) value (Fig. 4.2A), is used. For this reason, the uncertainty estimation is tailored for linear models. In case of non-linear model, the

GUM [32] considers the Monte Carlo simulation as a valid alternative (Fig. 4.2B). Repeated random sampling are used to determine the probability distribution of the output, i.e. a brute-force concept maximizing the computational burden. A recent approach for nonlinear models is based on the Unscented Transform (Fig. 4.2C): the probability density function of the input quantity is replaced by a set of its deterministic samples (referred to as *sigma points*, *sp* in Fig. 4.2C) and corresponding suitably associated weights (W in Fig. 4.2C), either positive or negative. Sigma points and weights are determined in order to assure that the statistics of the sigma points set match those of the input quantity. This matching allows not only the expected value and standard deviation (as for GUM), but also a defined number of central moments to be propagated efficiently through a nonlinear measurement model [48]. This can achieve results, in terms of expected value and standard uncertainty of the output quantity, very close to those granted by Monte Carlo methods, but with a strongly reduced computational burden.

The *uncertainty source classification* is carried out by applying statistical tools to the UT-based uncertainty estimates obtained in a suitably limited number of numerical experiments, representative of the source domain as a whole. For the rotating coil transducers, this classification provides twofold interests:

- the effect and related significance of each uncertainty source can be assessed;
- a simple rule for setting the source uncertainty values with respect to a target uncertainty of the magnetic field can be determined.

4.2.3 Procedure

The procedure of rotating coils uncertainty analysis is illustrated in Fig. 4.3. In the following, its two main phases of *(i) Unscented Transform-based uncertainty estimation*, and *(ii) uncertainty source classification* are described with the corresponding steps.

Unscented Transform-based uncertainty estimation

1. *Measurement model definition*: According to the GUM [32], in indirect magnetic measurements, the relationship between the measured quantity (e.g., the field harmonics B_n) and a suitable set of measurands $\boldsymbol{X} = [X_1, X_2, ..., X_I]$ (e.g., the magnetic flux for each angular step, or the coil area) has to be defined. In other words, the measurement model $B_n = f(\boldsymbol{X})$ relates the quantity B_n with I measurands, modeled as random variables. The model takes into account as

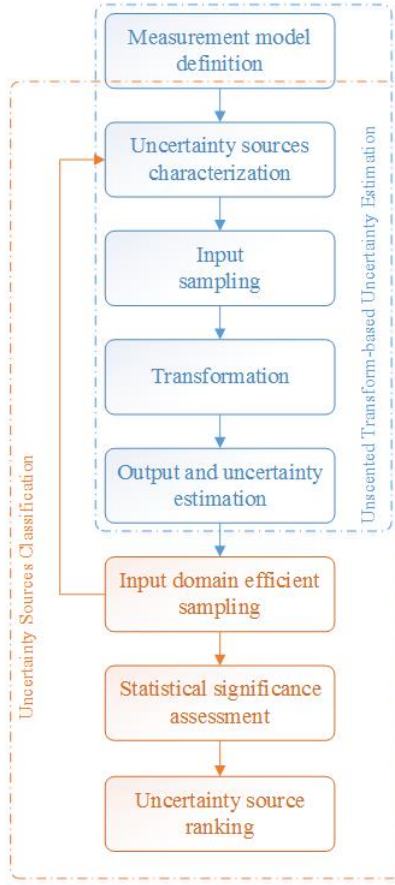

Figure 4.3: Procedure of rotating coils uncertainty analysis.

input all the known uncertainty sources affecting the measurands [32]. This task coincides with the first three steps of the main stage a) formulation of uncertainty evaluation, defined in the Supplements 1 [33] and 2 [51] of the GUM.

2. *Uncertainty source characterization*: the I input measurands $\boldsymbol{X} = [X_1, X_2, ..., X_I]$, that is, the sources of uncertainty, are characterized in terms of their *pdfs*; repeated measurements, available information, and/or user knowledge can be adopted for this purpose. For each $X_i, (i = 1, 2, ..., I)$, the expectation and a suitable collection of μ_g central moments (with $g = 1, ..., G$) have to be estimated. The higher is the number of considered central moments, and more accurate will be the estimate of the output expectation and associated uncertainty. Conceptually, this task coincides with the step 4 of the main stage a) "formulation" of uncertainty evaluation, defined in the Supplements 1 [33] and 2 [51] of the GUM.

3. *Input sampling*: The distributions of X_i are deterministically sampled so that expectation and G central moments of the sample are the same as the original population [31, 48] (Fig. 4.2C). In particular, a new, artificial distribution, composed by the sigma points *sp* and the associated arbitrary weights W, is determined for each uncertainty source.

4. *Transformation*: The measurement model is applied to the sigma points; the obtained values are usually referred to as *transformed sigma points* (h in Fig. 4.2C). In this way, a similar artificial distribution for the output B_n is determined.

5. *Output and uncertainty estimation*: The model output expectation and associated standard uncertainty are estimated analogously as in traditional average and standard deviation calculation, by combining samples and weight of the artificial distribution of B_n.

Uncertainty source classification

The second task of the method accounts for the significance assessment of the uncertainty sources.

6. *Source domain sampling*: First, the effect of variation of uncertainty values within the input sources domain has to be verified and assessed. The experi-

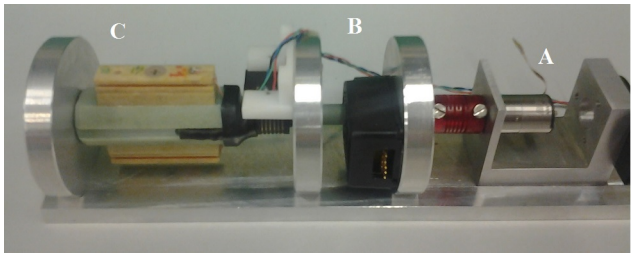

Figure 4.4: Rotating coil transducer for magnetic field mapping: (A) piezomotor, (B) encoder, and (C) sensing coils [13].

mental burden is reduced by means of a suitable strategy of experiments design. Steps from 2 to 5 have, in fact, to be repeated for each combination of the source uncertainty value to be investigated, in order to estimate the corresponding output uncertainty.

7. *Statistical significance assessment*: A statistical analysis of the output uncertainty estimates obtained in the previous step is carried out in order to check the significance of the influence of the uncertainty sources.

8. *Uncertainty source ranking*: The single contribution to the overall uncertainty budget of each significant uncertainty source is assessed. On this basis, their impact on the metrological design of the rotating coil transducer is ranked.

4.3 Case study: Rotating coil transducer for dipole field mapping

A case study on a rotating coil transducer (Fig. 4.4) for local measurements of magnetic field quality in accelerator magnets [13] is considered. The transducer was designed to measure fringe fields and to easily fit apertures of curved magnets. A rotating coil, an accurate transport for longitudinal displacements inside the magnet aperture, and components with magnetic compatibility for negligible interference of the measurand field were adopted. In the proof-of-principle demonstration of the transducer, the main field component (dipole) was measured for the experimental validation and metrological characterization.

4.3.1 Unscented transform-based uncertainty estimation

In Fig. 4.5, the transducer architecture with the main quantities, corresponding also to the main uncertainty sources, are illustrated.

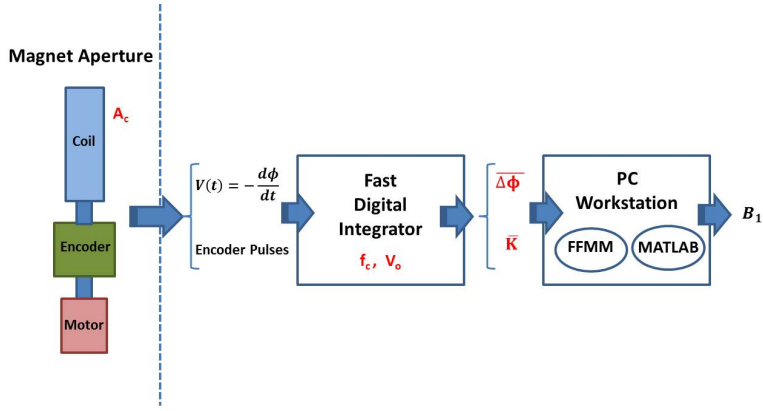

Figure 4.5: Measurement setup and uncertainty sources.

Measurement Model Definition

The definition of the measurement model is the first step of the proposed procedure (Fig. 4.3). In Tab. 4.1, the used indexes are summarized for the sake of the reader easiness.

Table 4.1: Indexes.

Index	Range	Definition	Value
n	$[1, N]$	harmonic order	$N < 15$
s	$[1, S]$	number of steps per turn	$S = 1024$
i	$[1, I]$	number of variables	$I = 5$
g	$[1, G]$	number of central moments	$G = 8$
v		dummy index	
m	$[1, M]$	number of coil turns	M=20
j	$[1, J]$	number of matrix R columns	$J = 41$
k	$[1, 4]$	W indexes	

The voltage signal $V(t)$ of the rotating coil is acquired by a digital integrator (Fast Digital Integrator, FDI [18]), and the acquisition is triggered by the angular encoder

pulses. The results are (i) the measured elementary fluxes (namely the magnetic flux for each angular step) $\Delta\phi$, and (ii) the counts K, corresponding to the instants of the encoder pulses, measured by an FDI clock of frequency f_c. On this basis, an array with the magnetic flux, defined as the cumulative sum of $\Delta\phi$, and the time instants $t(v)$ are obtained for each coil turn:

$$\phi(s) = \begin{cases} 0, & \text{if } s = 0, \\ \sum_{v=1}^{s}[\Delta\phi(v) + V_o(m)\Delta t(v)], & \text{if } s \in [1, S] \end{cases} \tag{4.5}$$

where S is the number of pulses per turn, m the number of coil turns, and

$$\Delta t(v) = t(v) - t(v-1) = \frac{K(v) - K(v-1)}{f_c} \tag{4.6}$$

the time difference between two encoder pulses. In (4.5), the magnetic flux is evaluated taking into account the drift correction, associated with the offset voltage of the integrator, $V_o(m)$. The value of the offset voltage is assessed as:

$$V_o(m) = -\frac{\sum_{s=1}^{S}\Delta\phi(s)}{P(m)} \tag{4.7}$$

where $P(m)$ is the rotation period for the $m-th$ turn:

$$P(m) = t(S \cdot m) - t\left(S \cdot (m-1) + 1\right), m \in [1, M] \tag{4.8}$$

For the sake of clarity, the measurement model is presented with reference to the first coil turn, in order to drop the dependence on the number of turns. By combining (4.6), (4.7), and (4.8), the correction term of the elementary flux $V_o\Delta t(v)$ in (4.5) can be expressed as

$$V_o\Delta t(v) = -\frac{f_{c1}\sum_{s=1}^{S}\Delta\phi(s)}{K(S) - K(1)} \cdot \frac{K(v) - K(v-1)}{f_{c2}} \tag{4.9}$$

where f_{c1} and f_{c2} are two different states of the digital integrator clock.

The harmonic components of the discrete Fourier transform of the flux (4.5) are:

$$\Phi_n = \frac{2}{S}\sum_{s=1}^{S}\left[\phi(s)\exp\left(-\frac{j2\pi n(s-1)}{S}\right)\right] \tag{4.10}$$

and considering the coil sensitivity for a perfect tangential coil [15]

$$H_n = \frac{2jQL}{n}R^n\sin(\frac{n\Delta}{2}) \tag{4.11}$$

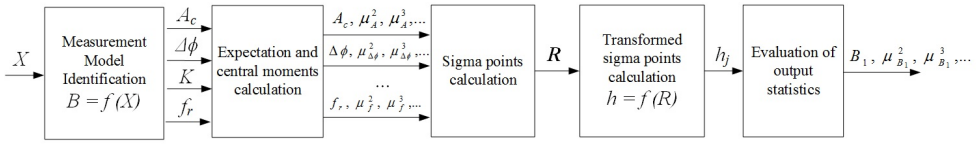

Figure 4.6: UT-based uncertainty estimation [48] of rotating coil transducers for magnetic field mapping.

where L is the coil length, Q is the number of windings, R is the radius of the winding centers, and Δ is the opening angle (Fig. 4.1). The field harmonics can be obtained as

$$B_n = \frac{r_0^{n-1}\,\Phi_n}{H_n} \tag{4.12}$$

The field harmonics ($n > 1$, i.e. quadrupole, sextupole higher order, etc.) depend on reference radius r_0, while the dipole field measurements are independent of r_0. In fact, the formula (4.12) can be simplified as the ratio between the first flux component,Φ_1, and the coil area, $H_1 = A_c$:

$$B_1 = \frac{\Phi_1}{A_c} \tag{4.13}$$

Combining all the preceding equations, the expression for the dipole field harmonic can be written as:

$$B_1 = |\frac{2}{A_c S}\sum_{s=1}^{S}\sum_{v=1}^{s}[\Delta\phi(v)+ \\ - \frac{[\sum_{s=1}^{S}\Delta\phi(s)]\cdot[K(v)-K(v-1)]f_r}{K(S)-K(1)}]\cdot\exp[-\frac{j2\pi(s-1)}{S}]| \tag{4.14}$$

where the ratio f_r=f_{c1}/f_{c2} has nominal value equal to 1.

According to the simplified model (4.14), the uncertainty source contributions related to the reference radius and to further sources (e.g. vibrations and manufacturing tolerances) are not considered.

Furthermore, the model (4.14) is nonlinear, and thus, the applicability of the GUM linearization is to be verified in the specific practical case.

Uncertainty Source Characterization

According to the flow chart of Fig. 4.6, the main uncertainty sources have to be modeled for the rotating coil transducer. From (4.14), the main sources of uncertainties are A_c, $\Delta\phi_s$, K, and f_r.

The expected value of A_c is assigned by calibration. As a consequence, the corresponding input quantity is modeled as a uniform random variable: $A_c \sim \mathcal{U}(a_c, \Delta A)$. $\Delta\phi$ is modeled as a Gaussian variable, $\Delta\phi \sim \mathcal{N}(0, \sigma(\Delta\phi))$, with a standard deviation $\sigma(\Delta\phi)$ related mainly to the integrator specifications.

The uncertainty on the counts is related to the resolution of the digital counter, and the corresponding quantity is modeled as a uniform variable: $K \sim \mathcal{U}(k, \Delta K)$.The time array is determined as the difference between two shifted vectors $(K(v) - K(v-1))$. Correspondingly, two different variables, $K_1 = K(v-1)$ and $K_2 = K(v)$, are considered in the uncertainty model. The uncertainty on f_r is determined from the short-term stability of the digital integrator clock frequency, owing to the limited measurement interval. As for the coil area, f_r is modeled as a uniform random variable according to $f_r \sim \mathcal{U}(1, \Delta f_c)$.

All the uncertainty sources characterized are collected in $\boldsymbol{X} = [A_c, \Delta\phi, K_1, K_2, f_r]$; The input variables are mutually independent, therefore they can be considered as uncorrelated. Their expectations and the suitable collection of central moments can be evaluated easily stemming from the assumed *pdf*. Furthermore, the considered *pdfs* are symmetric, thus even the central moments up to the 8^{th}, i.e. $G = 8$, have to be calculated [48].

Input Sampling

This step (Fig. 4.3) aims at sampling deterministically the input variables $X_i \in \boldsymbol{X}, (i = 1, 2, ..., 5)$ in order to construct a new artificial distribution (sigma points), characterized by the same mean and central moments of the i^{th} uncertainty source. The sigma points are input quantities sampled from the original *pdf* by means of weights W, determined in a way that the sigma points maintain the same statistics of $\boldsymbol{X}$, by solving the nonlinear equation system:

$$\begin{bmatrix} 0 \\ \boldsymbol{C}^2 \\ \vdots \\ \boldsymbol{C}^8 \\ 1 - W_0 \end{bmatrix} = \begin{bmatrix} \boldsymbol{D}_1 & \boldsymbol{D}_2 & \dots & \boldsymbol{D}_8 \\ \boldsymbol{D}_1^2 & \boldsymbol{D}_2^2 & \ddots & \boldsymbol{D}_8^2 \\ \vdots & \vdots & \ddots & \vdots \\ \boldsymbol{D}_1^8 & \boldsymbol{D}_2^8 & \dots & \boldsymbol{D}_8^8 \\ 5 & 5 & \dots & 5 \end{bmatrix} \begin{bmatrix} W_1 \\ W_2 \\ \vdots \\ W_8 \end{bmatrix} \tag{5.15}$$

where $\boldsymbol{C}^g = diag\left(\mu^g_{A_c}, \mu^g_{f_r}, \mu^g_{K_1}, \mu^g_{K_2}, \mu^g_{\Delta\Phi}\right)$ are 5x5 diagonal matrices , whose generic entry μ^g_i is the g^{th} central moment of the $i-th$ input random variable (where $g =$

$1, ..., 8$). The last row of system (5.15) is

$$1 = W_0 + 5(W_1 + W_2 + ... + W_8) \tag{5.16}$$

The sigma points are collected and arranged in a matrix $\boldsymbol{R}$ (the *sigma set*), consisting of 5 rows (equal to the number I of entries of the array $\mathbf{X}$) and $J = G \cdot I + 1 = 41$ columns:

$$\boldsymbol{R} = [\boldsymbol{P} + \boldsymbol{D}_1, \boldsymbol{P} + \boldsymbol{D}_2, \ldots, \boldsymbol{P} + \boldsymbol{D}_G, \boldsymbol{x}^T] \tag{5.17}$$

where:

- $\boldsymbol{P}$ is an 5-dimensional square matrix given by 5-times repetition of the array $\boldsymbol{x}^T$, containing the expectations (or means) of the variables X_i, this is

$$\boldsymbol{P} = \left[\boldsymbol{x}^T, \ldots, \boldsymbol{x}^T\right] = \begin{bmatrix} a_c & \ldots & a_c \\ 1 & \ldots & 1 \\ k_1 & \ldots & k_1 \\ k_2 & \ldots & k_2 \\ \Delta\phi & \ldots & \Delta\phi \end{bmatrix} \tag{5.18}$$

- $\boldsymbol{D}_g$, $g = 1, ..., 8$ are 5 x 5 diagonal matrices

$$\boldsymbol{D}_g = \begin{bmatrix} d_{gA_c} & 0 & \ldots & \ldots & 0 \\ 0 & d_{gf_r} & 0 & \ddots & \vdots \\ \vdots & 0 & d_{gK_1} & 0 & \vdots \\ \vdots & \ddots & 0 & d_{gK_2} & 0 \\ 0 & \ldots & \ldots & 0 & d_{g\Delta\Phi} \end{bmatrix} \tag{5.19}$$

In particular, the first and the last line of the equations system (5.15) assure an unbiased determination of the sigma set. According to the UT approach, the best estimate of each variable, defined as [48], is

$$x_i = \sum_{j=1}^{5} W_1 R_{i,j} + \sum_{j=6}^{10} W_2 R_{i,j} + ... + \sum_{j=36}^{40} W_8 R_{i,j} + W_0 R_{i,41} \tag{5.20}$$

Similar considerations hold for the other central moments.

For symmetric *pdfs* of X_i, the solution of the system (5.15) can be optimized by assuming:

$$\boldsymbol{S}_{2k} = -\boldsymbol{S}_{2k-1}, \quad W_{2k} = -W_{2k-1}, \quad k = 1, \ldots, 4. \tag{5.21}$$

In this way, only 4 equations and unknown matrices $\boldsymbol{S}_i$ are necessary so that:

- the even central moments, up to the 8^{th} order, of the resulting sigma points are equal to the corresponding ones of input variables,
- and the odd central moments are zero because the input variables are characterized by symmetric *pdfs*.

By selecting the values of W_g (as from (5.16)), the equation system (5.15) can be solved in explicit form for central moments up to the 8^{th} order [48].

Transformation

The measurement model (4.14) is now applied to each sigma point to determine the transformed sigma-points:

$$h_j = f(\boldsymbol{R}|_{\boldsymbol{j}}), \qquad j = 1, ..., J = G \cdot I + 1 \tag{5.22}$$

where $\boldsymbol{R}|_{\boldsymbol{j}}$ represents the j^{th} column of the matrix $\boldsymbol{R}$ of the sigma set.

Output quantity estimation

The expected value estimate of B_1 is computed by processing the h_j, as in (5.20),m for $R_{i,j} = h_j$:

$$\hat{B_1} = \sum_{j=1}^{5} W_1 h_j + \sum_{j=6}^{10} W_2 h_j + ... + \sum_{j=36}^{40} W_8 h_j + W_0 h_{41} \tag{5.23}$$

The associated standard uncertainty can be obtained from the estimated variance according to

$$u\,(B_1) = (\sum_{j=1}^{5} W_1 (h_j - \hat{B_1})^2 + \sum_{j=6}^{10} W_2 (h_j - \hat{B_1})^2 + ... + \sum_{j=36}^{40} W_8 (h_j - \hat{B_1})^2 + W_0 (h_{41} - \hat{B_1})^2)^{\frac{1}{2}} \tag{5.24}$$

4.3.2 Uncertainty source classification

The separated effect of each significant uncertainty source on the transducer performance is assessed by simulation. The simulation burden is reduced by statistical design of experiments in order to control the related significance loss simultaneously [52].

Field uncertainty estimation in the input sources domain

To this aim, the variation range of the uncertainty sources is established according to both the typical variation interval and the practice knowledge and experience. The range is discretized on a limited number of levels. In particular, all the uncertainty values of the sources has been discretized on three levels, but those of the counts K, on two.

The total number of tests, equal to $2 \cdot 3^3$, is then limited my means of a standard Resolution III plan L18 [53]. It allows the subspace generated by one two-levels and up to six three-levels statistically-independent parameters to be explored efficiently. From an operating point of view, the L18 plan is organized as a matrix: each uncertainty source is assigned to a column, by suitably selecting its levels so that each row determines a specific configuration of uncertainty sources to be adopted for assessing $u(B_1)$ by Eq. (5.24).

The effect of the uncertainty sources on $u(B_1)$ is determined by analysis of mean (ANOM), carried out as detailed in [54].

Significance assessment of the uncertainty sources

The significance of the uncertainty sources effect on $u(B_1)$ is determined by analysis of variance (ANOVA). In particular, the ratio F between the source and error variances is assessed by checking for its significance by a Fisher test [55]. If the result is positive, the associated uncertainty source has a significant effect on $u(B_1)$.

Chapter 5

Transducer and bench implementation

The Chapter presents the implementation of the full system components: the transducer and the train-like motion system. The rotating coil transducer was implemented on different prototyping phases. The twofold prototypes reported here deal with a measuring shaft with absolute wiring coils, and PCB coils. The train-like motion system is composed of a rail and a trolley. The motion is actuated by a rotary piezomotor, driving a belt plastic rack and pinion system. The longitudinal position is measured by a linear encoder, magnetically compatible, with flexible codestrip.

5.1 Transducer

Prototype A piezoelectric motor, ER-15 of Nanomotion [56] was selected for driving the shaft (Fig. 5.1 A). The main features of ER-15 are: diameter of 15 mm, length of 22.5 mm, weight of 12 g, variable speed of rotation from 40 to 180 rpm, and a torque from 6 to 4 Nmm. Like most similar devices this motor includes some ferromagnetic components, such as the ball bearings and the shaft, the effects of which have to be checked experimentally. The optical encoder HEDM 5505-J13 of Avago Technologies [57] (Fig. 5.1 B) has specifications matching the design goals: non-magnetic material (plastic code wheel), compact dimension ($41 \times 30 \times 18$ mm), and an adequate resolution (1024 cycles per revolution).

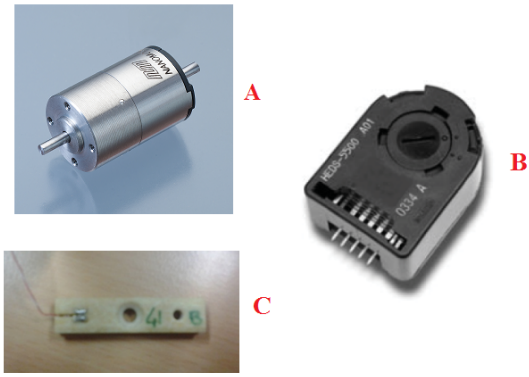

Figure 5.1: Main components of the transducer prototype: A) piezomotor ER-15 by Nanomotion, B) encoder HEDM 5505-J13 by Avago Technologies, and C) sensing coils (40×10 mm, area: 0.12367 m^2, resistance: 420 Ω).

The coil shaft is made in fiberglass to ensure suitable rigidity and magnetic compatibility during the rotation. Two coils (Fig. 5.1 C) of dimensions 40×10 mm, with a total sensing surface area of 0.12367 m^2, 485 turns, and a resistance of 420 Ω each are mounted on the shaft (Fig. 5.2) in tangential configuration (i.e. intercepting the radial magnetic flux density) without compensation coil. One coil measures the field, while the other is kept as a spare and, at the same time, balances mechanically the shaft. The length of the coil is determined by the required longitudinal resolution of the measurement, while the width is constrained by the magnet gap and shaft size. The number of turns determines the total coil area, which must be chosen so as to obtain coil signals of the order of a few Volt in the given magnetic field at the given rotation speed (typically of the order of 1 rps).

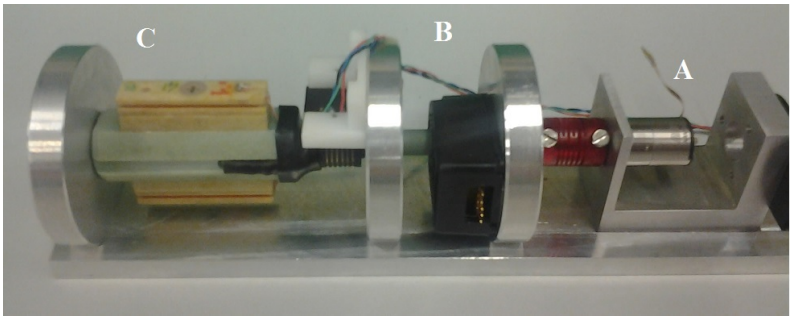

Figure 5.2: Prototype of the rotating coil transducer: A) piezomotor, B) encoder, and C) sensing coils.

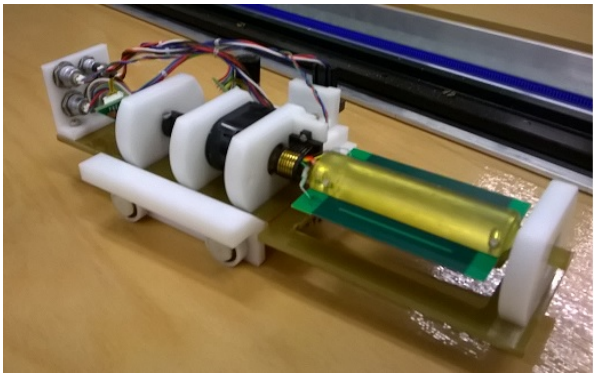

Figure 5.3: Final transducer mounting the PCB coils.

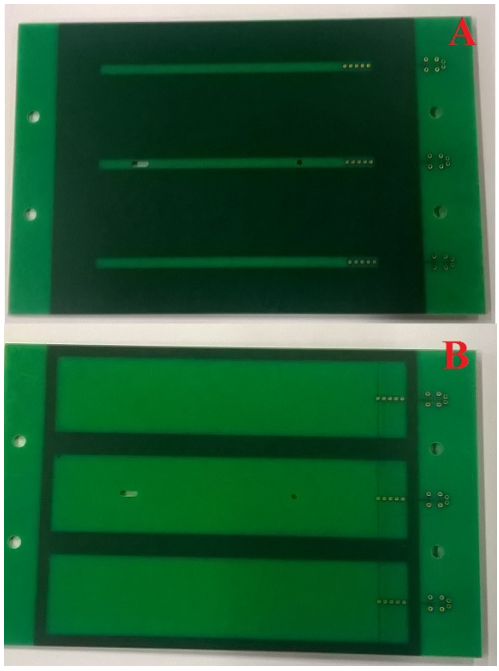

Figure 5.4: Printed circuit board coils: 10 pcb layers with (A) 41 and (B) 10 tracks per layer, and coil surfaces of 0.25803 and 0.10803 m^2.

Final transducer The final transducer shown in Fig. 5.3 mounts the PCB coils (Fig. 5.4), and a coil shaft made in plastics (Accura® 48HTR [58]). The PCB coils, as reported in Chapter 4, are composed of 10 layers with 41 and 10 tracks per layer (coil surfaces of 0.25803 and 0.10803 m^2). Considering the particular installation, the support shaft for the coils was realized in plastics by a 3D printer (Polymer lab at CERN).

5.2 Train-like motion system

The general requirements and architecture highlight some technical aspects to be taken into account: magnetic compatibility, mechanical stability, and high precision of positioning system. Considering the measurement features of the proposed system, the transducers and motion/positioning parts should be magnetically compatible and, in particular, the moving components should be free of metals, avoiding perturbation of field by eddy currents insurgences. In fact, the transducer should be able to be

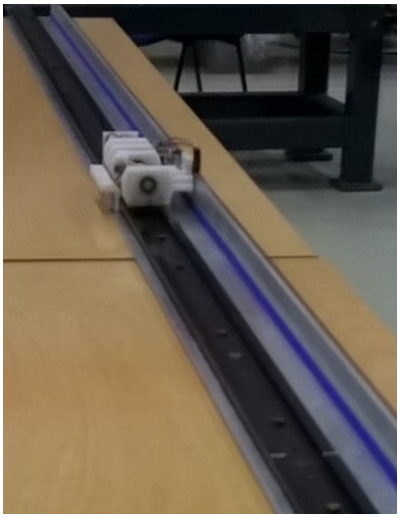

Figure 5.5: Train-like motion system.

placed inside the magnet aperture, completely immersed in the magnetic field, as presented in [13]. The mechanical stability is a pre-requirement of every measurement system, and this is reached by an high manufacturing precision. The high precision positioning system depends on the linear actuator and the relative component, such as the linear encoder.

The magnetic compatibility is guaranteed by choosing the suitable components, such as rotary piezomotor, optical encoder and non-metallic materials for the support [13]. The mechanical stability is given by a precision manufacturing of the components. Apart the choice of metal free components, the high precision of positioning system can be realized by a piezomotor-actuator and an optical encoder, used for the transducer. Another important component for the positioning is represented by the general support. In particular, the rail of the trolley should have the right trade off between high mechanical tolerance (running clearance less than 100 μm) for guaranteeing the precision and low mechanical resistance for allowing the sliding of the trolley.

Prototype The prototype of the magnetic measurement system is composed of two parts: i) the rotating coil transducer, and ii) the train-like system (Figs. 5.5 and 5.6). The transducer [13] was mounted on a trolley in white plastics, with three wheels (ceramic ball bearing), and a base plate made in yellow composite fiberglass.

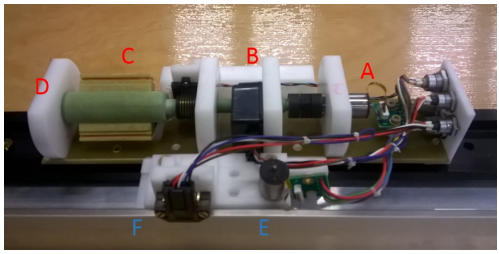

Figure 5.6: Rotating coil transducer: (A)piezomotor for rotating coil, (B) rotary optical encoder, (C) coils, (D) plastic support and trolley, (E) piezomotor for longitudinal motion, and (F) linear optical encoder.

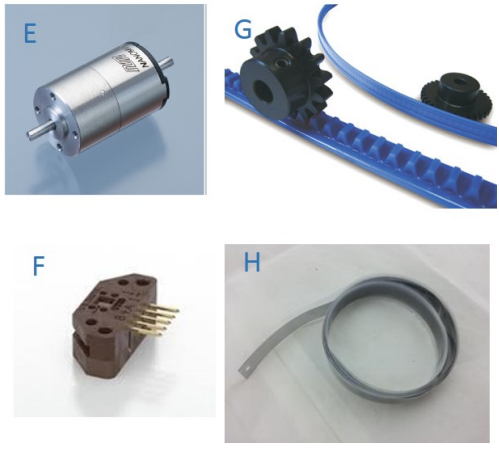

Figure 5.7: Motion and positioning system components: piezomotor, linear, plastic rack and pinion, and flexible codestrip.

The longitudinal motion of the trolley is transmitted by plastic rack and pinion [59] (Fig. 5.7G) actuated by means of a rotary piezomotor, ER-15 Nanomotion [56] (Figs. 5.6E and 5.7E). The position measurement of the trolley is effetuated by an optical encoder, HEDS-9200 360 [60] (Fig. 5.7F), with a pitch per count of 70 μm, using an high precision flexible codestrip [61] (Fig. 5.7H).

5.2.1 Interface Device

The interface device was implemented for controlling the two piezomotors (linear and rotating motion). The device is composed of two PCB cards, and each card mounts the motor controller (side A, Fig. 5.8), the powering card of the motor (side B, Fig.

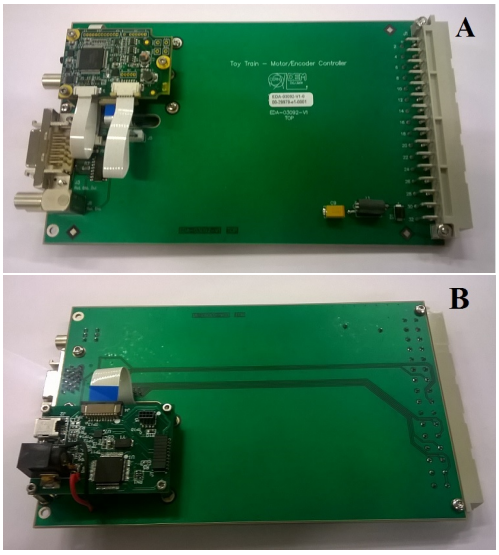

Figure 5.8: Interface device card (by David Giloteaux - TE-MSC-MM section, CERN): (A) side of piezomotor controller, and (B) side with the powering card of the motor.

5.8) and the conditioning circuit card for encoder signals.

Chapter 6

Metrological Characterization: Transducer

This Chapter deals with the metrological characterization of the rotating coil transducer by describing the preliminary phase of feasibility tests, the uncertainty analysis, and the metrological characterization. The feasibility tests concerned the magnetic compatibility and the speed variations of the piezomotor, and the electrical interference of the full transducer. The results of the uncertainty model presented in chapter 4 are shown, by considering the main uncertainty sources and their classification. Finally, the repeatability, linearity, and resolution results are reported for the absolute field measurements.

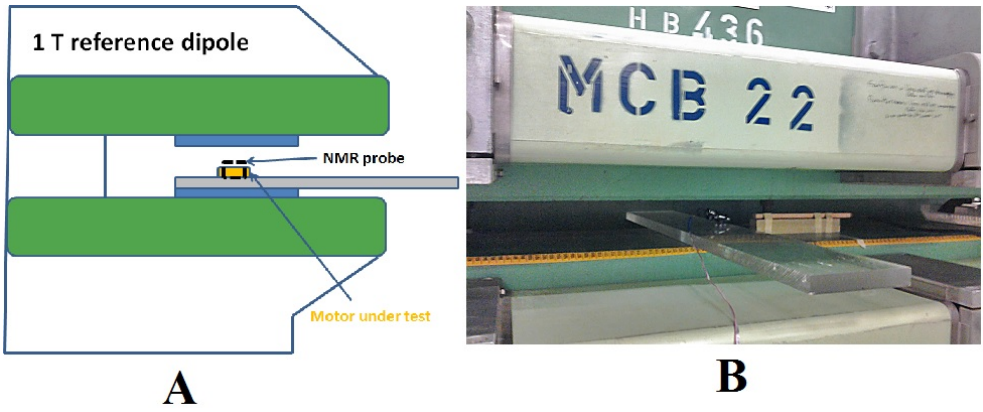

Figure 6.1: Magnetic compatibility test set up: A) trasversal section, and B) Plexiglas support of the motor under test with the NMR probe inside the 1T reference dipole (MCB22).

6.1 Feasibility Tests

6.1.1 Magnetic Compatibility

The aim of the test is to verify the magnetic field variation due to the presence of the transducer inside the magnet with respect to a threshold (typically of 100 ppm). The only component with ferromagnetic parts is the piezomotor ER-15. The test procedure is to put the piezomotor into the aperture of a reference dipole magnet with a static magnetic field, and to measure the field before and after the motor insertion.
The measurement setup is composed by a NMR Teslameter (Metrolab PT2025 [1]), the 1-T dipole reference magnet of the Magnetic Measurement Section at CERN, and the piezomotor ER-15 under test (Fig.6.1).

Two different configurations of the piezomotor with respect to the NMR Teslametr probe were investigated (Fig. 6.2): (A) aligned along the axis and (B) in a lateral position. The test was carried out at increasing magnetic field levels ([0.4, 0.5, 0.8, 1.0] T) with the motor both switched off and on. The test at 1.0 T in alignment configuration (Fig. 6.2A) turned out to be the worst case. The measured variations in magnetic field, with motor off and on, at different distances are reported in Tab.6.1. The trend and the threshold are highlighted in Fig. 6.3. The minimum distance in order to have an influence on the field lower than the threshold is 4 cm. This result was taken into account for positioning the coil on the shaft in the prototype.

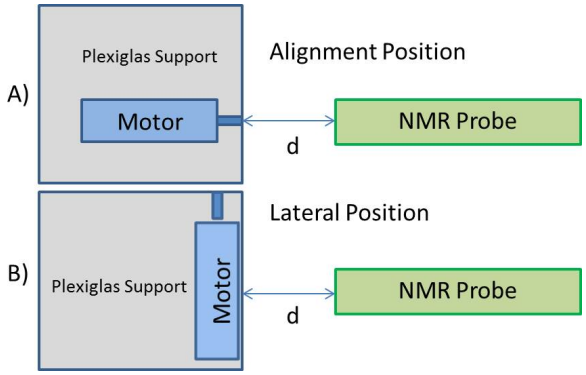

Figure 6.2: Magnetic compatibility test configurations: motor and NMR probe in position (A) aligned along the axis and (B) lateral (d: distance).

Table 6.1: Magnetic compatibility test results: magnetic field differences between the reference NMR measurements without and with motor (off and on) at 0.8 T at varying distance.

distance (cm)	$\Delta B/B$ (motor off) (ppm)	$\Delta B/B$(motor on) (ppm)
2	537	535
3	219	219
4	95	94
5	36	36
6	17	17
7	7	7
8	4	4
9	2	2

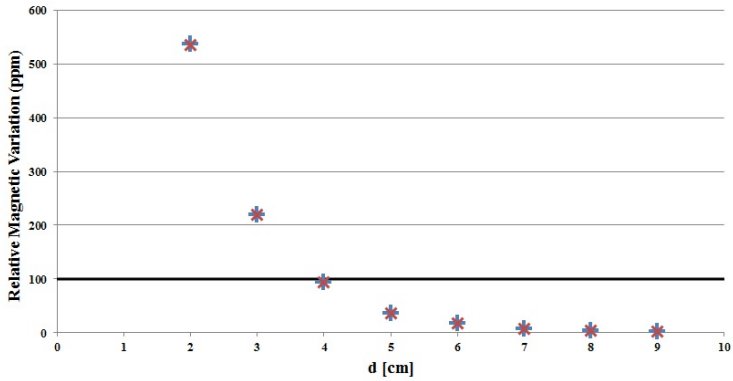

Figure 6.3: Magnetic compatibility test: relative variations of magnetic field without and with motor (off and on) in worst-case alignment position.

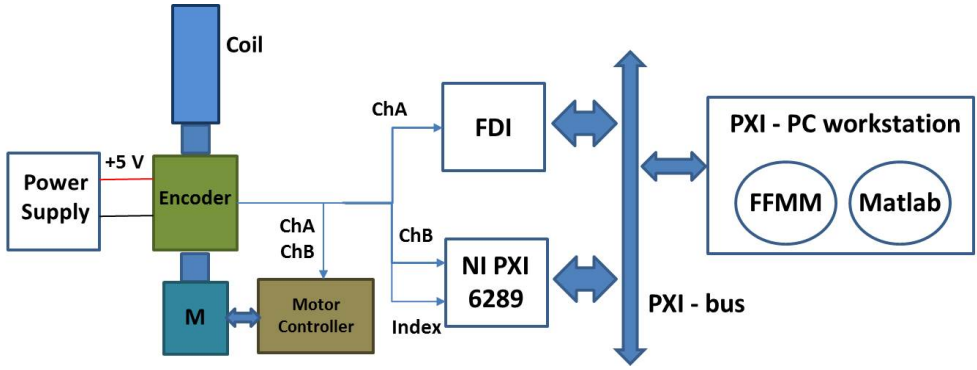

Figure 6.4: Speed variation test: measurement setup.

6.1.2 Speed variations

The aim of this test is to check the stability of the rotation speed stability of the piezomotor and to compare it to reference systems at CERN [27, 62]. The measurement setup (Fig. 6.4) is based on a data acquisition board (NI PXI 6289 [63]), a power supply for the encoder, and a Fast Digital Integrator (FDI) with an encoder interface used to acquire the encoder pulses [18]. The measurement is carried out by means of the Flexible Framework for Magnetic Measurements (FFMM) [19], a C++ program running on a PXI PC workstation. Result analysis was done in Matlab.

Three different case studies were considered to assess the variation of the angular speed ω: (i) *stand-alone configuration*, that is, only motor and encoder; (ii) *complete*

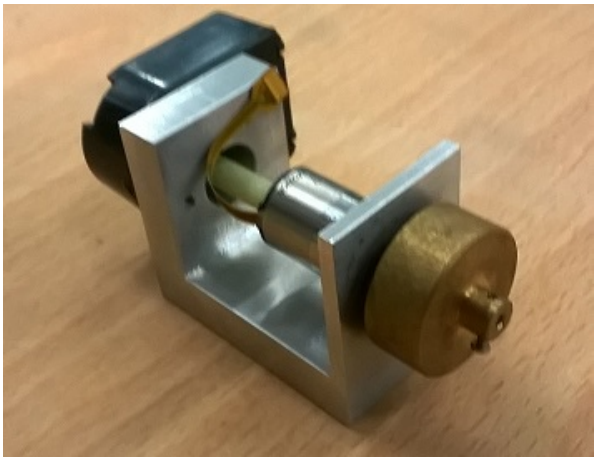

Figure 6.5: Setup (encoder, motor and flywheel) for assessing the intrinsic rotation speed features of the piezomotor ER-15 of Nanomotion [56].

configuration in a field-free region, in order to determine the optimal controller settings; and (iii) *complete configuration in a reference dipole*, to check the transducer rotation in presence of different levels of magnetic field.

Case study 1: stand-alone configuration

In this case study, the intrinsic rotation features of the piezomotor ER-15 by Nanomotion [56] (Fig. 5.2A) are tested in the minimal setup of Fig. 6.5. A flywheel of about 50 g was used to increase the inertia of motor, and thus, to emulate the mechanical load of the coil. The quality of rotation in term of acceptable speed fluctuations, i.e. RMS and peak-to-peak percent variations of the angular velocity ω, has been measured.

Preliminarily, the motor operation was tuned by setting the drive and feedback loop gain of its controller Nanomotion XCD [56]. The objective is to optimize the velocity loop with respect to the applied load. The speed variation depends mainly on these parameters and on the weight of the rotating shaft. The results for the speed variation are reported in Tab. 6.2, expressed as reference and measured speed, as well as root mean square (RMS) and peak-to-peak of their relative difference $(\Delta\omega/\omega)_{pp}$. The results show that speed variations decrease as the speed consistently with the behavior of similar systems based on step motors.

Table 6.2: Speed variation results: stand-alone configuration.

Reference (rps)	Average ($\bar{\omega}$) (rps)	RMS($\Delta\omega/\bar{\omega}$) (%)	$(\Delta\omega/\bar{\omega})_{pp}$ (%)
1	1.036	3.28	19.92
2	2.071	2.08	12.30
3	3.108	2.00	11.38

Table 6.3: Speed variation results: complete configuration in a field-free region.

Reference (rps)	Average ($\bar{\omega}$) (rps)	RMS($\Delta\omega/\bar{\omega}$) (%)	$(\Delta\omega/\bar{\omega})_{pp}$ (%)
1	1.036	3.04	21.60
2	2.072	1.96	14.48
3	3.108	1.68	12.76

Case study 2: Complete configuration in a field-free region

The second speed variation test was made with the complete transducer (Fig. 5.2). The results are given in Tab. 6.3. The measured RMS and peak-to-peak speed variations are compatible with the previous ones (Tab. 6.2), independently of the motor load. In Tab. 6.4, the rotation performance of the proposed transducer and the motor unit of main current CERN benches (LINAC4 [62] and MRU [27]) is compared. The amplitude of RMS speed variations is about three times higher than that the best similar systems in operation at CERN. This is still acceptable if the measurement time is kept sufficiently short so that any input voltage offset can be considered constant throughout a coil rotation, since in this case the resulting drift can be corrected exactly by post-processing [64].

Table 6.4: Speed variation results: performance comparison with other CERN benches, LINAC4 [62] and MRU-based [27] systems.

Bench	Reference (rps)	Average ($\bar{\omega}$) (rps)	RMS($\Delta\omega/\bar{\omega}$) (%)	$(\Delta\omega/\bar{\omega})_{pp}$ (%)
Transducer	1	1.036	3.04	21.60
MRU	1	0.989	0.74	3.84
LINAC4	0.5	0.499	1.82	10.36

Table 6.5: Speed variation results: complete configuration in a reference dipole.

Field (T)	Reference (rps)	Average ($\bar{\omega}$) (rps)	RMS($\Delta\omega/\bar{\omega}$) (%)	$(\Delta\omega/\bar{\omega})_{pp}$ (%)
0.0	2	2.072	1.96	14.48
0.2	2	2.073	2.00	14.22
0.4	2	2.073	1.88	14.36
0.6	2	2.073	1.98	14.48
0.8	2	2.073	2.04	15.16
1.0	2	2.073	1.94	14.30

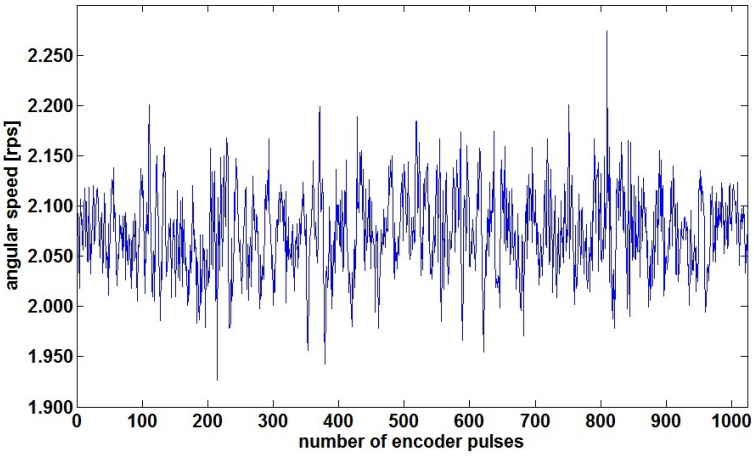

Figure 6.6: Angular speed signal for magnetic field of 1.0 T and nominal speed of 2 rps.

Case study 3: Complete configuration in a reference dipole

In this test, the speed variation is measured at different angular speeds ω ([1.000, 2.000, 3.000] rps), at different dipole magnetic fields B ([0.0, 0.2, 0.4, 0.6, 0.8, 1.0] T), in the transducer complete configuration. In Fig. 6.6,a typical angular speed measurement is shown as a function of azimuthal angle. As an example, Tab. 6.5 and Fig. 6.7 show the rotation speed results for 2.000 rps and different magnetic fields. Results of all the tests show the independence of speed variations upon the magnetic field.

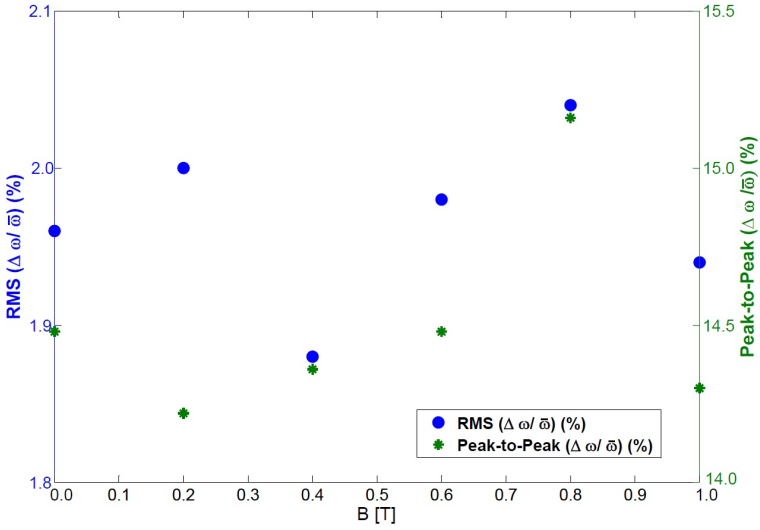

Figure 6.7: Percent RMS and peak-to-peak variations of speed at different magnetic field.

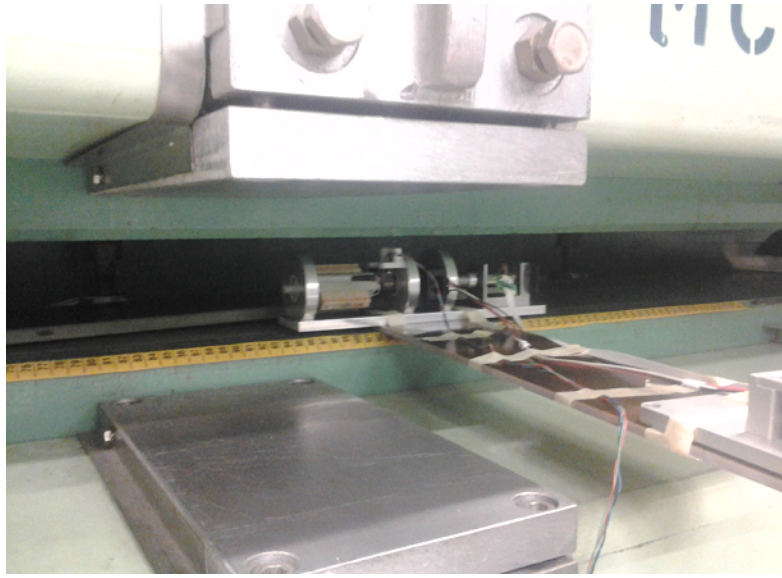

Figure 6.8: Field measurement quality test: rotating coil transducer inside the 1 T reference dipole (MCB22).

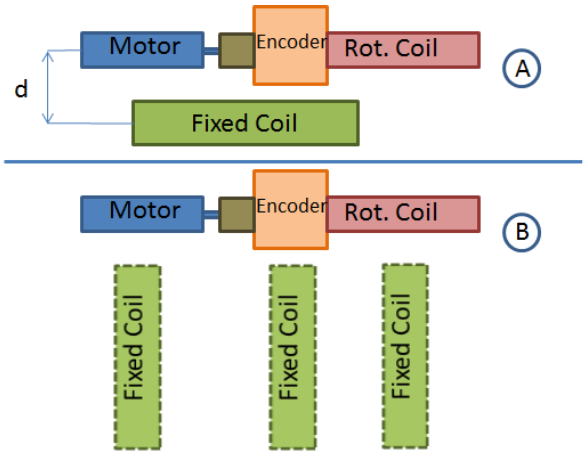

Figure 6.9: Configurations of electrical interference test: with fixed coil A) parallel and B) perpendicular to the prototype.

6.1.3 Electrical Interference Tests

The measurement setup (shown in Fig. 6.9) is based on the prototype (rotating motor, encoder, and rotating coil shaft), an independent fixed coil (dim. 20×10 mm, $S = 0.31839$ m^2) and a data acquisition card (NI PXI 6289 [63]). The test procedure is to acquire the output voltage of the fixed coil over the full speed range of the motor, for different relative positions and distances of the fixed coil. The aim is to measure the peak amplitude of the induced noise of the prototype as a whole and to understand its influence on the measured voltage signal of the rotating coil. Different configurations between prototype and fixed coil were tested to analyze the interference. The results presented here are referred to two interesting cases: i) fixed coil planar and parallel to the prototype, by acquiring the voltage signal for different rotation speeds, and ii) planar and perpendicular to the prototype, by acquiring the voltage signal at different positions (with respect to the motor, encoder, and rotating coil).

For both configurations, three different states were evaluated: 1) motor off, 2) motor and encoder on, and 3) encoder off. In this way, the tests were able to distinguish the electrical interference of each component. Four acquisitions of 2 s and 400.000 samples each were considered for each state (sampling frequency of 200.000 S/s, improving the resolution of the data acquisition card, $\delta R = \pm 0.01$ μV). The standard deviation and mean of the fixed coil voltage signal is calculated to measure

Table 6.6: Standard deviation of fixed coil voltage for different distance (configuration A Fig. 6.9) in three states: motor off (Off), motor and encoder on (On), and encoder off.

d [cm]	Off [μV]	On [μV]	Enc.Off [μV]
4	$21,3$	$984,3$	$960,6$
5	$19,0$	$636,5$	$639,3$
6	$18,6$	$501,7$	$504,4$

Table 6.7: Standard deviation of fixed coil voltage for different perpendicular position in three states: motor off (Off), motor and encoder on (On), and encoder off (configuration B Fig.6.9).

Pos.	Off [μV]	On [μV]	Enc.Off [μV]
M	$23,5$	$650,1$	$649,0$
E	$29,0$	$449,1$	$452,1$
S	$34,6$	$295,5$	$298,5$

the electrical noise contribution, by avoiding offset and DC voltages. In case of the first configuration (Fig. 6.9 A) the results in Tab. 6.6 show decreasing noise with the distance (Fig. 6.10). In the second configuration (Fig. 6.9 B), the results of Tab. 6.7 and Fig. 6.11 show a greater electrical interference close to the motor.

6.2 Uncertainty analysis results

The uncertainty analysis approach, presented in Chapter 4, was validated on the rotating coil transducer for field mapping of [13]. In this Section, the results of uncertainty computation are reported, by comparing them to the experimental characterization reported in [13].

6.2.1 Uncertainty estimation

In Tab. 6.8, the adopted values of standard deviation σ and systematic error Δ for normally and uniformly distributed input quantities, are summarized. For the counts K, the uncertainty arising from the resolution was taken into account, while the other values were inferred from the device specifications [65].

Then, all the steps in Fig. 4.6 were carried out for the measurement model (4.14). In Tab. 6.9, examples of results for different values of magnetic field, $B = [0.2, 0.4, 0.6, 0.8, 1.0]\ T$, and rotating speed of transducer equal to 120 rpm, are reported. In the same table, the corresponding results of the repeatability experiments,

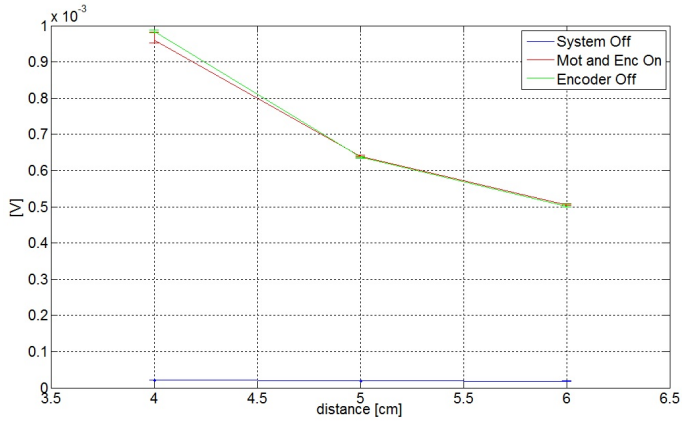

Figure 6.10: Standard deviation and its spread over 4 consecutive measurements of fixed coil voltage signal for different positions.

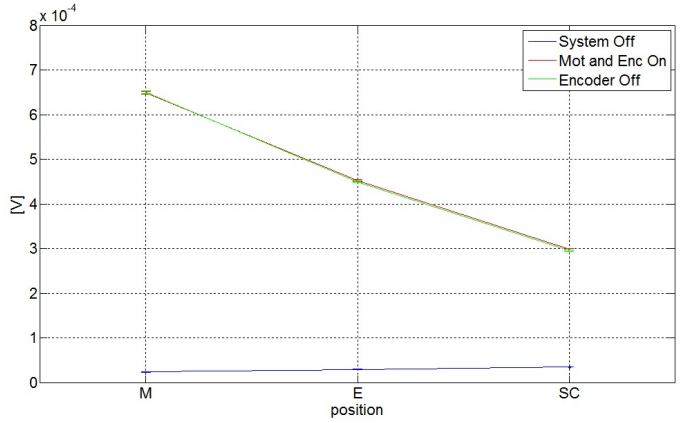

Figure 6.11: Standard deviation and its spread over 4 consecutive measurements of fixed coil voltage signal for different perpendicular positions (see Fig. 6.9B).

Table 6.8: Uncertainty sources characteristics.

Variates	Model	x	σ, Δ	unit
$\Delta\Phi$	$\mathcal{N}$	0	2.05×10^{-5}	Vs
A_c	$\mathcal{U}$	0.1237	4.95×10^{-5}	m^2
f_r	$\mathcal{U}$	1	5×10^{-10}	–
K_1	$\mathcal{U}$	0	1	–
K_2	$\mathcal{U}$	0	1	–

carried out on the reference dipole MCB22, by the setup scheme of Fig. 4.5, according to the protocol reported in [13], are reported.

Table 6.9: Expectation and associated standard uncertainties of main magnetic dipole field estimated through both the UT-based approach and experiments.

Exp. Value	$\hat{B}_1$	$u(B_1)$	$\hat{B}_1$ [13]	$\sigma_{B_1}/\bar{B}_1$ [13]
T	T	μT	T	ppm
0.2	0.200460	$\pm$54	0.200438	110
0.4	0.400475	$\pm$95	0.398831	72
0.6	0.600774	$\pm$139	0.598293	104
0.8	0.800638	$\pm$185	0.797384	86
1.0	1.001121	$\pm$230	0.996239	72

The results are compatible, thus validating the proposed approach of uncertainty estimation(Fig.6.12).

6.2.2 Uncertainty source classification

The uncertainty sources were classified by iterating the UT-based uncertainty estimation. In particular, the discretized levels of the uncertainty sources in Tab. 6.10 were selected.

The corresponding L18 matrix is shown in Tab. 6.11, along with the associated estimates of field uncertainty in tests at a nominal magnetic field of 1 T.

The ANOM was carried out for the obtained estimates. The results, in terms of marginal means (i.e., the average in L18 row tests with the same value of source uncertainty), are shown in Tab. 6.12, and in Fig. 6.13 with a 1-sigma interval of error

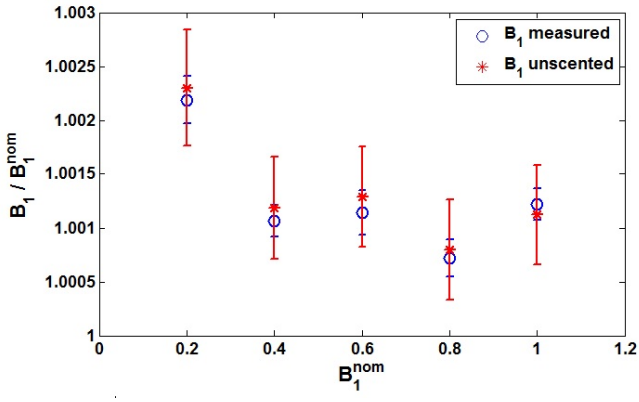

Figure 6.12: Compatibility check graph between the field measurements estimated by unscented approach and the measured ones.

standard deviation. The most influencing uncertainty source turns out to be $u(A_c)$; conversely, any apparent variation is associated with levels of both $u(K)$ and $u(f_r)$.

The results of ANOVA in Tab. 6.13 confirmed the uncertainty of the coil area and $\Delta\phi$ as the only significant contributions.

For the metroplogical design of the transducer, even in a so simplified configuration, the following considerations are drawn:

- The uncertainty on the coil area turned out to be predominating with respect to other sources.
- This result can be exploited to dramatically reduce the field uncertainty; if the coil relative uncertainty is decreased by one order of magnitude, the output uncertainty can be reduced more then 25 times with respect to the worst condition.

Table 6.10: Relative uncertainty values for sources classification.

Source	**Level**		
	1	2	3
$u(K_{1,2})$	1	10	-
$u(\Delta\phi)$	10^{-6}	10^{-5}	10^{-4}
$u_r(A_c)$	10^{-6}	10^{-5}	10^{-4}
$u(f_r)$	10^{-10}	10^{-6}	10^{-4}

Table 6.11: L18 plan of simulation trials for a magnetic field of 1 T.

Test	**Level**				**Result**
	$u\,(K_{1,2})$	$u\,(\Delta\phi)$	$u_r\,(A_c)$	$u\,(f_r)$	$u\,(B_1)\,[\mu T]$
1	1	1	1	1	0.625
2	1	1	2	2	5.756
3	1	1	3	3	57.56
4	1	2	1	1	2.514
5	1	2	2	2	6.255
6	1	2	3	3	57.61
7	1	3	1	2	24.48
8	1	3	2	2	25.14
9	1	3	3	1	62.55
10	2	1	1	3	0.642
11	2	1	2	1	5.763
12	2	1	3	2	57.56
13	2	2	1	2	2.518
14	2	2	2	3	6.257
15	2	2	3	1	57.56
16	2	3	1	3	24.48
17	2	3	2	1	25.14
18	2	3	3	2	62.55

Table 6.12: Results of ANOM for the magnetic field uncertainty.

Source	**unit**	**Level**		
		1	2	3
$u\,(K_{1,2})$	μT	26.95	26.95	-
$u\,(\Delta\phi)$	μT	21.32	22.13	37.39
$u_r\,(A_c)$	μT	9.211	12.39	59.24
$u\,(f_r)$	μT	25.70	26.52	28.62

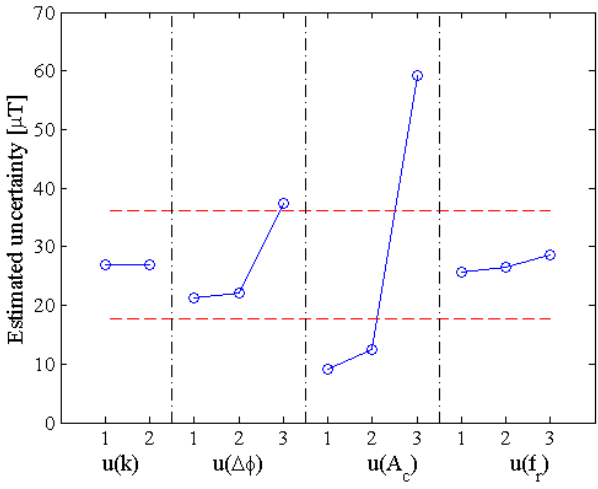

Figure 6.13: Results of ANOM for the magnetic field uncertainty

- If a source uncertainty is assessed as not significant for the output uncertainty, the corresponding measurement instrument can be downgraded in terms of metrological specifications, with an associated reduction of the costs.

In spite of the reduced number of trials (18), results corresponding to 10^5 Monte Carlo simulations are achieved. This efficiency, typical of design of experiments, arises mainly from the combined use of a polynomial model of the effects and ANOM and ANOVA [53].

Table 6.13: ANOVA results for $u\,(B_1)$.

Source	**SS**	**DF**	**VAR**	**F**	$\boldsymbol{F_t}$
$u(K_{1,2})$	0	1	0	0	10.04
$u(\Delta\phi)$	984	2	492	23.05	7.56
$u(A_c)$	9418	2	4709	220	7.56
$u(f_r)$	27.2	2	13.6	0.64	7.56
Error	213.5	10	21.4		

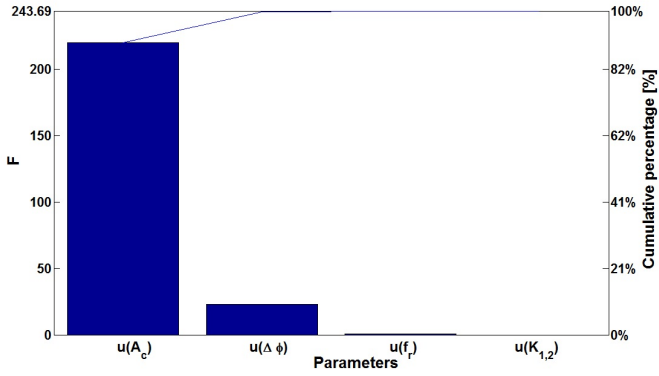

Figure 6.14: Ranking of uncertainty source impact.

6.3 Characterization

This test aims at characterizing the transducer as a whole (Fig. 5.2) by evaluating the quality of its magnetic field measurement in terms of:

- *repeatability*:

$$\pm\sigma_{B_1} = \sqrt{\frac{1}{N}\sum_{i=1}^{N}(B_1 - \bar{B_1})^2} \tag{6.1}$$

  where $\bar{B_1}$ is the average and N the number of consecutive measurements. The relation 6.1 is useful also for assessing the coils mechanical stability in a predefined rotation time interval [27, 28].

- *accuracy*, assessed as the deviation from the reference field B_1^{ref} measured by NMR:

$$\Delta B_1 = (\bar{B_1} - B_1^{ref}) + C \tag{6.2}$$

  where C is a term of correction, accounting for the different position of transducer and NMR probe in the magnet (0.08% of difference), as well as for the gain error of the integrator (0.2 - 0.3%, according to the gain, without self-calibration).

- *resolution*, that is the minimum level of field variation appreciable by the transducer, assessed as the repeatability in absence of measurand, and thus in presence only of the earth magnetic field.

Table 6.14: Field measurement quality results with transducer in longitudinal position and nominal ω of 2 rps.

B_1^{nom} (T)	$\bar{B}_1$ (T)	$\sigma_{B_1}/\bar{B}_1$ (ppm)	RMS$(\Delta\omega/\bar{\omega})$ (%)	$(\Delta\omega/\bar{\omega})_{pp}$ (%)
0.0	0.002301	74	1.96	14.48
0.2	0.199639	110	2.00	14.22
0.4	0.398831	72	1.88	14.36
0.6	0.598293	104	1.98	14.48
0.8	0.797384	86	2.04	15.16
1.0	0.999239	72	2.04	15.30

6.3.1 Experimental setup

The measurement setup (Fig. 6.8) is the same as in the previous test, and the FDI is used to acquire and integrate the coil voltage signal.

6.3.2 Test procedure

The measurement procedure consists of setting the magnetic field level B inside the reference dipole ([0.0, 0.2, 0.4, 0.6, 0.8, 1.0] T) and measuring it through the transducer for different angular rotating speeds ω ([1, 2, 3] rps). According to the classical procedure for rotating coil measurements [66], the magnetic flux is computed by integrating the coil voltage and adding the flux increments measured by the FDI triggered by the encoder pulses. In this test, only the main dipolar field component B_1, obtained from the fundamental harmonic of flux, is considered, because the transducer includes only an absolute coil.

6.3.3 Experimental results

In Tab. 6.14,the dipole field measurements (averaged on 20 revolutions) $\bar{B}_1$, the field relative repeatability $\pm\sigma_{B_1}/\bar{B}_1$, as well as the RMS and peak-to-peak $(\Delta\omega/\omega)_{pp}$ of the speed relative difference are given for a nominal ω of 2 rps at varying the nominal magnetic field B_1^{nom} .

As shown in Figs. 6.15 A and B, the 1-σ repeatability does not appear to be correlated neither to the field level, nor to rotating speed fluctuations.

In order to check the eventual effects of speed variation, the relative difference $\Delta B_1/B_1^{ref}$ (6.2) is considered with respect to the field measured by the reference

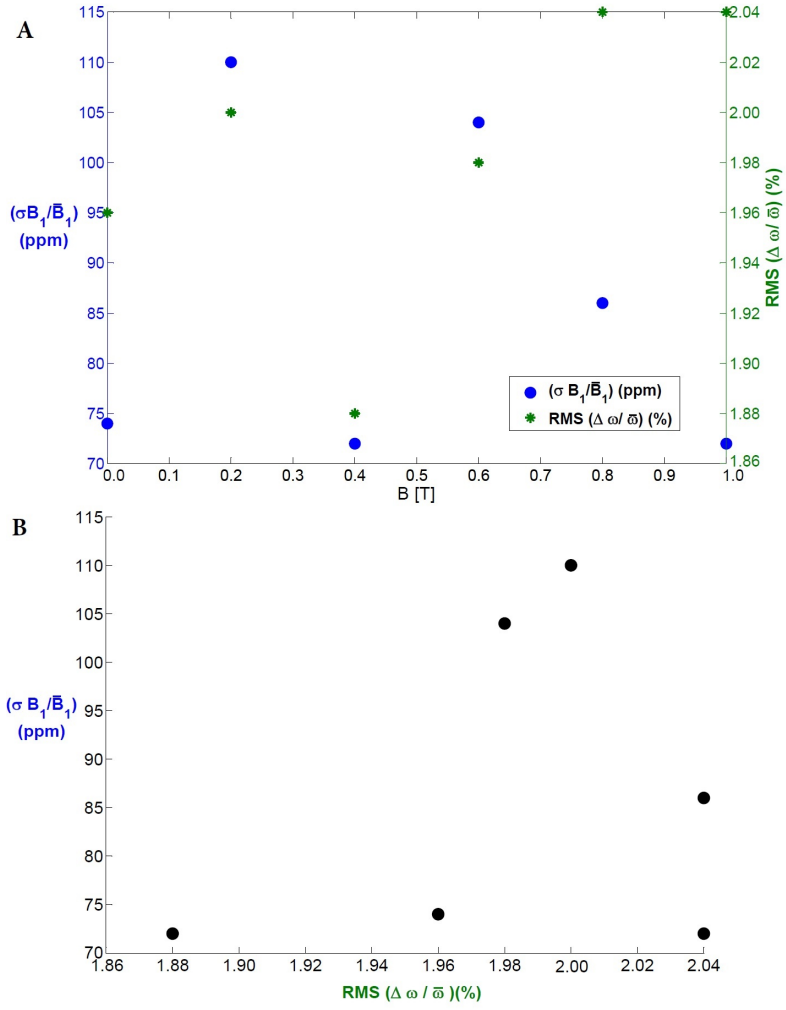

Figure 6.15: Comparison (A) and correlation (B) between magnetic field relative repeatability ($\pm \sigma_{B_1}/\bar{B_1}$) and relative angular speed rms [RMS($\Delta\omega/\bar{\omega}$)].

Table 6.15: Field measurement quality results at varying ω, for nominal magnetic field of 0.8 and 1.0 T.

ω (rps)	B_1^{ref} (T)	$\bar{B}_1$ (T)	$\Delta B_1/B_1^{ref}$ (10^{-4})	$\sigma_{B_1}/\bar{B}_1$ (ppm)	RMS$(\Delta\omega/\bar{\omega})$ (%)	$(\Delta\omega/\bar{\omega})_{pp}$ (%)
1.0	0.799788	0.797341	−0.41	102	3.32	23.54
2.0	0.799788	0.797384	0.22	86	2.04	15.16
3.0	0.799788	0.797381	0.19	214	1.92	12.12
1.0	0.998848	0.996394	−0.01	98	3.08	24.08
2.0	0.998848	0.996396	0.01	128	2.14	16.74
3.0	0.998848	0.996395	0.00	138	1.68	12.66

Table 6.16: Field measurement quality results in free space (earth magnetic field) with ω of 2.0 rps, and transducer aligned or perpendicular to north pole.

North-pole orientation	$\bar{B}_1$ (μT)	$\sigma_{B_1}/\bar{B}_1$ (%)
alignned	36.00	0.2
ortogonal	62.00	0.2

NMR probe [1], for different ω and for 2 levels of B_1. The results in Tab. 6.15 show that the measured field is repeatable within about a hundred of ppm with respect to the NMR reference (the systematic difference is due to the non-uniformity of the field inside the magnet gap). Furthermore, the repeatability worses as the rotation gets faster. The repeatability is less than the typical target value of 100 ppm at both the nominal field levels when ω is 1 rps, which is fast enough for practical applications. This result demonstrates the possibility of measuring magnetic field with the required repeatability of $\pm\sigma_{B_1}/\bar{B}_1 < 100$ ppm, without a very-high uniformity in the rotation speed (RMS $(\Delta\omega/\bar{\omega}) > 2$ %, and $(\Delta\omega/\bar{\omega})_{pp} > 10$ %). Indeed, the digital integrator (FDI) triggered by the angular encoder allows speed irregularity to be compensated, by confirming precedent results [64].

In Tab. 6.16, the results of the test carried out outside the reference magnet in presence of only the earth magnetic field are reported. These results highlight the transducer capability of measuring fields down to about 30 μT, with a relative 1-σ repeatability per revolution of $\pm$0.2%. From these results, the resolution can be assessed as the minimum variation appreciable of magnetic field. This is the repeatability in presence of the only earth magnetic field,equal to 0.07 μT (worst case, north-pole aligned orientation).

Chapter 7

Metrological characterization: Bench

The chapter presents the characterization of the full bench (transducer and "train-like" motion system). The functional tests of the motion system are preliminary reported, giving the results of the position measurements. The metrological characterization of the bench was divided into three different phases, considering: (*i*) the transducer mounting traditional wire coils and only absolute magnetic field measurement, (*ii*) the transducer with PCB coils, presented in chapters 3 and 6, evaluating main and compensated measurements, and (*i*) the profile measurements of the bench, by comparing the results with an Hall probe map. Finally, the results and the ongoing activities are discussed.

7.1 Functional Tests

The functional tests deal with the performance of the magnetic measurement system in terms of longitudinal position measurements. The experimental validation of the transducer were already carried out [13], in particular the magnetic compatibility and the speed variation of the piezomotor. The piezomotor ER-15 Nanomotion [56] was adopted also for the longitudinal motion. The installation of the motor on the trolley has followed the indication of the previous test of compatibility. In fact, the distance between the motor and the rotating coil is larger than 5 cm, such as the rotary one, in order to avoid magnetic perturbation. Another preliminary check was to quantify the necessary torque with respect to the weight of the trolley. The longitudinal position measurements have been carried out by measuring the position of the trolley by a laser interferometer (Lasertex HPI-3D [67]). The measurements have evaluated the repeatability of trolley positioning (absolute and relative) and the effective motor step length. In Tab. 7.1, the position measurements for three different motor steps number $(10000, 22000, 25000)$ have a motor step length (0.0400 mm), and a standard deviation of the number of steps over 20 consecutive measurements of about $1-2$ steps $(40-80\ \mu\text{m})$. This result has confirmed the precision of the positioning system $(< 100\ \mu\text{m})$.

Table 7.1: Position measurements by interferometer: mean and repeatability over different lengths.

Mot. steps N_s	$\overline{s}$	l_{step}	$\sigma\ (l_s)$	$\sigma\ (N_s)$
–	(mm)	(mm)	(mm)	–
10000	400.8048	0.04009	0.034	0.86
22000	881.9611	0.04009	0.009	0.49
25000	1100.0586	0.04009	0.009	2.05

On the opposite side, the ferromagnetic components of the piezomotor (shaft and ball bearings made in martensitic steel) limit the use of this kind of motion system in the magnetic field. In fact, for a field bigger than 0.4 T, the piezomotor is not able to actuate correctly the trolley in the fringe fields of the magnet. Conversely, the position performance is confirmed in an uniform field (tests until 1.0 T).

7.2 Characterization

The experimental characterization of the bench aims at verifying the quality of the magnetic field measurements in terms of repeatability, accuracy, and resolution. The second topic is to verify the results with respect to the previous ones presented in [13]. In particular, the impact of the train-like motion system on the measurements must be checked: as a matter of fact, the previous transducer was positioned and fixed manually in the magnet.

The measurement setup (Fig. 7.1) is based on a Fast Digital Integrator (FDI [18]) used to acquire and integrate the coil voltage signal, and an interface device with two motor controller cards (longitudinal and rotating motors), a power supply block, and an encoder interface used to acquire the encoder pulses. The measurement was elaborated by means of the Flexible Framework for Magnetic Measurements (FFMM) [19] (C++ program) running on a PXI PC workstation, and the result were analyzed in Matlab®. The measurement procedure was to set the magnetic field inside the reference dipole and to measure it through the rotating coil (Fig. 5.6) in a fixed position of the magnet (Fig. 7.1).

Table 7.2: Magnetic field measurements for experimental characterization of bench.

ω	B_1^{ref}	$\bar{B}_1$	$\Delta B_1/B_1^{ref}$	$\sigma_{B_1}/\bar{B}_1$
(rps)	(T)	(T)	(10^{-4})	(ppm)
1	0.399539	0.399480	-1.23	18
1	0.998848	0.998570	0.19	27

In Tab. 7.2, the dipole field measurements (averaged on 20 revolutions) $\bar{B}_1$, the field relative repeatability $\sigma_{B_1}/\bar{B}_1$, and relative accuracy $\Delta B_1/B_1^{ref}$ are reported for two nominal field values B_1 (0.4 and 1.0 T). The results show that the measured field is repeatable within about a hundred of ppm with respect to the average value $\bar{B}_1$. The relative accuracy $\Delta B_1/B_1^{ref}$ is equal or less of about $1 \cdot 10^{-4}$. These preliminary results have confirmed the previous ones presented in [13], and then the positioning system did not worsen the measurement performance.

7.2.1 PCB coil measurements

A second campaign of experimental characterization was carried out by mounting two PCB coils on the transducer (Fig.7.2). As described in chapter 7 for the transducer,

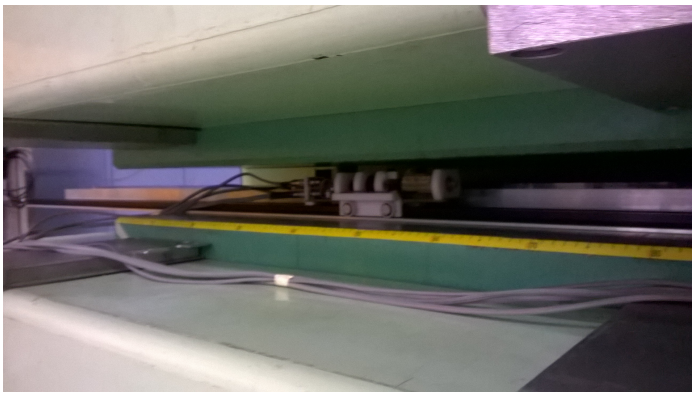

Figure 7.1: Characterization measurements of the full system in a dipole magnet.

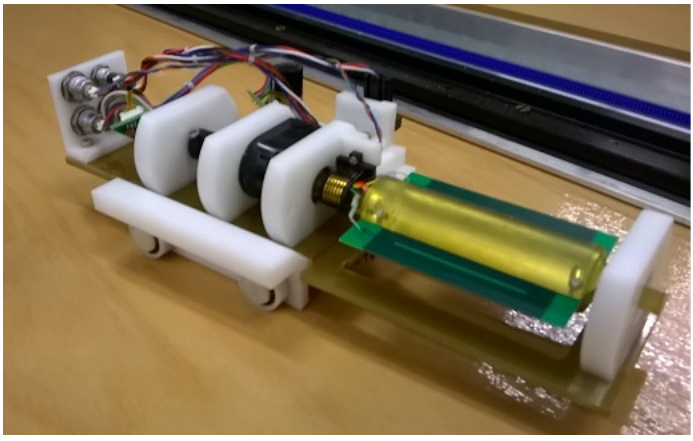

Figure 7.2: Rotating coil transducer with PCB coils.

these measurements aim at characterizing the bench of the rotating coil magnetic field mapper as a whole. This is carried out by evaluating (1) the quality of absolute magnetic field measurement in terms of repeatability, accuracy and resolution (as reported in chapter 7), and (2) the quality of the relative magnetic field harmonics in terms of repeatability (homogeneous and fringe field region). Differently from the Eq. 6.2, the correction C of the relative difference must take into account also the voltage drop of the coil, due to the not negligible coil resistance (2.5 kΩ) with respect to the input one of the integrator (400 $k\Omega$). Eq. 6.2 becomes:

$$\Delta B_1 = \bar{B_1} - B_1^{ref} + (r_{FDI} \cdot \bar{B_1} - r_R \cdot \bar{B_1} + r_{field} \cdot \bar{B_1}) \tag{7.1}$$

where the r_{FDI} is the factor from the calibration of the integrator ($0.3 - 0.4\%$), r_R takes into account the resistance difference between coil and integrator (0.6 and 0.2% for the two PCB coils with 410 and 100 turns), and r_{field} is the factor due to the systematic difference between the coil and NMR position in the reference dipole magnet (0.01%).

Another important feature is to verify the performance of the transducer for local measurements, in particular, the capability to measure relative harmonics. The *harmonics repeatability* is defined as :

$$\pm\sigma_{b_n} = \sqrt{\frac{1}{N}\sum_{i=1}^{N}(b_n^i - \bar{b_n})^2} \tag{7.2}$$

and

$$\pm\sigma_{a_n} = \sqrt{\frac{1}{N}\sum_{i=1}^{N}(a_n^i - \bar{a_n})^2} \tag{7.3}$$

where b_n and a_n are the normal and skew multipoles, $\bar{b_n}$ and $\bar{a_n}$ are the average multipoles and N the number of consecutive measurements. The bucking (or compensation) ratio between the two coil signals (main and compensation coils) is to be considered for both the PCB coils and with the transducer immersed in homogeneous and fringe field region. As presented in [66], the bucking ratio β_n is the ratio between the absolute and compensated measurement of the transformed flux harmonics. In the case the ratio considers the dipole compensation, it is computed as:

$$\beta_1 = \frac{\Phi_1^{abs}}{\Phi_1^{cmp}} \tag{7.4}$$

where Φ_1 is the dipole component of the magnetic flux, and the superscript ^{abs} and ^{cmp} indicate the absolute and compensated measurements. The goodness of the dipole

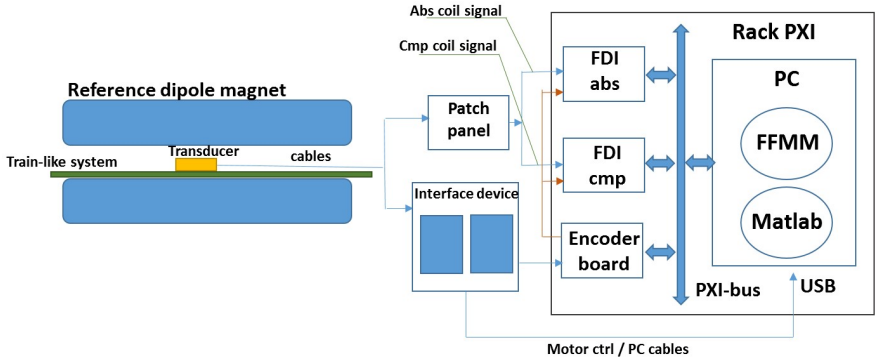

Figure 7.3: Measurement setup: scheme of connections among the different blocks.

compensation is assessed by the module of β_1, and the angular error between the coils is given by the phase of β_1.

7.2.2 Experimental setup

The measurement setup for the final coil (Fig. 7.3) is different from the one in Fig. 7.1 and Tab. 7.2 used for the wire coils. As shown in Fig. 7.3, the transducer is placed into the homogeneous and/or fringe field region of the reference dipole magnet. The compensation scheme for the dipole is implemented analogically by a patch panel that receives the voltage signals from the main and compensation coils. The two signals (Absolute and compensation coil signals, "*Abs*" and "*Cmp*" in the Fig. 7.3) are acquired by two FDIs (Fast Digital Integrators [18]). The integrators are triggered by the encoder pulses, directed before through the interface device (presented in chapter 6), and then through the encoder board. This aims at counting the encoder pulses, at managing the number of pulses per revolutions by interpolation or decimation, and triggering the FDIs acquisition. The rotation speed and direction are managed by the motor controller card installed into the interface device, that is driven by software through USB connection. The measurement is elaborated by FFMM C++ software framework and the data analysis by Matlab®, as in the previous test.

7.2.3 Test procedure

The measurement procedure provides two different positions of the transducer with respect to the features to characterize. Regarding the repeatability and accuracy of the main field measurements, the setup is shown in Fig. 7.4-A. The transducer was

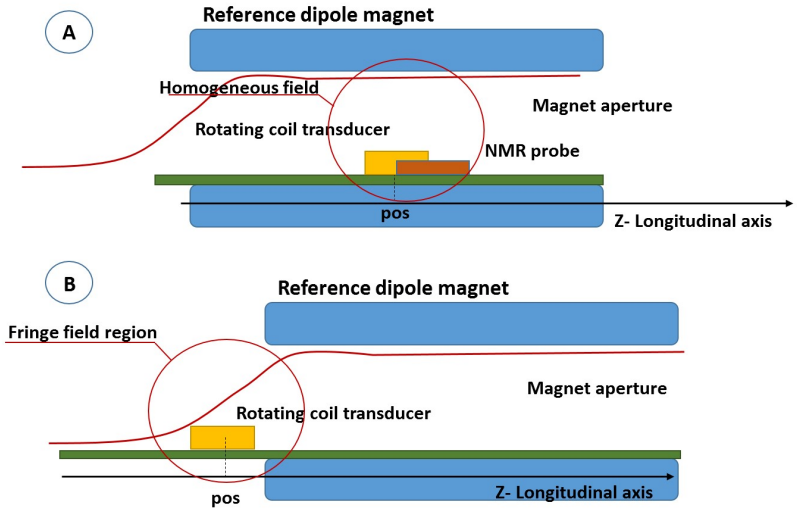

Figure 7.4: Measurement setup: A) repeatability and accuracy of the main field measurements, and B) harmonics repeatability in fringe field region.

placed into homogeneous field region of the reference dipole, and a NMR probe was installed close to it for checking the main field strength. Regarding the harmonics repeatability, the transducer was placed into the fringe field region (Fig. 7.4-B) in order to have an appreciable number and strength of harmonics, otherwise negligible into homogeneous field. For resolution measurements or earth magnetic field measurements, the transducer and the train-like motion system were put outside the reference dipole and far to magnetic field sources.

Such as the previous test (Chapter 7) for main field repeatability and accuracy, the measurement procedure consists of setting the magnetic field level B inside the reference dipole ([0.0, 0.2, 0.4, 0.6, 0.8, 1.0] T) and measuring it through the transducer, in this case, with a fixed rotation speed of 1 rps. According to the classical procedure for rotating coil measurements [66], the magnetic flux is computed by integrating the coil voltage and adding the flux increments measured by the FDI triggered by the encoder pulses. In this test, only the main dipolar field component B_1, obtained from the fundamental harmonic of flux, is considered. Viceversa, only the relative harmonics, derived from the compensated signals, are taken in account for harmonics repeatability. Indeed, the standard analysis procedure [66] establishes that the absolute signal is used for the determination of the main field component (dipole in the case study), or for the verification of it. The compensated signal, obtained as a

Table 7.3: Field measurement quality results with the transducer mounting the PCB coil (410 turns) in homogeneous field region for nominal magnetic field of [0.2, 0.4, 0.6, 0.8, 1.0] T.

B_1^{nom} (T)	B_1^{ref} (T)	$\bar{B}_1$ (T)	$\Delta B_1/B_1^{ref}$ (10^{-4})	$\pm\sigma_{B_1}/\bar{B}_1$ (ppm)
0.2	0.200226	0.200521	0.0	102
0.4	0.399972	0.400597	0.8	145
0.6	0.599531	0.600348	1.1	112
0.8	0.799610	0.800640	1.8	122
1.0	0.999590	1.000988	0.7	101

Table 7.4: Field measurement quality results with the transducer mounting the PCB coil (100 turns) in homogeneous field region for nominal magnetic field of [0.4, 0.6, 0.8, 1.0] T.

B_1^{nom} (T)	B_1^{ref} (T)	$\bar{B}_1$ (T)	$\Delta B_1/B_1^{ref}$ (10^{-4})	$\pm\sigma_{B_1}/\bar{B}_1$ (ppm)
0.4	0.400191	0.401108	1.1	192
0.6	0.600009	0.601373	1.5	72
0.8	0.800180	0.801996	1.3	167
1.0	1.000031	1.002109	0.2	133

combination of the signals of the two coils (for dipole compensation), is used for the determination of the field errors (harmonics of the field not wanted).

7.2.4 Experimental results

Accuracy, repeatability and resolution. In Tab. 7.3, the dipole field measurements (averaged on 20 revolutions) $\bar{B}_1$, the field relative repeatability $\pm\,\sigma_{B_1}/\bar{B}_1$, and the accuracy $\Delta B_1/B_1^{ref}$, relative to NMR measurements, B_1^{ref} at varying the nominal magnetic field B_1^{nom} are reported for the transducer mounting the PCB coil with 410 turns and placed to homogeneous field (Fig. 7.4-A).

The relative accuracy is about $1 \cdot 10^{-4}$ with respect to the NMR reference, and such as the previous results (chapter 7), the systematic difference is due to the non-uniformity of the field inside the magnet gap. The repeatability is worse than the last prototype. The typical target is to have a repeatability less than 100 ppm, and in the considered case, it is bigger than 100 ppm.

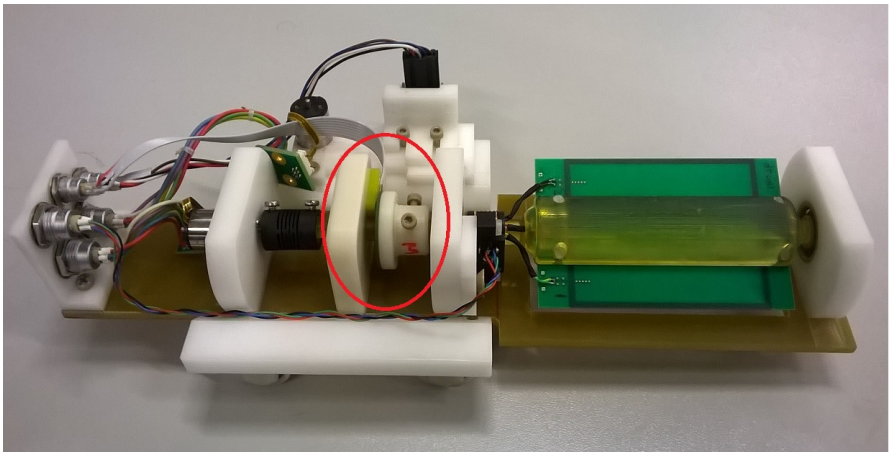

Figure 7.5: Rotating coil transducer with PCB coil of 100 turns and the capacitive encoder (red circle).

Tab. 7.4 reports the results of the same test for the PCB coil with 100 turns (Fig. 5.4-B) and an encoder by Posic, as shown in the Fig. 7.5. Practically, the results are the same of the previous coil (PCB with 410 turns). Considering also the change of the encoder, the detoriation of the performance in terms of repeatability could be due to the mechanics, and in particular to the change of the shaft (from the glassfiber one to the plastics one). This aspect must be investigated in the ongoing activities. Regarding the resolution, the measurements carried out in presence of only the earth magnetic field have highlighed a worsen of the relative 1-σ repeatability per revolution of $\pm 1\%$ (the previous prototype had a repeatability of ± 0.2). From this, the resolution measured was equal to 0.6 μT in the north pole aligned orientation of the transducer (worst case) with a main field of about 60 μT.

Harmonics repeatability. The tests considered the measurements of system positioned in a specific fringe field position, repeated for both the PCB coils. The Tabs. 7.5 and 7.6 report the results of the *harmonics repeatability* tests evaluated in the configuration of the Fig. 7.4-B for the PCB coils with 100 and 410 turns, respectively. In particular, the repeatability of the normal and skew harmonics, absolute and compensated, ($\pm\sigma_{b_n}$ and $\pm\sigma_{a_n}$) over 20 consecutive acquisitions are reported. The results show a repeatability of the compensated harmonics less than 10^{-4}, and the performance of the PCB coil with 100 turns, the smallest one (magnetic surface of about 0.10803 m^2), are better than the PCB coil with 410 turns (0.25803 m^2).

Table 7.5: Harmonics repeatability results for the transducer in fringe field region mounting the 100 turns PCB coil for nominal magnetic field of 0.4 T and reference radius R_{ref} of 0.024 m.

order	$\bar{b_n}^{abs}$	$\bar{a_n}^{abs}$	$\pm\sigma_{b_n}^{abs}$	$\pm\sigma_{a_n}^{abs}$	$\bar{b_n}^{cmp}$	$\bar{a_n}^{cmp}$	$\pm\sigma_{b_n}^{cmp}$	$\pm\sigma_{a_n}^{cmp}$
-	(10^{-4})	(10^{-4})	(10^{-4})	(10^{-4})	(10^{-4})	(10^{-4})	(10^{-4})	(10^{-4})
2	−89.97	−152.48	3.39	2.75	−26.15	−194.46	0.44	0.17
3	201.30	1.44	1.53	1.95	195.57	0.32	0.14	0.37
4	−0.30	8.98	1.20	1.62	−4.07	8.47	0.31	0.16
5	−4.05	−0.86	1.28	0.65	−2.61	−0.56	0.13	0.14
6	0.90	0.33	0.90	0.62	0.33	0.18	0.06	0.17

Table 7.6: Harmonics repeatability results for the transducer in fringe field region mounting the 410 turns PCB coil for nominal magnetic field of 0.4 T and reference radius R_{ref} of 0.024 m.

order	$\bar{b_n}^{abs}$	$\bar{a_n}^{abs}$	$\pm\sigma_{b_n}^{abs}$	$\pm\sigma_{a_n}^{abs}$	$\bar{b_n}^{cmp}$	$\bar{a_n}^{cmp}$	$\pm\sigma_{b_n}^{cmp}$	$\pm\sigma_{a_n}^{cmp}$
-	(10^{-4})	(10^{-4})	(10^{-4})	(10^{-4})	(10^{-4})	(10^{-4})	(10^{-4})	(10^{-4})
2	−25.36	−185.00	2.16	5.39	−27.31	−196.77	0.07	0.25
3	207.46	−8.58	2.23	3.18	196.77	−4.82	0.25	0.19
4	3.28	6.44	1.53	1.06	1.89	8.61	0.20	0.33
5	−3.18	−3.56	1.40	0.88	−2.98	−0.17	0.15	0.17
6	1.78	1.05	0.99	1.56	0.14	0.04	0.18	0.13

The main harmonics (a_n and b_n for $n = 1, ..., 6$) are compatible for both the coils, considering the repeatabilities as $\pm 3\sigma$, except for the quadrupole harmonics of the 100 turns coil, and the sextupolar normal component, b_3, of the 100 turns one, due to a rotation error and / or a longitudinal displacement between the coil position. This effect is also shown in the Figs. 7.6 and 7.7, where are graphed the absolute value of the c_n complex harmonics (defined as $c_n = b_n + ia_n$), and in particular, the superimposition of the harmonics and how the compensation eliminates the rotation error on the harmonics.

Fig. 7.8 shows the normal and skew harmonics comparison of the two coils in the same position, highlighting the reproducibility of the system, within the $2 \cdot 10^{-4}$, using two different coils. The unique differences are for the b_4 and a_3, where the harmonics present a sign inversion, due to the coil design differences and/or sensitivity factor (to be investigated further).

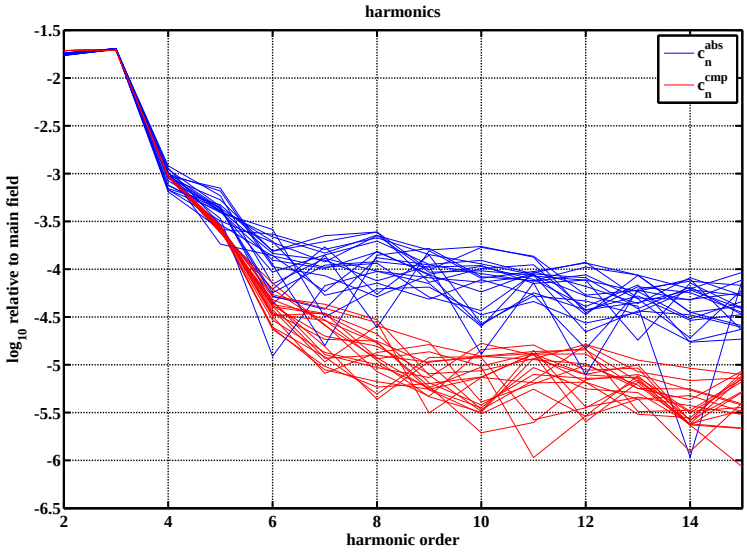

Figure 7.6: Harmonics c_n (absolute and compensated) measured by the 100 turns pcb coil in the fringe field region of the reference dipole ($B_1^{ref} = 0.4$ T).

Table 7.7: Harmonics repeatability results for the transducer in homogeneous region (magnet center) mounting the 410 turns PCB coil for nominal magnetic field of 1.0 T, reference radius R_{ref} of 0.024 m and bucking ratio of 358.

order	$\bar{b_n}^{abs}$	$\bar{a_n}^{abs}$	$\pm\sigma_{b_n}^{abs}$	$\pm\sigma_{a_n}^{abs}$	$\bar{b_n}^{cmp}$	$\bar{a_n}^{cmp}$	$\pm\sigma_{b_n}^{cmp}$	$\pm\sigma_{a_n}^{cmp}$
-	(10^{-4})	(10^{-4})	(10^{-4})	(10^{-4})	(10^{-4})	(10^{-4})	(10^{-4})	(10^{-4})
2	-52.14	-26.00	1.58	4.59	-0.16	-0.47	0.01	0.01
3	2.81	-8.05	2.46	2.51	0.08	-0.02	0.02	0.01
4	4.04	1.92	2.39	1.58	0.07	0.03	0.01	0.01
5	-2.76	0.22	1.92	1.63	-0.02	0.05	0.01	0.01
6	-1.29	1.97	1.55	1.30	-0.05	0.01	0.01	0.01

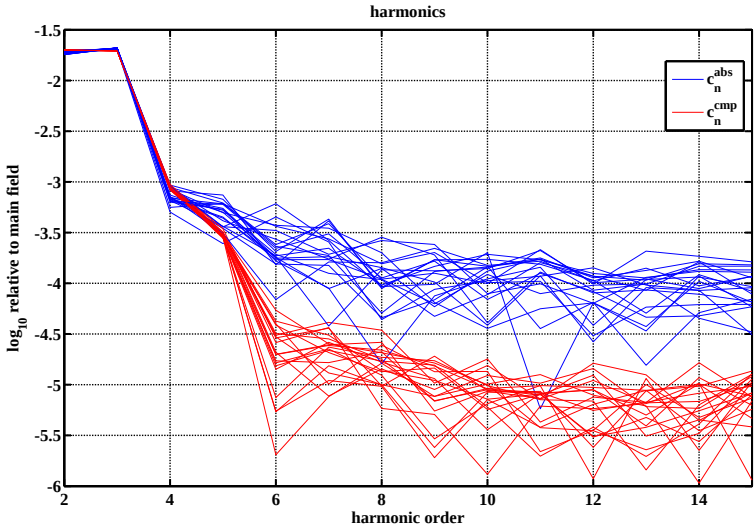

Figure 7.7: Harmonics c_n (absolute and compensated) measured by the 410 turns pcb coil in the fringe field region of the reference dipole ($B_1^{ref} = 0.4$ T).

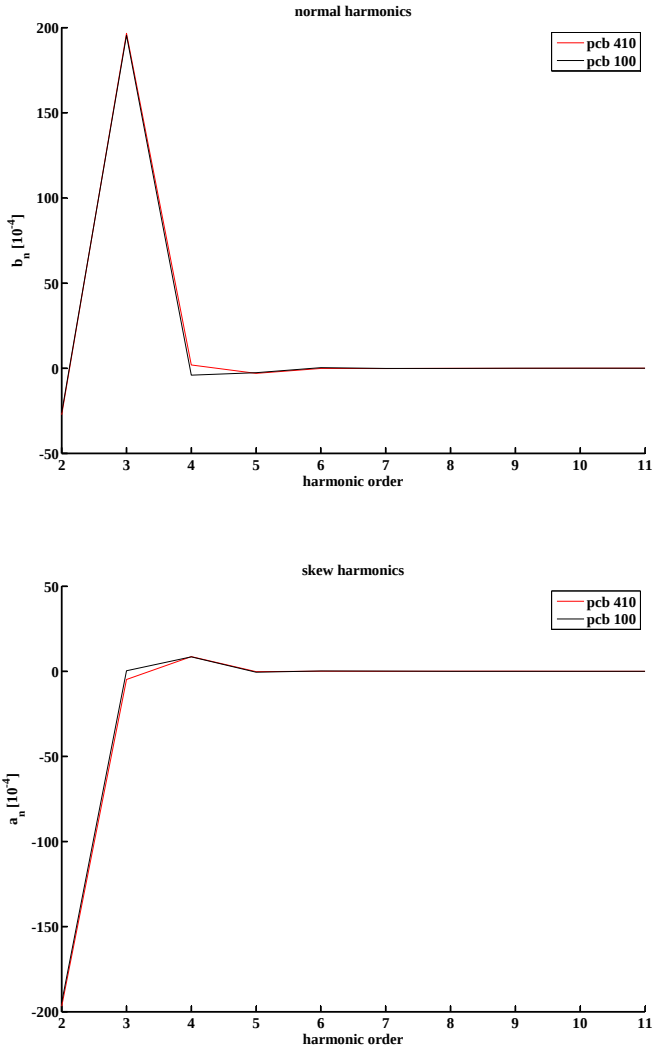

Figure 7.8: Comparison graph between the normal and skew harmonics of the two coils in the fringe field region of the reference dipole ($B_1^{ref} = 0.4$ T).

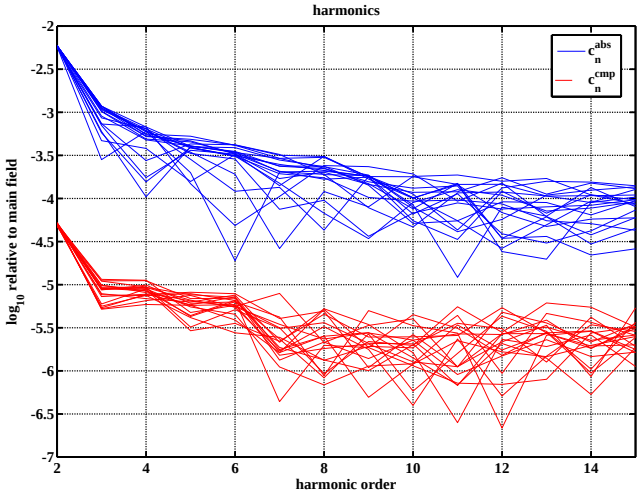

Figure 7.9: Harmonics c_n (absolute and compensated) measured by the 410 turns pcb coil in the homogeneous region of the reference dipole ($B_1^{ref} = 1.0$ T, $R_{ref} = 0.024$ m).

Harmonics - reference dipole magnet. Evaluating the harmonics measurements at the center of the reference dipole magnet (Fig. 7.4-A), the tests have verified also the quality of this magnet, that usually used for the calibration of the coils at CERN magnetic measurement section [68]. The Tab. 7.7 reports the harmonics repeatability (absolute and compensated) measured by 410 turns pcb coil, showing relative harmonics less than 10^{-4}, and repeatability of about 10^{-6}. This result demonstrates the quality of the dipole field used for the calibration of the coils, usually mapped by NMR probe. The Fig. 7.9 shows the normalized harmonic coefficients($log_{10}(|c_n|)$), and in particular, the difference between the absolute and relative coefficients. This difference is mainly due to the rotation quality of the probe, and to the feed down effect [66], considering that the coil is not at center.

Bucking ratio. The bucking ratios (Eq. 7.4) were equal to 167 and 152, respectively, showing a good compensation of the vibration also into fringe field region (Fig. 7.4-B). The best performance of the coil 100 turns is justified by the bucking ratio difference. In the homogeneous field region, the bucking ratios showed the best performance for both the coils, 358 and 515 for the PCB coils with 410 and 100 turns, respectively. As assessed after for the magnetic profile measurements, when the coil

body is completely immersed in homogeneous field, the coil sensitivity (i.e. K_n) takes into account the variation of the PCB loops. While, if the coils are immersed in the fringe field (or z-gradient region), the error measurement due to the end-probe effect is maximum. The worst case for the measurements (main field and harmonics) is when the coil end and the coil body are in two different field regions, namely fringe field and homogeneous region.

7.3 Magnetic profile measurements

The measurements of the magnetic field in the fringe field region is one of the main requirements to be verified for the proposed mapper. In particular, the mapper should measure the profile of the magnetic field (absolute measurement) and also the multipole profile (relative measurements). A Hall probe system was assumed as reference.

7.3.1 Measurement setup

The measurement setup (Fig. 7.3) is composed by the rotating coil transducer and the train-like motion system (objects under test), the PXI acquisition and workstation rack, the interface device for controlling the piezomotors, and the dipole magnet of the magnetic measurement section. The 3D Hall probe (Fig. 7.10, up) is a B-field sensor [69]) mounted on a controller board (BATCAN [70]), as shown in Fig. 7.10 (down). The probe was fixed on a glass fiber plate and then fixed on the trolley by replacing the coil.

7.3.2 Procedure

The test procedure consists of scanning longitudinally the magnetic profile of the reference dipole magnet by means of the rotating coil transducer, in different points ($n = 1, ..., N$), by overlapped measurements (Fig.7.11). The length of the fringe field region of the reference dipole is 400 mm (i.e. five times the aperture height 80 mm). The rotating coil was moved by steps of about 20 mm, and for each measurement, 30 consecutive acquisitions (i.e. coil revolutions) were carried out. The same profile was scanned by a 3D Hall probe [69] (B-field transducer, Fig. 7.10). Then, the probe was installed on the same shaft instead of the PCB coil board. This allowed to have a geometrical reference for the measurements, and to align the Hall probe with respect to the vertical dipole field (B_y) by using the angular position system of the piezomotor. The Hall probe scanning for technical simplicity has considered seven

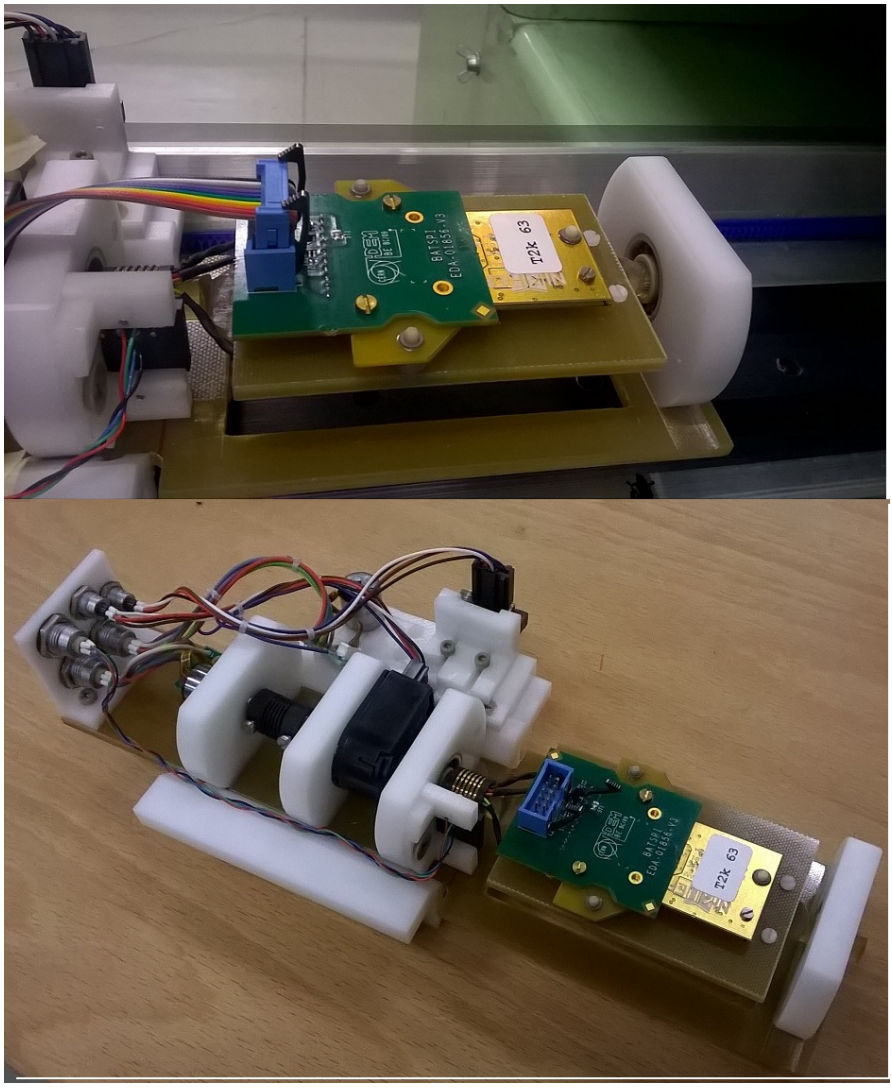

Figure 7.10: Reference 3D Hall probe for mapping the dipole magnet profile: particular of the probe (up), and mounted on the trolley (down).

longitudinal lines, displacing the probe and the train-like system in seven transverse positions ($x = [-30, -20, -10, 0, +10, +20, +30]$ mm) aligned with the coil axis. The Hall probe, a cube with three Hall elements, is positioned axially with respect to the coil at a distance of about 4 mm, i.e. transverse coordinate with respect to the coil axis $x = 0$ and $y = 4$ mm.

Each longitudinal line scan of the Hall probe consisted of 92 measurement points, separated by 8 mm for a full range of 736 mm. For each measurement point, 10 consecutive magnetic field measurements (B_x, B_y, and B_z) were performed. In order to compare the results of the two systems, the Hall probe measurements were interpolated transversely along the axis x, considering the longitudinal scans aligned and parallel. The interpolation is a polynomial fitting along x, defined as a polynomial of fifth degree:

$$B_y(x) = P_1 + P_2 \cdot x + P_3 \cdot x^2 + P_4 \cdot x^3 + P_5 \cdot x^4 + P_6 \cdot x^5 \tag{7.5}$$

where the coefficients P_i ($i = 1, ..., 6$) are the field harmonics of B_y component (P_1 is the dipole B_1, P_2 the quadrupole B_2, and so on), scaled by the reference radius R_{ref}.

The analysis considers the magnetic field component B_y and the dipole component B_1. The measurements of the two systems are compared by averaging the Hall probe maps on the coil length.

7.3.3 Results

The first analysis of the profile measurements deals with the reconstruction of the B_y magnetic field component, taking in account only the central longitudinal Hall scan ($x = 0$). Fig. 7.12 compares the rotating coil (red line, PCB coil 100 turns) and the Hall probe scan (blue line). The two measures seem to follow the same line, and the proposed transducer seems to reconstruct the B_y component correctly. The relative error between the measurements

$$E_{B_y} = \frac{B_y^{hall} - B_y^{coil}}{B_y^{coil}} \tag{7.6}$$

shown in Fig. 7.13 highlights that the accuracy of the rotating coil measurement varies longitudinally. Indeed, the relative error increases with the measurements approaching the magnet aperture, with a maximum of about 2%, and decreases in the

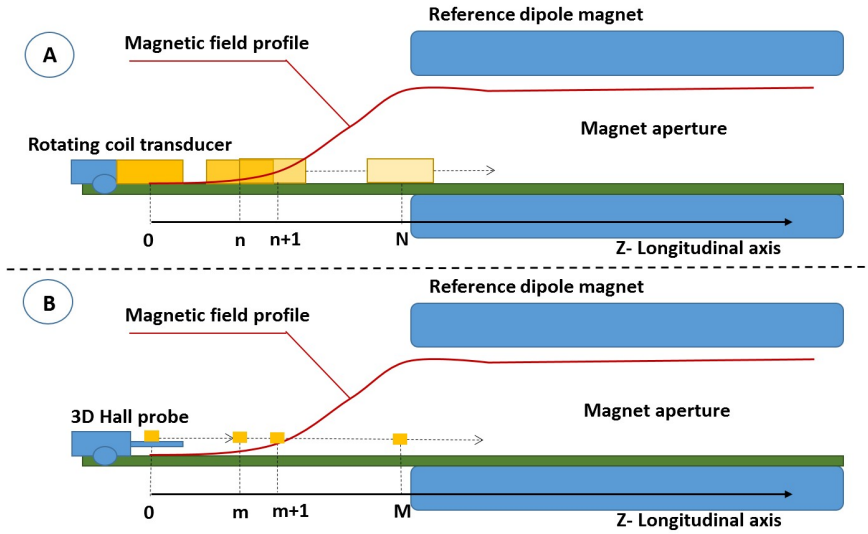

Figure 7.11: Profile measurements in fringe field region of the reference dipole magnet along the longitudinal axis: (A) rotating coil transducer, and (B) 3D Hall probe

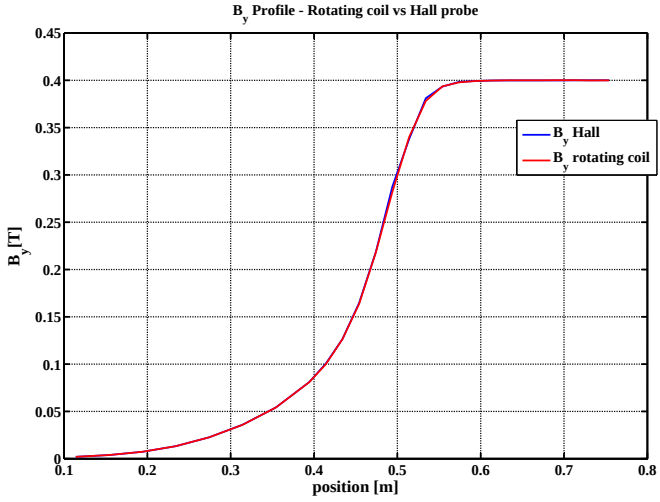

Figure 7.12: Profile measurements of the B_y magnetic field component in fringe field region of the reference dipole magnet: comparison between the rotating coil and Hall probe measurements.

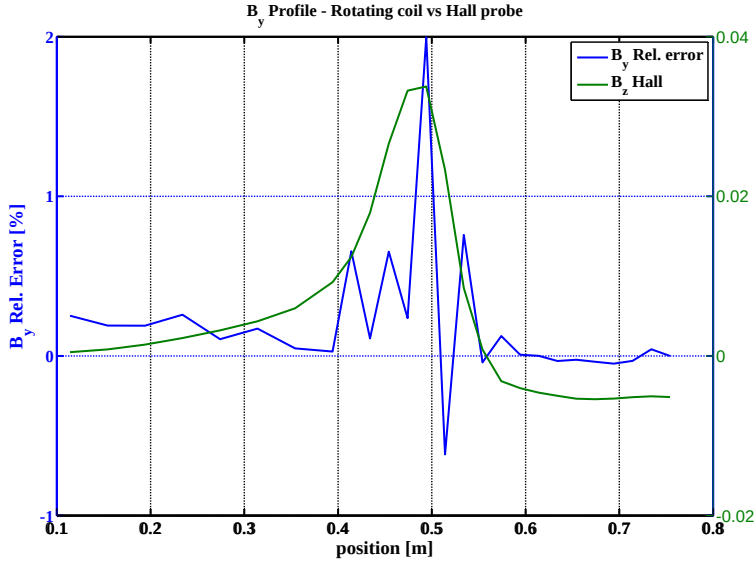

Figure 7.13: Comparison between the z-component profile, B_z of magnetic field measured by 3D Hall probe and the error of B_y profile measurements (Rotating coil vs Hall probe).

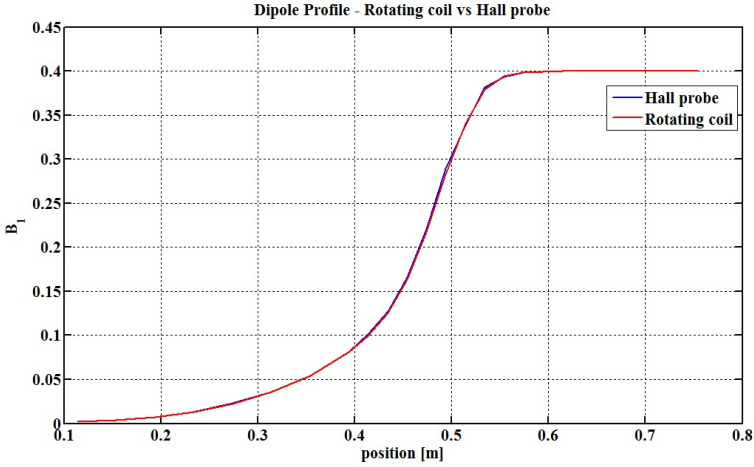

Figure 7.14: Dipole profile measurements in fringe field region of the reference dipole magnet: comparison between the rotating coil and Hall probe measurements.

homogeneous region, with a minimum of $\pm 2 \cdot 10^{-4}$. Excepting for positioning systematic errors, this difference arises mainly from the component B_z of the field. As anticipated in the previous section, the rotating coil in the fringe field region intercepts, in addition to the transverse components, also the longitudinal one (B_z), which is absent in the region of the homogeneous field, and maximum in the fringe field region (i.e. the magnet aperture entrance). This is mainly due to the end-probe effect in the fringe fields. Indeed, the maximum relative error corresponds to the maximum value of B_z.

Another evidence is given by considering the dipole component profile (B_1), shown in Fig. 7.14. Fig. 7.15 shows analogous trend and correspondence between the relative error and the B_z component.

In Fig. 7.16, the comparison between the profile of B_z and the bucking ratio for the dipole, β_1, evaluated by the compensated signal (Eq. 7.4), point by point, confirms the trend. Indeed, the bucking ratio decreases when the B_z component varies, and reaches the maximum value in the homogeneous region, such as expected. Practically, when the two coils (absolute and compensation) are in the fringe field region, the induced voltage is generated not only from the transverse component, i.e. the dipole, but also from the longitudinal one. The strength of B_z is strongly dependent on the radius, and for this reason, the effect is not compensated by the coils, which are in two different radii.

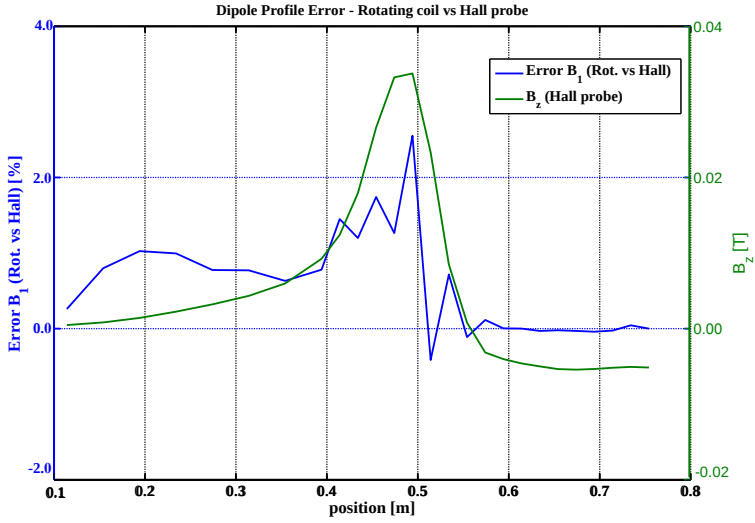

Figure 7.15: Comparison between the z-component profile, B_z of magnetic field measured by 3D Hall probe and the error of B_1 profile measurements (Rotating coil vs Hall probe).

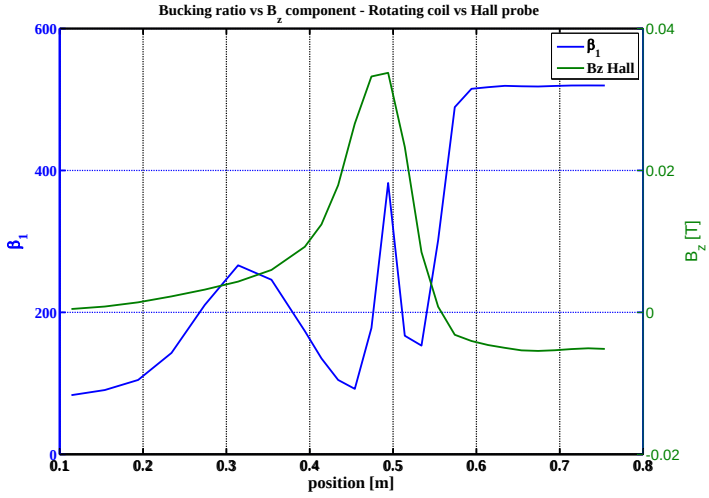

Figure 7.16: Comparison between the z-component profile, B_z of magnetic field measured by 3D Hall probe and the bucking ratio β_1 of the rotating coil measurements along the magnet profile.

7.4 Discussion

The functional tests highlighted that the motion system satisfies the requirements of precision (< 100 μm). The ferromagnetic components of the piezomotor limit its use (magnetic field less than 0.4 T).

In the experimental characterization of the prototype, the preliminary results related to the traditional wire coil (0.1237 m^2) confirmed the magnetic measurement performance in terms of repeatability (< 100 ppm) and accuracy (about 10^{-4}) with respect to the proof-of-principle transducer [13].

In the measurements of the transducer mounting PCB coils (100 and 410 turns with 0.1803 and 0.25803 m^2 of magnetic surface), the relative accuracy has confirmed the above mentioned results, while the repeatability is worse (> 100 ppm). This is due to the many changes in the mechanics of the trolley, and probably to the fixing of the coils on the shaft. The resolution, assessed as repeatability in presence of only the earth magnetic field, was of 0.6 μT.

In the tests in the fringe fields, the results have shown a harmonics repeatability (compensated signal) less than 10^{-4} for both the coils. The Figs. 7.6 and 7.7 highlight the effect of the compensation and how this eliminates the rotation error on the harmonics. The comparison between the results of the two coils (Fig. 7.8) highlights the reproducibility of the system (b_4 and a_3) at varying the coil design.

The measurements carried out in the homogeneous field of the reference dipole magnet have shown the magnetic field quality (homogeneity) of the magnet (high-order harmonics less than 10^{-4}) used for the calibration of the coils. The results reported in Tab. 7.7 and Fig. 7.9 underline also the compensation performance of the coil (bucking ratio of 358), looking at the difference between the absolute (*abs*) and relative harmonics (*cmp*).

Regarding the bucking ratio of the measurements, the best performance of both the coils were achieved in the homogeneous field (358 and 515 for the PCB 410 and 100), while in the fringe field, the bucking ratio is worse, according to [29]. The PCB 100 turns (magnetic surface smaller than the 410 turns) showed the best performance with respect to the other coil, because the coil 100 has a design with a limited end-probe surface (see chapter 3).

The profile measurements have highlighted how the rotating coil magnetic field mapper reconstructs the magnetic field profile (magnetic field component B_y and dipole component B_1) of the reference dipole magnet. The results reported in the Figs. 7.12 and 7.14 show that the reconstruction by rotating coil follows the same line of the Hall probe measurements. Regarding the field errors between the two

measurements (Figs. 7.13 and 7.15), the main mismatches are related to the B_z component of the magnetic field: the peak of the errors (about 2%) are in the same position of the B_z one. The effect of the longitudinal B_z component on the rotating coil measurements is also verified by comparing this with the bucking ratio of the coil in the longitudinal profile (Fig. 7.16). These results have demonstrated that the classical coil design is not able to evaluate this kind of measurements (fringe field), but it needs for a new design in order to avoid the longitudinal component effect. A possible solution is to substitute the radial design with a new tangential design, which provides iso-perimetric coils, and with a new compensation scheme.

Conclusions

In this Thesis, a magnetic field mapper based on rotating coils has been presented. The requirements, the architecture, the conceptual design, and the prototype for straight magnets were shown. A magnetic field mapper based [71] on (i) a rotating coil transducer [13] (ii) a train-like system for longitudinal motion and positioning inside magnet bore, is proposed. The mapper allows a localized measurement of magnetic fields and the variation of the harmonic multipole content in the magnet ends.

The proof-of-principle demonstration and the experimental characterization [13] of the rotating-coil transducer specifically conceived for mapping validated the main objective of satisfying the magnetic measurement needs of the next generation of compact accelerators. Results of tests on the magnetic compatibility of its motor point out a perturbation tolerance area with a radius of 4 cm. Test results about of speed variation show a RMS and peak-to-peak fluctuations of about 2% and 20%, respectively. In fact, these are well acceptable for magnetic measurements in the rotating coil method using a digital integrator for determining the flux increment between two trigger signals from the angular encoder. As a matter of fact, the inherent re-parametrization with respect to the shaft's angular position makes the method intrinsically robust to the speed variations, if the input voltage offset is constant during the measurement. The impact of vibrations on the measurement of harmonics remains to be assessed. The 1-*sigma* repeatability per revolution of magnetic field absolute measurements (dipole B_1) is less than ± 100 ppm and the relative difference is about constant in the same condition. Another important result is the transducer resolution, about 0.07 mT, assessed as the minimum appreciable variation in measuring only the earth magnetic field for different orientations.

Furthermore, in Chapter 4, a method [14] for the uncertainty estimation and sources classification is applied to rotating coil transducers for magnetic measurements. A straightforward case study on the above rotating coil transducer for field

mapping [13] has been presented with the specific aim of illustrating the procedure. The experimental results of expectations and uncertainties for different magnetic fields were compatible with the measurements in [13]. Moreover, the proposed approach ensures by 18 trials the same results obtained by 105 Monte Carlo simulations. The ANOM and ANOVA analysis have shown that the coil area is predominating with respect to other sources. This can be used to reduce the uncertainty by 25 times. The sources relative to the digital integrator are assessed as not significant, so theoretically, the digital integrator performance can be downgraded, by reducing the instrumentation costs in the setup.

About the experimental results of the full bench, the functional tests [71] have shown that the motion system satisfies the requirements of precision (< 100 μm). The ferromagnetic components of the piezomotor limit the use of this (magnetic field less than 0.4 T). Regarding the experimental characterization of the prototype, the preliminary results related to the traditional wire coil (0.1237 m^2) confirmed the magnetic measurement performance in terms of repeatability (< 100 ppm) and accuracy (of about 10^{-4}) with respect to proof of principle transducer [13].

The measurements of the transducer mounting PCB coils (100 and 410 turns with 0.1803 and 0.25803 m^2 of magnetic surface) have confirmed the relative accuracy of the above mentioned results, while the repeatability has shown worse performance (> 100 ppm) with respect to the previous ones, due to the many changes on the mechanics of the trolley. In the fringe fields, the harmonics repeatability (compensated signal) was less than 10^{-4} for both the coils, showing the effect of the compensation. The reproducibility (Fig. 7.8) changing the coils reports some difference (b_4 and a_3) due to the different coil design. The tests in the homogeneous field (high-order harmonics less than 10^{-4}) have shown also the quality of the calibration magnet (MCB22). The bucking ratio of both the coils reported the best results in the homogeneous field, and in the end-fields, the coil with limited end-probe surface (PCB 100) showed the best performance (as in assessed in [29]) The magnetic profile measurements (magnetic field component B_y and dipole component B_1) and the relative comparison with the Hall probe measurements have highlighted how the traditional design (radial) used for the PCB coil is not suitable for this kind of measurements. Indeed, the bucking tests demonstrated how the longitudinal B_z component, intercepted by the coils, influences the rotating coil measurements with respect to the Hall probe. The solution could be a new coil design, tangential one (and not radial), that provides iso-perimetric coils, and consequently a new compensation scheme.

The ongoing activities will regard a full measurement campaign focused on the

validation of the system. The main requirements to verify are the fringe fields measurements of straight dipole magnets, longitudinal multipole reconstruction, and traditional measurement such as the integral field measurements. The rotating coil mapper will use traditional and iso-perimetric PCB coils, in order to avoid the distortion of the longitudinal component on the absolute and relative measurements. A new analytical approach, based on pseudo multipoles [72], must be considered for the 3-D magnetic fields measurements, in particular for reconstruction of fringing fields of large aperture and short lengths magnets.

The future works will regard also the realization of the prototype for mapping curved magnets (dipole magnets) and the relative validation (and or on-field exploitation). About the uncertainty analysis, the future work is to be devoted to take into account the uncertainty sources associated with the mechanical parts of rotating coil, whose impact cannot be usually neglected, in order to work out a comprehensive uncertainty analysis.

References

[1] Metrolab. PT 2025 NMR Teslameter. `http://www.metrolab.com/products/pt2025/`, 2003.

[2] Z. Ying-Shun et al. Design and end chamfer simulation of pefp beam line curved dipole magnets. *Chinese Phys. C*, 35(7):684–688, July 2011.

[3] E. Hirose, K.H. Tanaka, T. Takahashi, Y. Sato, K. Agari, M. Ieiri, Y. Kato, M. Minakawa, H. Noumi, Y. Suzuki, H. Takahashi, M. Takasaki, A. Toyoda, Y. Yamada, and Y. Yamanoi. A new 3-axis magnetic field measurement system based on hall elements. *Applied Superconductivity, IEEE Transactions on*, 14(2):1814–1817, June 2004.

[4] T. Ishikawa, H. Fujimura, R. Hashimoto, T. Ishida, J. Kasagi, T. Kinoshita, S. Kuwasaki, F. Miyahara, A. Miyamoto, K. Mochizuki, et al. The second GeV tagged photon beamline at ELPH. *Nuclear Instruments and Methods in Physics Research Section A: Accelerators, Spectrometers, Detectors and Associated Equipment*, 622(1):1–10, 2010.

[5] HE Hoeben Electronics. HE444 series 3D Analog Hall sensors. `http://www.hoeben.com/products-he444.html`, 2012.

[6] J. García Pérez, J. Billan, M. Buzio, P. Galbraith, D. Giloteaux, and V. Remondino. Performance of the room temperature systems for magnetic field measurements of the lhc superconducting magnets. *Applied Superconductivity, IEEE Transactions on*, 16(2):269–272, 2006.

[7] P. Arpaia, L. Fiscarelli, G. Montenero, and L. Walckiers. Active compensation of field errors within±2ppm in superconducting magnets. *Nuclear Instruments and Methods in Physics Research Section A: Accelerators, Spectrometers, Detectors and Associated Equipment*, 638(1):176–182, 2011.

[8] G. Golluccio, A. Beaumont, M. Buzio, O. Dunkel, M. Stockner, and T. Zickler. Pcb coil array for measuring curved accelerator dipoles: two case studies on the medaustron accelerator. In *20th IMEKO TC-4 International Symposium Measurement of Electrical Quantities, Benevento, Italy*, volume 2, pages 816–821, September 2014.

[9] W. Yang, X. Zhang, S. Han, J. Yang, C. Pei, L. Yang, L. Zhu, and Q. Yao. Magnetic field measurement for synchrotron dipole magnets of heavy-ion therapy facility in lanzhou. *Applied Superconductivity, IEEE Transactions on*, 24(3):1–4, June 2014.

[10] P. Schnizer, E. Fischer, H. Kiesewetter, F. Klos, T. Knapp, T. Mack, A. Mierau, and B. Schnizer. Mole for Measuring SIS100 Magnets Commissioning and First Test Results. *Applied Superconductivity, IEEE Transactions on*, 20(3):1977–1980, June 2010.

[11] P. Schnizer, E. Fischer, H.R. Kiesewetter, A. Mierau, and B. Schnizer. Field measurements on curved superconducting magnets. *Applied Superconductivity, IEEE Transactions on*, 21(3):1799–1803, June 2011.

[12] Y. Yanagisawa, K. Kusaka, T. Kubo, T. Haseyama, Y. Yano, H. Suzuki, and Y. Mizoi. Magnetic Field-Map Measurement of a Superconducting Triplet Quadrupole and a Dipole Magnet for BigRIPS Separator at RIKEN. *Applied Superconductivity, IEEE Transactions on*, 18(2):150–154, June 2008.

[13] P. Arpaia, M. Buzio, E. De Matteis, and S. Russenschuck. A rotating coil transducer for magnetic field mapping. *Journal of Instrumentation*, 10(6):P06006, 2015.

[14] P. Arpaia, E. De Matteis, and R. Schiano Lo Moriello. Unscented transform-based uncertainty analysis of rotating coil transducers for field mapping. *Review of Scientific Instrument*, 2015-(accepted for publication).

[15] S. Russenschuck. *Field computation for accelerator magnets: analytical and numerical methods for electromagnetic design and optimization*. John Wiley & Sons, 2011.

[16] J.K. Cobb and D. Horelick. A new precision measurement system for beam transport type magnets. In *Proc. 3rd Int. Conf. on Magnet Technology, Hamburg, Germany*, page 1439, 1970.

[17] L. Walckiers. Magnetic measurement with coils and wires. *arXiv preprint arXiv:1104.3784*, 2011.

[18] P. Arpaia, L. Bottura, L. Fiscarelli, and L. Walckiers. Performance of a fast digital integrator in on-field magnetic measurements for particle accelerators. *Review of Scientific Instruments*, 83(2):024702, 2012.

[19] P. Arpaia, M. Buzio, L. Fiscarelli, and V. Inglese. A software framework for developing measurement applications under variable requirements. *Review of Scientific Instruments*, 83(11):115103, 2012.

[20] C. Petrone and S. Russenschuck. *Wire methods for measuring field harmonics, gradients and magnetic axes in accelerator magnets.* PhD thesis, 2013.

[21] K. N. Henrichsen. Magnetic Field Measurements in Beam Guiding Magnets. (CERN-LHC-98-008-MMS):7, October 1998.

[22] L. Bottura and K.N. Henrichsen. Field measurements. Technical report, CERN, 2002.

[23] M. Green. Search coils. 1998.

[24] D. Zangrando and R. P. Walker. A stretched wire system for accurate integrated magnetic field measurements in insertion devices. *Nuclear Instruments and Methods in Physics Research Section A: Accelerators, Spectrometers, Detectors and Associated Equipment*, 376(2):275–282, 1996.

[25] P. Arpaia, M. Buzio, C. Petrone, S. Russenschuck, and L. Walckiers. Multipole correction of stretched-wire measurements of field-gradients in quadrupole accelerator magnets. *Journal of Instrumentation*, 8(08):P08010, 2013.

[26] J. Babiskin. Oscillatory galvanomagnetic properties of bismuth single crystals in longitudinal magnetic fields. *Physical Review*, 107(4):981, 1957.

[27] N. R. Brooks, L. Bottura, J. G. Perez, O. Dunkel, and L. Walckiers. Estimation of mechanical vibrations of the lhc fast magnetic measurement system. *Applied Superconductivity, IEEE Transactions on*, 18(2):1617–1620, 2008.

[28] J. DiMarco, H. Glass, P. Schlabach, C. Sylvester, J. C. Tompkins, and J. Krzywinski. Influence of mechanical vibrations on the field quality measurements of lhc interaction region quadrupole magnets. *Applied Superconductivity, IEEE Transactions on*, 10(1):1458–1461, 2000.

[29] J. DiMarco, G. Chlachidze, A. Makulski, D. Orris, M. Tartaglia, J.C. Tompkins, G.V. Velev, and X. Wang. Application of PCB and FDM technologies to magnetic measurement probe system development. *Applied Superconductivity, IEEE Transactions on*, 23(3):9000505–9000505, 2013.

[30] D. Schoerling. Design Study: ELENA Bending Magnet Prototype. Technical Report CERN-ACC-2013-0261, CERN, Geneva, Dec 2013.

[31] L. Angrisani, R. Schiano Lo Moriello, and P. D'Apuzzo. New proposal for uncertainty evaluation in indirect measurements. *Instrumentation and Measurement, IEEE Transactions on*, 55(4):1059–1064, 2006.

[32] Joint Committee for Guides in Metrology. Evaluation of measurement data. Guide to the expression of uncertainty in measurement: JCGM 100: 2008 (E), 2008.

[33] Joint Committee for Guides in Metrology. Evaluation of measurement data—Supplement 1 to the "Guide to the expression of uncertainty in measurement"-Propagation of distributions using a Monte Carlo method, 2008.

[34] C. Giloux, M. Karppinen, G. Mugnai, V. Remondino, W. Venturini-Delsolaro, P. Viret, L. Walckiers, and R. Wolf. Qualification of the LHC Corrector Magnet Production With the CERN-Built Measurement Benches. *Applied Superconductivity, IEEE Transactions on*, 18(2):121–125, June 2008.

[35] M. Gateau, L. Bottura, M. Buzio, and S. Sanfilippo. Uncertainty on magnetic measurements of the LHC magnets at CERN. In *IMMW 2005 - 14th International Magnetic Measurement Workshop*, CERN, Geneva, Switzerland, September 2005.

[36] L. Bottura, M. Buzio, S. Pauletta, and N. Smirnov. Measurement of magnetic axis in accelerator magnets: critical comparison of methods and instruments. In *Instrumentation and Measurement Technology Conference, 2006. IMTC 2006. Proceedings of the IEEE*, pages 765–770, April 2006.

[37] C.M. Spencer, S.D. Anderson, D.R. Jensen, and Z.R. Wolf. A rotating coil apparatus with sub-micrometer magnetic center measurement stability. *Applied Superconductivity, IEEE Transactions on*, 16(2):1334–1337, June 2006.

[38] A. Jain. Estimation of errors in the measurement of harmonics in rhic arc dipoles. Technical report, Magnet Group Note 570, Brookhaven, November 18, 1997, http://magnets. rhic. bnl. gov/publications. htm, 1997.

[39] W. Li and M. Coles. Systematic Error Analysis of Rotating Coil using Computer Simulation. In Phyllis Hale, editor, *Supercollider 5*, pages 499–502. Springer US, 1994.

[40] P. Arpaia, M. Buzio, G. Golluccio, and L. Walckiers. In situ calibration of rotating sensor coils for magnet testing. *Review of Scientific Instruments*, 83(1):013306, 2012.

[41] J. Mackey, F. Dynys, and A. Sehirlioglu. Uncertainty analysis for common seebeck and electrical resistivity measurement systems. *Review of Scientific Instruments*, 85(8):085119, 2014.

[42] A. Badalyan, Z. You, K. Aji, P. Bedrikovetsky, T. Carageorgos, and A. Zeinijahromi. Size exclusion deep bed filtration: Experimental and modelling uncertainties. *Review of Scientific Instruments*, 85(1):015111, 2014.

[43] S. Salicone. The mathematical theory of evidence and measurement uncertainty - expression and combination of measurement results via the random-fuzzy variables. *Instrumentation Measurement Magazine, IEEE*, 17(5):36–44, Oct 2014.

[44] C. De Capua and E. Romeo. A t-norm based fuzzy approach to the estimation of measurement uncertainty. In *Instrumentation and Measurement Technology Conference, 2004. IMTC 04. Proceedings of the 21st IEEE*, volume 1, pages 229–233 Vol.1, May 2004.

[45] A. Zanobini, G. Iuculano, and G. Pellegrini. The evaluation of the combined standard uncertainty for nonlinear models. In *Instrumentation and Measurement Technology Conference, 2002. IMTC/2002. Proceedings of the 19th IEEE*, volume 1, pages 359–363 vol.1, 2002.

[46] M. J. May, K. Widmann, C. Sorce, H.-S. Park, and M. Schneider. Uncertainty analysis technique for OMEGA Dante measurementsa). *Review of Scientific Instruments*, 81(10):10E505, 2010.

[47] D. C. Pace, R. Pipes, R. K. Fisher, and M. A. Van Zeeland. Mapping and uncertainty analysis of energy and pitch angle phase space in the DIII-D fast ion loss detector a). *Review of Scientific Instruments*, 85(11):11D841, 2014.

[48] L. Angrisani, P. D'Apuzzo, and R. Schiano Lo Moriello. Unscented transform: a powerful tool for measurement uncertainty evaluation. *Instrumentation and Measurement, IEEE Transactions on*, 55(3):737–743, 2006.

[49] S.J. Julier and J.K. Uhlmann. Unscented filtering and nonlinear estimation. *Proceedings of the IEEE*, 92(3):401–422, Mar 2004.

[50] A. Chao. *Handbook of accelerator physics and engineering*. World scientific, 1999.

[51] IEC BIPM, ILAC IFCC, and IUPAC ISO. IUPAP, and OIML. Evaluation of measurement dataâĂŤSupplement 2 to the "Guide to the expression of uncertainty in measurement" – Models with any number of output quantities. Joint Committee for Guides in Metrology, JCGM 102. *preparation*, 1:6–1.

[52] D. C. Montgomery. *Design and analysis of experiments*, volume 7. Wiley New York, 1984.

[53] M. S. Phadke. *Quality engineering using robust design*. Prentice Hall PTR, 1995.

[54] P. Arpaia, V. Inglese, G. Spiezia, and S. Tiso. Surface-response-based modeling of digitizers: A case study on a fast digital integrator at CERN. *Instrumentation and Measurement, IEEE Transactions on*, 58(6):1919–1928, 2009.

[55] R. A. Fisher. The design of experiments. 1960.

[56] Johson Electric Nanomotion. Piezo Motors and Subsystems. `http://www.johnsonelectric.com/en/product-technology/motion/piezo-motors-subsystems`, 2015.

[57] Avago technologies. Optical Encoder HEDM 5500-J13. `http://www.avagotech.com/`, 2015.

[58] 3D Systems. Accura 48HTR. `http://www.3dsystemsprinters.com/materials/accura-48htr/`, 2015.

[59] RadioSpare. Flexible Metrics Racks. `http://fr.rs-online.com/web/p/products/5217821/`, 2015.

[60] Avago technologies. Optical Encoder HEDS-9200 360. `http://www.avagotech.com/`, 2015.

[61] PWB encoders GmbH. Encoder Strips technical data. `http://www.pwb-encoders.com/encoder-strips/technical-data`, 2015.

[62] G. Golluccio, M. Buzio, O. Dunkel, D. Giloteaux, A. Lombardi, F. Mateo, S. Ramberger, and P. Arpaia. Magnetic measurements of permanent and fast-pulsed quadrupoles for the CERN LINAC4 project. In *Proc. Int. Particle Accelerator Conf. IPAC'10*, May 2010.

[63] National Instruments. NI PXI-6289. `http://sine.ni.com/nips/cds/view/p/lang/it/nid/14121`, 2015.

[64] L. Walckiers. The harmonic-coil method. *CERN-REPORTS*, pages 138–138, 1992.

[65] Metrolab. FDI2056 User's Manual. `http://www.metrolab.com/products/fdi2056/`, 2014.

[66] L. Bottura et al. Standard analysis procedures for field quality measurement of the LHC magnets - part I: harmonics. *LHC/MTA, Tech. Rep. LHC-MTA-IN-97-007*, 2001.

[67] Lasertex. Laser Measurement System HPI-3D. url-http://www.lasertex.eu/products.htm, 2015.

[68] O. Dunkel. Coil Manufacture, Assembly and Magnetic Calibration Facility for Warm and Cold Magnetic Measurements of LHC Superconducting Magnets. In *IMMW 14 – International Magnetic Measurement Workshop, Geneva, Switzerland*, September 2005.

[69] F. Bergsma. Calibration of Hall sensors in three dimensions, 13th Int. In *Magnetic Measurement Workshop*, 2003.

[70] H. Boterenbrood. BATCAN. `http://www.nikhef.nl/pub/departments/ct/po/html/Bsensor/BATCAN-v12.pdf`, 2010.

[71] P. Arpaia, M. Buzio, E. De Matteis, O. Dunkel, and S. Russenschuck. Magnetic field mapper based on rotating coil. In *Special Issue of IEEE Transactions on Instrumentation and Measurement on I2MTC 2016*, (accepted) 2015.

[72] H. Takeda, T. Kubo, K. Kusaka, H. Suzuki, and J. A. Inabe, N.and Nolen. Extraction of 3D field maps of magnetic multipoles from 2D surface measurements with applications to the optics calculations of the large-acceptance superconducting fragment separator BigRIPS. *Nuclear Instruments and Methods in Physics Research Section B: Beam Interactions with Materials and Atoms*, 317:798–809, 2013.

List of Figures

List of Tables